Western Graduate&PostdoctoralStudies

Western University
Scholarship@Western

Electronic Thesis and Dissertation Repository

6-22-2021 11:00 AM

Measuring inflammation in the entire myocardium in a canine model of myocardial infarction with hybrid PET/MRI

Benjamin Wilk, *The University of Western Ontario*

Supervisor: Prato, Frank S., *Lawson Health Research Institute and Western University*
Co-Supervisor: Thiessen, Jonathan D., *Lawson Health Research Institute and Western University*
A thesis submitted in partial fulfillment of the requirements for the Doctor of Philosophy degree in Medical Biophysics
© Benjamin Wilk 2021

Follow this and additional works at: https://ir.lib.uwo.ca/etd

Part of the Cardiology Commons, and the Medical Biophysics Commons

Recommended Citation

Wilk, Benjamin, "Measuring inflammation in the entire myocardium in a canine model of myocardial infarction with hybrid PET/MRI" (2021). *Electronic Thesis and Dissertation Repository*. 7911.
https://ir.lib.uwo.ca/etd/7911

This Dissertation/Thesis is brought to you for free and open access by Scholarship@Western. It has been accepted for inclusion in Electronic Thesis and Dissertation Repository by an authorized administrator of Scholarship@Western. For more information, please contact wlswadmin@uwo.ca.

Abstract

Background: After myocardial infarction (MI), fibrosis and an ongoing dysregulated inflammatory response are associated with adverse cardiac remodeling. Fluorodeoxyglucose (FDG) positron emission tomography (PET) is sensitive to inflammation provided suppression protocols are implemented to restrict the uptake of glucose in myocytes. Magnetic resonance imaging can be used to determine extracellular volume, a surrogate measure of fibrosis. In some cases, patients present with markedly reduced flow in the setting of a large infarct, i.e. microvascular obstruction, restricting the delivery of FDG and contrast agents. To overcome this problem, a constant infusion was explored as an alternative to the clinical standard bolus injection. This led to three objectives: a) comparison of the constant infusion to the bolus injection in healthy canines, b) investigation of the potential of the constant infusion to discriminate post-MI tissue types, and c) determination of the efficacy of the suppression protocol and its effect on extracellular volume.

Methods: All imaging was done with a hybrid PET/MRI scanner. MRI images were used to determine the regions of interest: remote, injured and obstructed myocardium. PET images were used to determine inflammation. To compare the injection strategies, five healthy canines were examined with all three. Subsequently, eight animals were imaged at baseline and days 3, 7, 14, 21, and 42 post-MI using a 60-min infusion. Lastly, seven animals were imaged at baseline and day 5 post-MI using a 150-min infusion. Forty minutes into the infusion, suppression of glucose uptake in myocytes was started.

Results: No significant differences in terms of glucose metabolism and extracellular volume were seen in healthy myocardium between the three injection strategies: bolus injection, constant infusion and bolus followed by constant infusion, showing that a strategy involving the constant infusion produced similar results as to those obtained with a bolus injection. Following MI, a significant increase in extracellular volume was seen in remote tissue on days 14 and 21, suggesting an inflammatory response. During the 150-min infusion, suppression of myocardial glucose uptake had the unexpected result of reducing FDG uptake in inflammatory cells within the infarcted area.

Conclusion: This research showed the possibility of using a constant infusion of Gd-DTPA and FDG to investigate inflammation within the entire myocardium. The finding that suppression affected inflammatory cells highlights the need for tracers which do not rely on myocardial glucose suppression.

Keywords

Myocardial Infarction, Heart Failure, Positron Emission Tomography, Magnetic Resonance Imaging, Hybrid PET/MRI, Constant Infusion of Tracer

Summary for Lay Audience

After a myocardial infarction, commonly referred to as heart attack, scar tissue and inflammation develop within the injured area. The scar tissue can be imaged with MRI and the inflammation with PET, provided injected contrast agents can reach the heart tissue. Some patients present with an area of extremely low flow within the injured region, unreachable with a clinically used bolus injection. A goal of my research is to test whether a constant infusion can be used to get the PET tracer and contrast agent into the injured region which is critical for imaging patient after a heart attack: if the PET tracer does not enter, there is no way to measure inflammation. The first experiment compared bolus injection and constant infusion in the normal healthy heart to establish if the results from these injection strategies are the same. The second experiment applied this approach in a model of myocardial infarction to determine if a constant infusion can measure inflammation and scarring in the remote, injured and obstructed regions of the heart. Lastly, since the PET imaging technique requires an infusion of fats to block the uptake of the PET tracer in normal heart tissue, the efficacy of this approach was tested.

Methods: All imaging was done with a hybrid PET/MRI scanner. MRI images were used to determine the regions of interest: remote, injured and obstructed myocardium. PET images were used to determine inflammation. To visualize inflammation lipids were infused.

Results: No differences were seen between constant infusion and bolus injection in healthy tissue. Findings from the second experiment suggested damage due to inflammation in remote tissue at days 14 and 21 after the heart attack. The last experiment showed that the suppression approach affected the injured region, suggesting that suppression measurement of inflammation in infarcted tissue may be underestimated.

Conclusion: This research demonstrated the ability to use hybrid PET/MRI with a dual contrast agent protocol to image inflammation in the myocardium. It also showed that remote tissue may be damaged from a myocardial infarction and that the current approach of suppression, necessary for inflammation imaging, may affect inflammatory cells, hindering accurate quantification of inflammation.

Co-Authorship Statement

All chapters except for chapters 4 and 5 were adapted from previously published manuscripts:

Chapter 1: Wilk B, Wisenberg G, Dharmakumar R, Thiessen JD, Goldhawk DE, Prato FS. Hybrid PET/MR Imaging in Myocardial Inflammation Post-Myocardial Infarction. *J Nucl Cardiol* 2019. 27(6):2083-2099.

Chapter 2: Smailovic H, Wilk B, Wisenberg G, Sykes J, Butler J, Hicks JW, Thiessen JD, Prato FS. Simultaneous measurements of myocardial glucose metabolism and extracellular volumes with hybrid PET/MRI using concurrent injections of Gd-DTPA and [18F]FDG. *J Nucl Cardiol* 2021. DOI: 10.1007/s12350-020-02486-6

Chapter 3: Wilk B, Smailovic H, Wisenberg G, Sykes J, Butler J, Kovacs M, Thiessen JD, Prato FS. Tracking the progress of inflammation with PET/MRI in a canine model of myocardial infarction. *J Nucl Cardiol* 2021. doi:10.1007/s12350-020-02487-5

Chapter 4: Wilk B, Smailovic H, Sullivan R,Wisenberg G, Sykes J, Butler J, Kovacs M, Thiessen JD, Prato FS. Myocardial glucose suppression interferes with the detection of inflammatory cells with FDG-PET in a canine model of myocardial infarction. To be submitted to Journal of Nuclear Medicine.

The experiments in this thesis were planned and performed primarily by Benjamin Wilk in the laboratories of Dr. Frank Prato and Dr. Jonathan Thiessen with the assistance of the co-authors listed below. For these experiments, the contributions from Dr. Frank Prato and Dr. Jonathan Thiessen were of an intellectual nature with respect to experimental design data analysis/interpretation and manuscript preparation.

Selection of regions of interest as well as analysis of cardiac function and PET data were performed by Benjamin Wilk. Haris Smailovic, supervised by Benjamin Wilk, assisted with analysis of extracellular volume. Rebecca Sullivan helped with histology sampling and analysis. Dr. Gerald Wisenberg is a clinical cardiologist who provided expertise in the clinical assessment of heart failure. Dr. Rohan Dharmakumar and Dr. Donna Goldhawk provided expertise in cardiac PET/MRI imaging techniques. PET tracers were provided by

the LHSC cyclotron facility, headed by Dr. Michael Kovacs. Radiochromatography, used in chapter 2, was performed by Dr. Justin Hicks. MRI technologists John Butler and Heather Biernaski performed all PET/MRI experiments at all time points. Animal care and anesthesia of animals were performed by the veterinarian technologists Jane Sykes and Lela Deans.

Acknowledgments

To my supervisor, Dr. Jonathan Thiessen I would like to express my gratitude for hours of advice, especially getting started on this project. The lab atmosphere has helped me grow and your open-door policy has made me feel comfortable in asking for help when needed. To my supervisor, Dr. Frank Prato, I would like to express gratitude for the countless hours of discussions, advice and soccer games. You have helped me grow as a scientist and as a person. Thank you for being an excellent mentor and role model.

During my doctoral study, I have been fortunate to receive stipend support through a Lawson Internal Research Fund and an Ontario Graduate Scholarship as well as travel support from the Collaborative Program in Molecular Imaging. Additionally, the Natural Sciences and Engineering Research Council of Canada and the Ontario Research Fund supported my research in Dr. Prato and Dr. Thiessen's laboratories.

I would also like to thank Dr. Gerald Wisenberg who provided substantial feedback and guidance for my articles and research directions.

I would like to thank the technicians, Jane Sykes, John Butler, Heather Biernaski and Lela Deans without whom none of this work would be possible.

I would like to express my gratitude to Haris Smailovic, for the help with data analysis and writing but also for some great soccer games.

I would like to say a special thank you to Rebecca Sullivan for helping me with my research but also for being an amazing friend who has been there for me during my academic journey.

Thank you to Qi Qi, who went from lab mate to office mate to house mate. You have been a great friend throughout.

Thank you to my friends who have provided crucial support throughout my PhD, with many relaxing weekends together.

To my fiancée, Alyssa, thank you for this wonderful journey together, with traveling, camping, martial arts and now marriage.

I would also like to thank my parents, Martina and Andreas, and my brother, Sebastian. Thank you for supporting me throughout my academic career and for continuing to push me to do my best.

Table of Contents

Abstract ii

Summary for Lay Audience iv

Co-Authorship Statement v

Acknowledgments vii

Table of Contents ix

List of Tables xv

List of Figures xvi

List of Appendices xix

List of Abbreviations xx

Preface xxiii

Chapter 1 1

1 Hybrid PET/MR Imaging of Myocardial Inflammation Post-Myocardial Infarction 1

1.1 Introduction 1

1.1.1 Role of inflammatory cells 2

1.2 Magnetic Resonance Imaging (MRI) of myocardial inflammation 4

1.2.1 Functional Imaging 4

1.2.2 “Scar imaging” 4

1.2.3 Edema imaging 5

1.2.4 Iron detection 5

1.2.5 Myocardial blood flow 6

1.2.6 BOLD MRI contrast 6

1.2.7 Chemical exchange saturation transfer (CEST) 7

1.2.8 Labeling Inflammatory Cells 7

1.3 PET imaging post-myocardial infarction 9
1.3.1 Glucose metabolism 9
1.3.2 Blood flow 10
1.3.3 Imaging macrophages 11
1.3.4 Injecting labeled inflammatory cells 12
1.4 Hybrid PET/MR technology 15
1.4.1 Hybrid PET/MR in cardiology 16
1.4.2 Future opportunities with hybrid cardiac PET/MRI 20
1.4.3 Constant Infusion Protocol 20
1.4.4 Hybrid PET/MRI protocols 20
1.4.5 Hybrid PET/MRI as a convergent technology 23
1.4.6 Artificial intelligence with hybrid PET/MRI 24
1.5 Preclinical benchmarking using animal models 26
1.6 Summary 27
1.7 Research Objectives 28
1.8 Thesis Outline 29
1.8.1 Simultaneous measurements of myocardial glucose metabolism and extracellular volumes with hybrid PET/MRI using concurrent injections of Gd-DTPA and [^{18}F]FDG 29
1.8.2 Tracking the progress of inflammation with PET/MRI in a canine model of myocardial infarction 29
1.8.3 Investigating the effects of myocardial glucose suppression on the incorporation of FDG into pro-inflammatory cells in a canine model of myocardial infarction 29
1.9 References 30
Chapter 2 53
2 Simultaneous measurements of myocardial glucose metabolism and extracellular volumes with hybrid PET/MRI using concurrent injections of Gd-DTPA and [18F]FDG 53

2.1 Introduction 53
2.2 Materials and Methods 55
2.2.1 Animal Preparation 55
2.2.2 PET/MRI Protocol 55
2.2.3 Image Analysis 58
2.2.4 Glucose Metabolism 59
2.2.5 FDG stability under concurrent injection with GBCAs 60
2.2.6 Statistical Analysis 61
2.3 Results 61
2.3.1 FDG stability under concurrent injection with GBCAs 61
2.3.2 Evaluation of ECV in Healthy Myocardium with and without glucose suppression 62
2.3.3 Comparison of ECV in Healthy Myocardium – Measurements using Different Injection Types 64
2.3.4 Glucose metabolism using Patlak parameter estimates 65
2.3.5 Change in T1 during each contrast delivery method 66
2.4 Discussion 68
2.5 Conclusion 71
2.6 References 72
Chapter 3 76
3 Tracking the progress of inflammation with PET/MRI in a canine model of myocardial infarction 76
3.1 Introduction 76
3.2 Methods 78
3.2.1 Animals and Surgical Preparation 78
3.2.2 PET Imaging 78
3.2.3 Cardiac MR imaging 79

3.2.4 Data Analysis 80
3.2.4.5 MRI Measurement of Heart Function 82
3.3 RESULTS 83
3.3.1 Volume of IOT and INOT 83
3.3.2 Extracellular Volume 85
3.3.3 Patlak Parameter Estimates 89
3.3.4 Measurements of Cardiac Function 92
3.4 Discussion 93
3.5 Conclusion 96
3.6 References 97
Chapter 4 102
4 Myocardial glucose suppression interferes with the detection of inflammatory cells with FDG-PET in a canine model of myocardial infarction 102
4.1 Introduction 102
4.2 Materials and Methods: 103
4.2.1 Animal Preparation 103
4.2.2 Injection Protocol 105
4.2.3 PET/MRI Protocol 106
4.2.4 Image Analysis 107
4.2.5 Volumes of IOT and INOT 108
4.2.6 Extracellular Volume Determination 108
4.2.7 Glucose Metabolism 108
4.2.8 Histology 109
4.2.9 Statistical Analysis 110
4.3 Results 110
4.3.1 Effect of Suppression on metabolic rate of glucose consumption 110

4.3.2 Effect of suppression on extracellular volume 111
4.3.3 Penetration of infarcted obstructed tissue 113
4.3.4 Histology 113
4.4 Discussion 114
4.5 Conclusion 116
4.6 References 117
Chapter 5 120
5 Conclusions, Limitations and Future Directions 120
5.1 Conclusions and Future Direction 120
5.2 Research Objectives 120
5.3 Summary of Individual Chapters 120
5.3.1 Chapter 1: Hybrid PET/MR imaging in myocardial inflammation post-myocardial infarction 120
5.3.2 Chapter 2: Simultaneous measurements of myocardial glucose metabolism and extracellular volumes with hybrid PET/MRI using concurrent injections of Gd-DTPA and [18F]FDG 121
5.3.3 Chapter 3: Tracking the progress of inflammation with PET/MRI in a canine model of myocardial infarction 121
5.3.4 Chapter 4: Myocardial glucose suppression interferes with the detection of inflammatory cells with FDG-PET in a canine model of myocardial infarction 122
5.4 Limitations 123
5.5 Future Work 124
5.5.1 The role of the remote tissue 124
5.5.2 The role of the microvascular obstruction in left ventricular remodelling 125
5.5.3 Interventions during a constant infusion 126
5.5.4 Patient Study 126
5.6 Conclusion 128

5.7 References 129

Appendices 131

Curriculum Vitae 135

List of Tables

Table 1: Chemical Stability when combining Gd-DTPA or gadobutrol and FDG..... 61

List of Figures

Figure 1-1: Availability of PET tracers and MRI approaches for a convergent hybrid PET/MRI approach to the study of cardiac inflammation post MI. ..... **Error! Bookmark not defined.**

Figure 1-2: Comparison of the capability of different large animal and human molecular imaging modalities. ..... **Error! Bookmark not defined.**

Figure 1-3: Longitudinal comparison of inflammation post-MI with PET/MR in a canine model. ..... **Error! Bookmark not defined.**

Figure 1-4: Post-mortem images of the left ventricle in a canine model. Hybrid PET/MRI after constant simultaneous infusion of FDG and Gd-DTPA in a large animal model of inflammation Post MI. ..... **Error! Bookmark not defined.**

Figure 1-5: Conventional vs convergent approaches to cardiac hybrid PET/MRI protocols. ..... **Error! Bookmark not defined.**

Figure 1-6: Imaging myocardial perfusion reserve and inflammation with a convergent PET/MRI protocol. ..... **Error! Bookmark not defined.**

Figure 2-1: Suppression differences based on injection type with FDG imaging. 56

Figure 2-2: Injection protocol with three different injection strategies. 57

Figure 2-3: Region of interest selection at baseline. 59

Figure 2-4: The effect of glucose suppression on healthy non-infarcted myocardial ECV. ... 63

Figure 2-5: The time course of changes in the measured ECV of Gd-DTPA in healthy myocardium in five canine subjects, with glucose suppression, measured every 3 minutes for up to 90 minutes after start of injection. 64

Figure 2-6: The effect of glucose suppression on healthy non-infarcted cardiac myocardium Ki, a marker of glucose metabolism. 65

Figure 2-7: Changes in T1 values over time in both the myocardium and the blood..... 67

Figure 3-1:FDG uptake at day 7 post-MI, 10 minutes after the end of the constant infusion. 78

Figure 3-2: Experimental Protocol..... 80

Figure 3-3: Region of interest selection post-MI on a 2-chamber T1 map..... 81

Figure 3-4: 2-Chamber T1 maps throughout the constant infusion at day 7. 84

Figure 3-5: Change in INOT Volume over Time. 84

Figure 3-6: ECV in remote tissue post-MI. 85

Figure 3-7: ECV measurements pre- and post-MI in all tissue types. 86

Figure 3-8: ECV measurements in the INOT post-MI. 87

Figure 3-9: ECV in the INOT 3 days post-MI. 88

Figure 3-10: Remote tissue Ki pre- and post-MI. 89

Figure 3-11: Ki in INOT post-MI. 90

Figure 3-12: Distribution volume (y-intercept) calculated using the Patlak model in the INOT. 91

Figure 3-13: End-systolic volume, end-diastolic volume and ejection fraction over time post-MI. 92

Figure 4-1: 150-minute constant infusion protocol. 104

Figure 4-2: FDG uptake and T1 maps 5 days post-MI pre- and post-suppression. 106

Figure 4-3: Regions of interest at 5 days post-MI used for the 150-minute constant infusion protocol. 108

Figure 4-4: FDG activity concentration over the course of a 150-minute constant infusion in one representative animal. 111

Figure 4-5: Metabolic rate of glucose consumption at baseline and 5 days post-MI. 112

Figure 4-6: Suppression of myocardial glucose uptake does not affect ECV at 5 days. 112

Figure 4-7: IOT and INOT volume 5 days post-MI. 113

Figure 4-8: GLUT1 and CD68 expression 5 days post-MI. 114

Figure 5-1: Comparison of Ki in IOT and INOT. 125

List of Appendices

Appendix A: Copyright for Chapter 1: Hybrid PET/MR Imaging in Myocardial Inflammation Post-Myocardial Infarction 131

Appendix B: Animal Use approval for chapters 3 and 4. 132

Appendix C: Copyright for Chapter 2: Simultaneous measurements of myocardial glucose metabolism and extracellular volumes with hybrid PET/MRI using concurrent injections of Gd-DTPA and [18F]FDG 132

Appendix D: Copyright for Chapter 3: Tracking the progress of inflammation with PET/MRI in a canine model of myocardial infarction 133

Appendix E: Ethics approval of cardiac patient study mentioned in Chapter 5 134

List of Abbreviations

AMI – Acute Myocardial Infarction

BI – Bolus Injection

BL – Baseline

BOLD – Blood Oxygen Level Dependent

CEST – Chemical Exchange Saturation Transfer

CI – Constant Infusion

CT – Computed Tomography

CTAC – Computed Tomography Attenuation Correction

CXCR4 – Chemokine Receptor Subtype 4

DTPA – diethylenetriaminepentacetate

ECV – Extracellular Volume

EDV – End-Diastolic Volume

EF – Ejection Fraction

ESV – End-Systolic Volume

FDG – ^{18}F – Fluorodeoxiglucose

$[FDG(t)]_b$ – Whole Blood Concentration

$[FDG(t)]_i$ – Concentration of [^{18}F]FDG in Tissue i

$[FDG(t)]_p$ – Arterial Plasma Concentration

GBCA – Gadolinium Based Contrast Agent

GLUT1 – Glucose Transporter Type 1

Hct – Hematocrit

INOT – Infarcted Not Obstructed Tissue

IOT – Infarcted Obstructed Tissue

Ki – Influx Constant in Tissue i

MI – Myocardial Infarction

MO – Microvascular Obstruction

MOLLI – Modified Look-Locker Inversion Recovery

MR – Magnetic Resonance

MRAC – Magnetic Resonance Attenuation Correction

MRGlu – Metabolic Rate of Glucose

MRI – Magnetic Resonance Imaging

MMR – Macrophage Mannose Receptor

OCT – Optimal Cutting Temperature Compound

OSEM – Ordered Subset Expectation Maximization

P – Glucose Plasma:Whole Blood Ratio

PBS – Phosphate Buffered Solution

PET – Positron Emission Tomography

RC – Recovery Coefficient

ROI – Region of Interest

RT – Remote Tissue

SEM – Standard Error of the Mean

SPECT – Single Photon Emission Computed Tomography

SPIO – Superparamagnetic Iron Oxide

TrueFISP - True Fast Imaging With Steady-State Free Precession

TSPO – Translocator Protein

V_d – Volume of Distribution

v_e^p – Equilibrium Space of the Extravascular Exchangeable Region

v_p^p – Plasma Space of the Extravascular Exchangeable Region

Preface

The first chapter in this thesis is adapted from a published review paper: Wilk B, Wisenberg G, Dharmakumar R, Thiessen JD, Goldhawk DE, Prato FS. Hybrid PET/MR Imaging in Myocardial Inflammation Post-Myocardial Infarction. *J Nucl Cardiol* 2019. 27(6):2083-2099. This chapter sets the groundwork for the rest of the thesis in terms of what has been done in the field of imaging inflammation post-myocardial infarction and how current PET and MRI techniques can be applied to complement each other. Also outlined are tracer and contrast agent options to image different aspects of inflammation. In the following chapters, the focus is on a combination of FDG and gadolinium-based contrast agent. The constant infusion technique will be investigated to optimize tracer delivery and image all regions of the heart rather than only the infarcted area.

Chapter 1

1 Hybrid PET/MR Imaging of Myocardial Inflammation Post-Myocardial Infarction

In this introductory chapter, I review the current and predict the future contributions that hybrid PET/MRI technology can make toward advancing our understanding of myocardial inflammation post-myocardial infarction. First, it is necessary to describe the role of inflammatory cells post-MI, then the contributions that MRI has made to this understanding. This is followed by explaining the contribution that PET has made. Then, with this background on the separate contributions that MRI and PET can and, in the future, could make, we introduce the technology of hybrid PET/MRI and explore how it has, to date, and could, in the future, further our understanding of inflammation post-MI. We explore the potential contributions of hybrid PET/MRI if we first treat hybrid PET/MRI as more than a simple combination of PET and MRI. Rather, we suggest that hybrid PET/MRI can be treated as a new convergent technology, where the PET aspect is modified to the realities of MRI and the MRI modified to the realities of PET. We investigate, under this convergent view of hybrid PET/MRI, biophysical explorations that would result in new horizons in imaging inflammation post-MI. We conclude that fruitful research would be the development of hybrid PET/MRI protocols including combining, for the first time, concurrent simultaneous injections of a PET tracer and an MRI contrast agent. In the research that follows (chapters 2 and 3) we first demonstrate that the novel acquisition protocols and novel infusion methods provide valid, quantitative results. Then in chapter 4, we explore this methodology to address the fundamental questions with respect to cardiac imaging that in the past has not, and perhaps could not, be addressed if a convergent approach of hybrid PET/MRI had not been used.

1.1 Introduction

Although early mortality in patients with acute myocardial infarction (AMI) has declined by 75% over the past half century[1], these patients still remain at risk for late adverse

events and death[2]. Evidence suggests that infarct size[3,4], extent of microvascular obstruction within infarcted tissue[5] and extent of iron precipitation[6–8] following hemorrhagic infarction are independent predictors of left ventricular remodeling post-AMI, leading to heart failure. Furthermore, this remodeling is associated with additional effects on myocardial tissue remote from the AMI caused by an ongoing dysregulated pro-inflammatory process[9,10]. The target/substrate to be imaged in post-myocardial infarction is predominantly inflammatory cells responding to aseptic injury. There is also growing evidence that the presence of iron in the infarcted tissue following a hemorrhagic infarct plays a further role in modulation of inflammation[6,8].

1.1.1 Role of inflammatory cells

After AMI, pro-inflammatory processes stabilize the region of infarction with scar tissue that strengthens the muscle to prevent the development of an aneurysm and reduce the potential for sudden death from cardiac rupture[11–13]. Two cellular hallmarks of this pro-inflammatory stage include neutrophils[14] (peaking within the first few hours to days post-MI in humans and dogs) and classically-activated (M1) macrophages (peaking between 3 and 10 days post-MI in humans and dogs)[6,15–20]. The population of M1 macrophages is primarily of myeloid origin, but may also include tissue resident macrophages within the myocardium and those drawn from splenic reservoirs[21–24]. These are the dominant inflammatory cell types responding to MI. The pro-inflammatory period is followed by an anti-inflammatory stage where the predominant cellular hallmark is the recruitment of alternatively-activated (M2) macrophages[13]. Note that M1 and M2 macrophages are a simplification and the picture is more complex with in-between macrophage phenotypes and the possibility for the polarization to change[25,26]. It has been suspected that progression to heart failure post AMI is related to a sustained pro-inflammatory response[27,28]. A sustained pro-inflammatory response may also have negative effects on scar stability leading to cardiac rupture[29].

Anti-inflammatory clinical trials have yielded mixed results[30]. If anti-inflammatory therapies are given too early to reduce the “healing” inflammatory response, the patients are at increased risk of aneurysm; if administered too late, there is an increased risk of negative local and remote myocardial tissue remodeling. In order to develop effective

therapies tailored to modify this dynamic process towards improved clinical outcomes, a non-invasive cardiac imaging method is required to detect the differential time course, post-AMI, of the inflammatory processes in three myocardial tissues: a) infarcted tissue with microvascular obstruction (i.e. infarcted obstructed tissue, IOT), b) infarcted tissue excluding the zone of microvascular obstruction (i.e. infarcted not obstructed tissue, INOT) and c) myocardial tissue remote from the infarcted tissue (i.e. remote tissue, RT). These tissues may have vastly different patterns and timing of the inflammatory response. However, if the appropriate therapy could be tailored for each patient early in the management and progression of the disease process, using noninvasive imaging to differentiate between neutrophils, M1 and M2 macrophages, then we could optimize therapy in real time, inform treatment and personalize care.

Given their divergent effects, non-invasive imaging that distinguishes between M1 and M2 macrophages is critical and hence an understanding of the differences that could be exploited for imaging is essential. Glucose uptake in M1 macrophages is approximately twice that of M2 macrophages and phagocytic activity of M2 is approximately twice that of M1[31,32]. Also, macrophage phenotype may be distinguished based on iron handling, as M1 exhibit an iron storage phenotype while M2 display an iron recycling phenotype[33,34]. Macrophages are among the few mammalian cells to express the only recognized mammalian iron export protein, ferroportin. Its activity is subject to regulation by the endocrine hormone hepcidin, produced primarily in the liver in response to pro-inflammatory cytokines, like interleukin-6, and elevated levels of iron. Systemic hepcidin-ferroportin interactions induce ferroportin degradation and interrupt iron export[35]. In the dog, serum hepcidin levels rise within 4 to 6 days post-MI (unpublished data from the laboratory of Dr. DE Goldhawk), facilitating the production of M1 macrophages and locally depriving the injured tissue of iron. In the canine model of myocardial hemorrhage, Kali et al[6] suggest that elevated iron stalls macrophage progression from M1 to M2, consistent with the interaction of hepcidin and ferroportin. This in turn may delay the evolution of M2 activities needed to stabilize the scar, like fibroblast formation, and may also damage RT by prolonging the pro-inflammatory activity of M1 macrophages.

1.2 Magnetic Resonance Imaging (MRI) of myocardial inflammation

Post-MI, MRI is an attractive modality to use due to its high spatial resolution, excellent soft tissue contrast, and ability to mitigate and/or measure cardiac and respiratory motion.

1.2.1 Functional Imaging

The capability of MRI to acquire "cine" images of wall motion throughout the cardiac cycle during breath holds has resulted in cardiac MRI becoming effectively the gold standard for the quantitation of ejection fraction, end diastolic volumes and end systolic volumes, all important in the definition of cardiac function with respect to progression towards heart failure. The imaging of left ventricle wall strain showing wall fiber tracks has not been as important. Although developed in the 1990s[36] strain imaging has yet to establish itself for discriminating INOT and IOT[37]. The imaging of smaller cardiac structures such as those associated with the atria have been more difficult due to the thinness of the atrial wall, approaching the resolution of MRI. Developments such as phase contrast flow imaging, where the velocity of moving magnetic moments (flow) is proportional to the phase shift[38], and its successor, 4D Flow, have been helpful in estimating effects of valve defects on regurgitant fraction in the ventricles[39]. Attempts to apply 4D Flow to investigate effects of atrial fibrillation are in development[40].

1.2.2 "Scar imaging"

It has been shown extensively that the distribution volume of gadolinium chelates such as Gd-DTPA corresponds to the extracellular space in the myocardium. This is calculated as the ratio of the concentration of Gd chelate in the myocardium divided by the concentration in the blood, which is often referred to as the partition coefficient and designated as λ. The volume of distribution can be calculated from λ if the hematocrit (Hct) is known, i.e. $V_d = \lambda \times (1 - Hct)$. It has been shown in both humans and dogs that λ in myocardial tissue post-MI increases from approximately 0.45 to 0.9 ml/g[41–43]. For a hematocrit of 0.4, this would correspond to volumes of distribution going from 0.27 to

0.54 ml/g. It has also been shown that a) this increase occurs within a few hours of occlusion/reperfusion injury[43], b) that it may be reduced when the post-MI injury has become chronic[43,44], c) it represents a marker of permanently damaged myocardium[45], as reversible injury such as stunning[41] or hibernation[46] does not increase λ substantially[47] and d) given MRI's spatial resolution, it allows the transmural extent of the infarct to be determined[48,49]. Non-contrast-enhanced scar imaging approaches have also demonstrated that scar following MI can be characterized on the basis of T1 mapping using modified Look-Locker with balanced steady state free-precession readouts at 3.0 T[50,51].

1.2.3 Edema imaging

The T2 relaxation rate increases in tissue containing an increase in extra-cellular water i.e. edema, resulting in a hyperintense signal in T2-weighted MRI. The extent to which edema correlates with the extent of inflammation post-MI still needs to be determined[52].

1.2.4 Iron detection

T2*-weighted cardiac MR is effective in the detection and characterization of infarction/reperfusion induced myocardial hemorrhage[7,8,53]. Histological study of canine myocardial infarction has shown that persistent microvascular obstruction post-MI culminates in the development of ferric iron oxide crystals, an increased pro-inflammatory burden and adverse remodeling[6]. A postulated mechanism is that the conversion from M1 to M2 macrophages may be delayed by this iron crystal formation leading to dysregulation of the inflammatory response and progression to heart failure and/or an aneurysm at the site of infarction[6]. However, in vivo validation of this hypothesis requires the non-invasive differential imaging of M1 and M2 macrophages at the site of iron accumulation. Note that it has recently been shown in the P19 monocyte cell line that extracellular iron concentration (25μM of ferric nitrate) reduces ferroportin expression[54]. Quantitative susceptibility mapping (QSM) has also been used to determine tissue iron content and relate this to patient outcome[55].

1.2.5 Myocardial blood flow

Myocardial blood flow is a major consideration when discussing myocardial inflammation as it may play a major role in the degree and extent of the process. Myocardial blood flow can be measured following a bolus injection of a gadolinium chelate with transmural resolution[56,57]. However, complete heart coverage may not always be possible and two bolus injections to account for signal saturation are often employed[58,59], increasing the amount of Gd-chelate that is needed though methods are being developed to overcome these issues. Comparison to determinations using PET have indicated the increased complexity of the use of Gd-chelates which have a much lower extraction fraction compared to PET methods such as those using ^{13}N-Ammonia or ^{15}O-water[60–62]. It is important to note here that ^{13}N-Ammonia enters and is trapped in living cells while Gd-chelates are extracellular[63].

1.2.6 BOLD MRI contrast

Blood oxygen level dependent (BOLD) contrast in MRI has been extensively applied for the non-invasive study of the brain. Due to the decreased extraction fraction of oxygen when blood flow increases, venous blood contains higher levels of oxyhemoglobin with a corresponding decrease in the concentration of deoxyhemoglobin. When the venous deoxyhemoglobin concentration falls, then T2* increases. Hence the BOLD effect is an indication of the venous concentration of deoxyhemoglobin. Li et al[64] have shown in normal volunteers that following the administration of the hyperemic agent, dipyridamole, with increased myocardial blood flow, there is an increase in T2* which is consistent with a decrease in myocardial venous deoxyhemoglobin concentration as myocardial oxygen supply exceeds demand[64]. In contrast, the administration of dobutamine resulted in an increase in coronary blood flow but no significant change in T2* consistent with a lack of change in myocardial venous deoxyhemoglobin concentration which is interpreted as a balance between oxygen supply and demand. This seminal work laid the foundation for future applications. However, not until recently has the BOLD measurement in the myocardium been of sufficient accuracy to be used in routine cardiac assessment. Recently, new MRI methods for the measurement of cardiac

BOLD have shown considerable promise indicating a potential to assess myocardial ischemia comparable with SPECT and PET methodologies[65]. As this has now been demonstrated in a canine model of ischemia, clinical studies demonstrating feasibility are needed.

1.2.7 Chemical exchange saturation transfer (CEST)

Chemical exchange saturation transfer (CEST) relies on the selective saturation and exchange of protons from metabolites of interest to the free protons imaged with MRI[66–68]. CEST has been used to detect changes in protein concentration[69], glutamate[70], creatine[71], glycosaminoglycan and most notably pH (acidoCEST)[72,73] and D-glucose (glucoCEST)[74–76] though it can be difficult to unravel changes in CEST signal from changes in pH, T1, temperature and other metabolites[77]. To our knowledge, neither glucoCEST nor acidoCEST have been attempted in the heart, although there would be some utility for alternative measurements of perfusion and pH post-MI. Cardiac CEST acquisitions are challenging, however, recent promising results suggest its utility for measuring myocardial creatine kinase[78–80] and hyaluronan synthesis[81] post-MI.

1.2.8 Labeling Inflammatory Cells

Iron particles of magnetite are strong negative contrast agents attenuating the MRI signal through the strong susceptibility induced by ferromagnetism. Using iron particles to label cells has been investigated using two different approaches. In one, inflammatory cells are isolated from blood lymphocytes, labeled with iron particles (such as superparamagnetic iron oxide (SPIO) particles) and then re-injected[82]. In this scenario, detection of loss of MRI signal within the myocardium signifies presence of labeled cells once the blood background is reduced, and, provided the iron particles have not been released by dying lymphocytes and either engulfed by other cells or lodged in the extracellular space. This signal may also be confounded by endogenous iron due to hemorrhage. Although it has been shown that, under optimal conditions, individual cells can be seen, quantitation of label has proven challenging due to a) the difficulty in relating the magnitude of the loss of MRI signal with the amount of iron particles[83] and b) the dilution of the label as

labeled cells proliferate. This effectively limits the quantitation of the number of cells. Note that labeling cells with positive contrast (e.g. ^{19}F) may overcome this issue but dilutions due to proliferation cannot be overcome[84–86].

In addition to phagocytic activity, monocytes and macrophages possess iron export activity that is detectable by MRI. In the human THP-1 monocyte cell line, iron export prevails regardless of extracellular iron concentration[87]. These cells display both autocrine/paracrine regulation of ferroportin as well as the endocrine response to hepcidin. In the multi-potent P19 cell line, extracellular iron stimulates iron export through transcriptional regulation, whereas the presence of hepcidin knocks it back down via post-translational modification[35,54,88]. Thus, processes governing the up and downregulation of iron export co-exist and contribute an MR visible signal that will be influenced by pro-inflammatory signaling through hepcidin, the inherent iron recycling activity of M2 macrophages, and the iron released from SPIO degradation.

In the second approach, SPIO particles or perfluorocarbon agents are injected intravenously, hypothesizing that macrophages will engulf them and allow their detection. It has been shown in vitro that their engulfment rate in M2 macrophages is approximately 50% greater than for M1 macrophages[31]. However, using this method, the MRI signal will be related to the uptake of particles by both M1 and M2 macrophages, making it difficult to determine the relative contribution of each cell population to the signal change.

Hyperpolarized ^{13}C-pyruvate is another option for imaging macrophages as the lactate signal is increased in macrophages in vitro[89]. It has also been shown that rodents and pigs exhibit a high lactate response in the infarcted region post-MI[90].

MRI reporter genes that deliver strong contrast have been difficult to develop[91]. One of the best approaches involves introducing genes from magnetotactic bacteria in mammalian cells for the biosynthesis of membrane-enclosed SPIO-like particles called magnetosomes[92]. The technology was initially attempted using single gene expression systems[93]. If this technology could be implemented such that the concentration of iron particles in mammalian cells were equal to that in magnetotactic bacteria, theoretical

calculations indicate that as few as 3 cells could be detected in small animals and as few as 2,600 cells in large animals and humans[93]. This would correspond to a major breakthrough. For example, white blood cells from the peripheral circulation (e.g. monocytes) could be isolated and transfected with the MR reporter gene expression system, which could be programmed to produce magnetosome-like iron particles upon promoter activation. For example, the receptor gene could be engineered to signal, by production of iron particles, a molecular event involved in differentiation of the monocyte into an M1 macrophage. One of the main obstacles remaining is the acceptance of genetically modified cells for human use, although this strategy is now permitted in some therapeutic applications[94].

1.3 PET imaging post-myocardial infarction

Although there are a large number of PET probes for cardiac investigation that have been developed, see Fig 1-1, clinical practice to date for use in post-MI patients has used only a few[95]. PET imaging post-MI is most commonly done with ^{18}F-FDG although suppression of healthy myocyte glucose uptake is needed concurrent with flow tracers to evaluate ischemia. However, other tracers that target translocator protein (TSPO) receptors in inflammatory cells, such as ^{18}F-GE180 which, while having potential for pre-clinical small animal imaging of macrophage activity, has been largely dismissed for human imaging due to poor brain penetration[96] or ^{18}F-FEPPA[97,98], may be used to target macrophages specifically.

1.3.1 Glucose metabolism

Inflammation can be measured with ^{18}F-FDG due to the increased presence of glucose transporters on macrophages[99]. Due to this, uptake of glucose is upregulated in areas of inflammation. The non-specificity of ^{18}F-FDG for evaluating cardiac inflammation is, however, compounded by uptake in normal myocytes which must be suppressed for successful, unambiguous detection of inflammation. The failure, at times, to effectively suppress that uptake by either dietary modification (high fat), overnight fasting and/or heparin injection, may result in failure of the test. Five percent of the time this test fails

even under the best diet and fasting protocols[100]. The reduced spatial resolution of ^{18}F-FDG PET compared to 3T MRI makes it difficult to uniquely identify ^{18}F-FDG uptake in the three tissue regions post MI: IOT, INOT and RT. Although in vivo cardiac imaging reflects the significant uptake by inflammatory cells, it may not allow the distinction between M1 and M2 inflammatory cells.

It has been shown in vitro that ^{18}F-FDG uptake in M1 macrophages is greater than in M2 macrophages. Uptake in M1 macrophage is twice that of M2 when differentiated from the human THP-1 monocyte cell line[31]. In contrast, when using primary monocytes from human blood, the uptake of ^{18}F-FDG in M1 macrophages is ten times greater than M2[101]. This is further obscured as uptake of ^{18}F-FDG by neutrophils and monocytes may be similar to that of M1 macrophages. Although compartmental analysis allows the quantitation of glucose metabolism in units of mmol per gram per minute, there has been little or no attempt to evaluate quantitative ^{18}F-FDG uptake post-MI in macrophages. The upregulation of ^{18}F-FDG metabolism in inflammatory cells must be very large for this to be seen in infarcted tissue since the density of inflammatory cells in infarcted tissue would be much lower than that of myocytes in normal and remote tissue. It is unknown at this time if myocardial suppression of ^{18}F-FDG uptake affects uptake of ^{18}F-FDG in inflammatory cells. However, work reported of ^{18}F-FDG studies in cardiac sarcoidosis indicates that if uptake is suppressed in inflammatory cells it is not sufficient to eliminate the strong signal of inflammation[102].

1.3.2 Blood flow

Historically, PET myocardial blood flow measurements have used ^{13}N-Ammonia, ^{15}O water or ^{82}Rb. At centers using PET/CT, ^{82}Rb is often used since it does not require an on-site cyclotron, as opposed to ^{13}N-Ammonia (10 min half-life) and ^{15}O-water (2 min half-life). However, the ^{82}Rb positron range reduces effective spatial resolution and, to date, no manufacturer of ^{82}Rb/^{82}Sr generators has produced an MR-compatible system. In this context, ^{13}N-Ammonia is attractive for cyclotron-equipped sites and it has both high first pass extraction fraction and good retention characteristics[103]. However, the 10-minute half-life makes stress/rest studies expensive. More development of a repeat

injection strategy would lower costs substantially by greatly reducing the length of the exam[104]. Alternatively, ^{18}F-flurpiridaz is attractive due to its very high extraction and retention characteristics, but the cost of the tracer may negatively impact its implementation. Additionally, the long half-life makes it difficult to conduct stress/rest exams during a single imaging session as the traditional approach requires waiting for the tracer to have decayed between the stress and the rest scans. New single-scan dual-injection protocols have significantly cut down the required time for Furpriridaz perfusion imaging[105]. Whereas the measurement of blood flow reserve is important in the scenario of stable coronary disease, its value post-MI has not been established, perhaps due to the difficulty of combining two ^{13}N-Ammonia studies and one ^{18}F-FDG study.

1.3.3 Imaging macrophages

Many PET ligands have been developed to detect upregulation of the mitochondrial translocator protein (TSPO) in activated microglia, the tissue resident macrophages of the brain[106]. Similar to FDG, TSPO is taken up more by pro-inflammatory than anti-inflammatory cells[107]. There is the added limitation that a polymorphism affects TSPO binding[108]. Recently it has been shown[109] in mice and humans that myocardial inflammation post-MI could be detected using a TSPO PET ligand. However, in vitro work[101] suggests that this compound is taken up by other inflammatory cells besides M1 macrophages. (It has been reported that the uptake in M1 macrophages is four times greater than the uptake in M2 macrophages, neutrophils, monocytes, T/NK cells and B cells.[101]) The one real advantage over ^{18}F-FDG is that uptake of TSPO PET ligands in the normal myocardium does not have to be suppressed in order to detect inflammatory cells remote from the infarcted tissue. However, almost all research has been related to uptake in microglia and there is a need for more research into the in vivo uptake of TSPO PET ligands by inflammatory cells.

Other targets for inflammatory tracers include the chemokine receptor CXCR4 which has been shown to colocalize with CD68 with the additional benefit of not being taken up by the myocardium. [^{68}Ga] Pentixafor targets this receptor and has been used to image atherosclerosis and acute myocardial infarction[110,111]. Somatostatin receptor subtype-2 is

another promising target for PET imaging and is highly expressed in M1 macrophages. This can be imaged with radio-labeled DOTATATE (^{68}Ga or ^{64}Cu) and has been applied in patients with atherosclerosis[112,113]. Many other targets such as apoptosis[114], matrix metalloproteinases[115] or the macrophage mannose receptor (MMR) have been reported where MMR is upregulated in M2 macrophages[116]. Some of these options and others are summarized in figure 1-1.

1.3.4 Injecting labeled inflammatory cells

Although labeling white blood cells has been practiced in nuclear medicine for decades to detect sites of inflammation, imaging these cells within the myocardium has not been possible[117]. This is due to a) partial volume effects and b) the lack of retention of the tracer within the labeled cells[118] . Another problem is that a bolus injection of ^{18}F-FDG does not allow sufficient delivery of labeled inflammatory cells into the IOT. However, in animals, ^{111}In labeled white blood cells do accumulate if injected approximately 24 hours prior to sacrifice, as detected by in vitro tissue sample counting[119]. A recently developed new PET probe (^{89}Zr-DBN) that labels the (white blood) cell plasma membrane in a stable manner[118] addresses tracer leakage. The attractiveness of a ^{89}Zr label is its long half-life (3.3d) which would allow the initial high background activity in the left ventricular cavity to be reduced/cleared. However, effective implementation will require high spatial resolution anatomic images of the heart (by CT or MRI) that are reliably registered to the PET image to allow for effective partial volume correction and confidence in the location of regions of interest corresponding to IOT, INOT and RT identification. Although quantitation of the ^{89}Zr signal is relatively simple and reliable compared to quantitation of SPIO iron particles by MRI, there is still the problem of quantitation of the number of cells. Obtaining the absolute number of cells rather than a relative amount of inflammation would be ideal for determining the efficacy of anti-inflammatory therapy, comparison to histology or future research into the mechanism of inflammation post-MI. Inflammatory cell proliferation and resultant dilution of the label interferes with reliable quantitation. As has been shown by Blackwood et al, one likely advantage over MRI is that, as cells die, ^{89}Zr-labeled debris will likely not be engulfed by other cells[120]; whereas, the SPIO particles released by labeled cells as they die have been

reported trapped in other cells and in the interstitium of the myocardium[121,122]. Reporter genes have also been developed for PET. Cells that are transfected and transplanted directly into the myocardium can be visualized after injection of the needed radiolabeled substrate[123,124]. To date, tracking intravenously-injected PET reporter gene-expressing cells within IOT, INOT and RT has not been accomplished and there remains the general prohibition of injecting genetically modified cells into humans. Nevertheless, it might be worth investigating if ^{89}Zr-labeled cells could be developed that would allow visualization of inflammatory cells in the IOT, INOT and RT regions, if hybrid PET/MRI were used to identify the anatomical location of the ^{89}Zr activity. Fig 1-1 summarizes the currently available PET probes and MRI agents discussed.

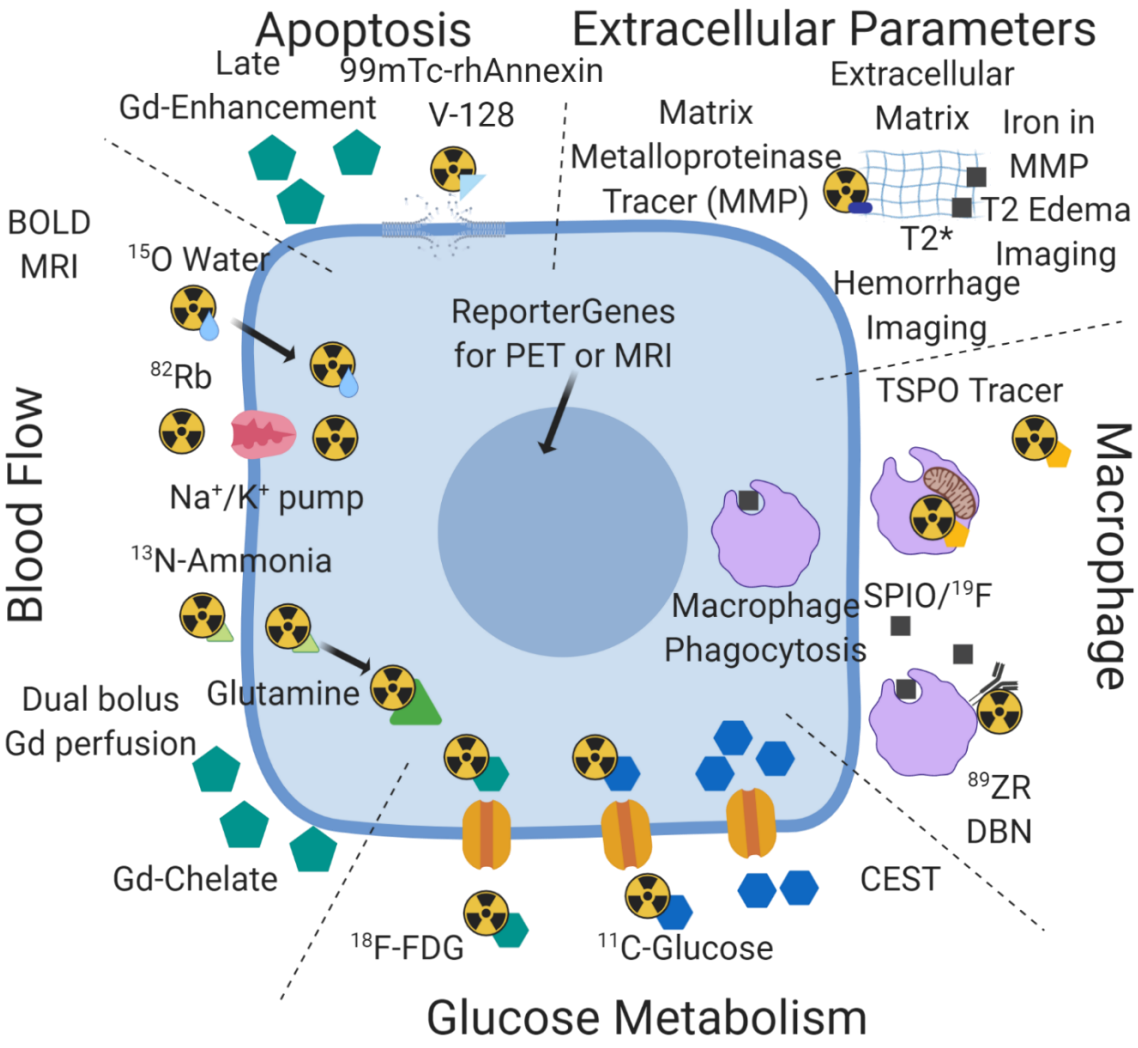

Figure 1-1: Availability of PET tracers and MRI approaches for a convergent hybrid PET/MRI approach to the study of cardiac inflammation post MI.

This figure is an attempt to integrate the PET tracers and MRI approaches available for the study of inflammation post MI under the categories of myocyte glucose metabolism, detection of inflammatory cells, measurement of blood flow, examination of changes in the extracellular matrix (not discussed in the review) and cell death (apoptosis section). The intent is to suggest a synthesis of the available independent toolbox for PET and MRI into hybrid PET/MRI.

1.4 Hybrid PET/MR technology

In Fig 1-2 the sensitivity, spatial resolution, and approximate maximum sample diameter of PET and MRI are compared and contrasted with other major imaging modalities (SPECT, CT and optical) for large animal and human imaging. It should be emphasized that hybrid PET/MRI is a convergence of PET and MRI and unlike PET/CT, which is a sequential acquisition technology, hybrid PET/MRI allows simultaneous acquisition over the same anatomical site. As such, although both PET and MRI are mature technologies when used independently, their combination with hybrid PET/MRI adds a distinct additional nuance that may take many years to explore and determine the value of hybrid PET/MRI over sequential PET and MRI.

The engineering feat of integrating a PET ring into the bore of an MRI required a major redesign of whole-body PET technology[125]. The equipment challenges that remain include a) optimization of the RF/MRI receive coils to reduce the attenuation of the PET signal while maintaining similar performance to dedicated MRI only coils and b) MR-based PET attenuation correction (MRAC) that compares well with CT-based PET attenuation correction (CTAC). However, it has been shown that artifacts and misalignment can impact quantitative accuracy of PET imaging by up to 6%[72,126]. One of the contributing factors is that the MRAC is often done during breath hold while PET data is acquired continuously. Lassen, et al, suggest that this can be corrected by taking μmaps at several respiratory phases or at the end of the exam[127]. It should also be noted that contrast administration could lead to misclassification of tissue[128]. A recent publication demonstrated high MR performance and low PET signal attenuation with a 32-channel RF array designed prospectively for cardiac PET/MRI[129]. Furthermore, MR-derived attenuation correction of the heart using manufacturer-provided software shows excellent correlation with corrections using CT[125,130,131].

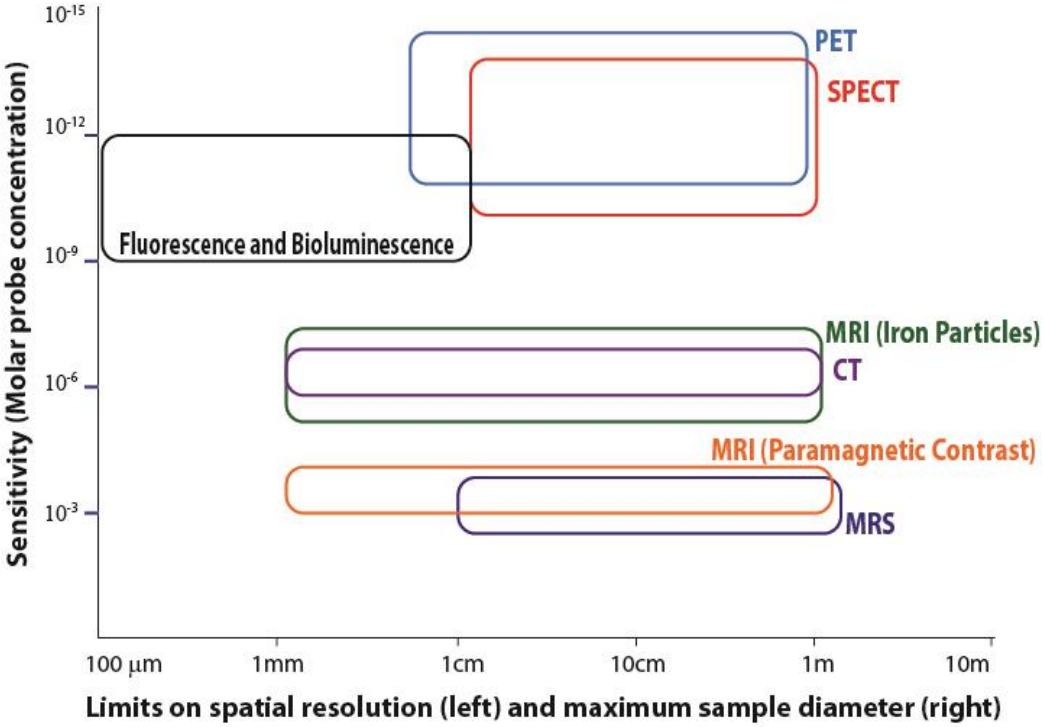

Figure 1-2: Comparison of the capability of different large animal and human molecular imaging modalities.

This figure uses a log-log scale of sensitivity on the vertical axis and spatial resolution on the horizontal axis to demonstrate the capabilities of several imaging modalities. The limit on spatial resolution is shown as the left edge of each shape, while the approximate maximum sample size, which is dependent on both instrument design and signal attenuation, is shown as the right edge. The height of each shape shows the range of sensitivity estimates. This figure was first published by Goldhawk et al, using data from several sources and is used with permission. [132–139]

1.4.1 Hybrid PET/MR in cardiology

The major limitation in standalone PET (i.e. sequential PET/CT) has been the collection of data while the heart moves through the combined cardiac and respiratory cycles. This is in contrast to cardiac MRI, wherein ECG synchronization of the cardiac cycle can be

combined with breath hold or respiratory gating[140]. However, respiratory gating of PET results in loss of 50% of the data and dividing the cardiac cycle into eight phases results in a total loss of 15/16th of the collected data for each component phase. Methods have been developed to register cardiac MR images taken at different times in the respiratory cycle[141,142] but to date they have not been effectively used to reduce/eliminate the effect of motion on the PET data without sacrificing some MRI capabilities[143–146]. It is possible that the respiratory and cardiac motion of the heart could be tracked by MRI (e.g. with 3D navigator echoes and motion sensitive MRI acquisitions) and PET lines of response shifted to a fixed cardiac location (e.g. end diastole at functional residual capacity)[147].

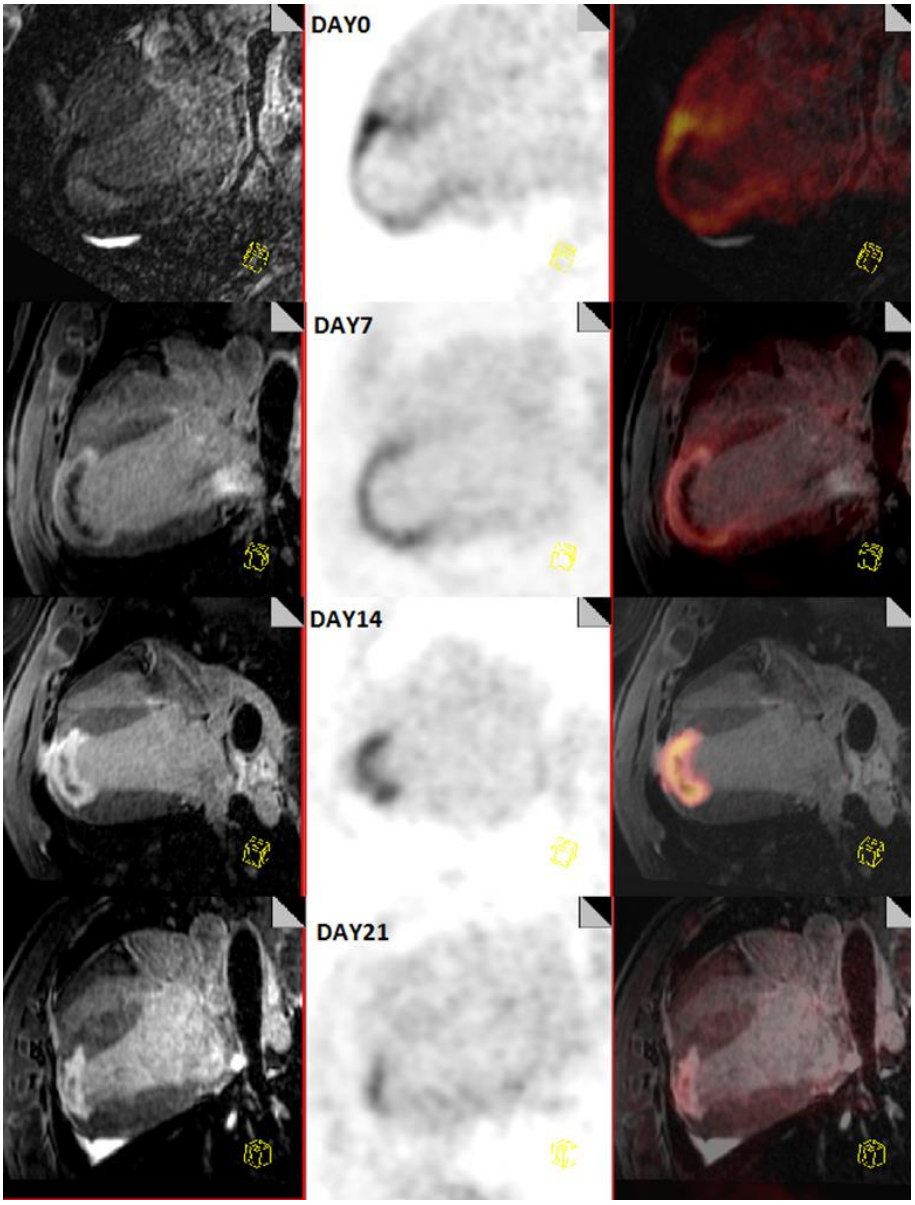

Figure 1-3: Longitudinal comparison of inflammation post-MI with PET/MR in a canine model.

This figure shows the progression of a myocardial infarction from day 0 (top) to day 21 (bottom). On the left are a multiplanar reconstruction of 3D T1-weighted images showing a 4-chamber view of the heart, acquired 20 minutes after a bolus injection of Gd-DTPA, in the middle is an ^{18}F-FDG image and on the right is a combined PET/MR image. Myocardial glucose uptake is suppressed by lipid infusion and heparin injection. These images show that the areas of inflammation decrease over time.

Accurate registration to MRI is needed to effectively implement partial volume correction of cardiac PET. Although conceptually simultaneous PET/MRI over the heart has the needed information this has yet to be achieved. Fig 1-3 shows the importance of PET registration to MR to relate the extent of inflammation to the post-MI tissue types defined by contrast-enhanced MRI. Also, with good suppression of normal ^{18}F-FDG myocyte uptake, it is only by MRI registration that the extent of ^{18}F-FDG uptake associated with the different post-MI tissue types can be identified. The appeal of "perfect" registration is shown in Fig 1-4 where the FDG-PET and post contrast MRI images are perfectly registered as the data was taken after euthanasia[119]. Notice the potential for sub transmural PET signal localization.

Figure 1-4: Post-mortem images of the left ventricle in a canine model. Hybrid PET/MRI after constant simultaneous infusion of FDG and Gd-DTPA in a large animal model of inflammation Post MI.

Registration is "Perfect" as the PET/MRI were acquired post-euthanasia. Arrows indicate center of infarct (blue) and edges of infarct (orange). Notice that inflammation by PET extends beyond the infarct into the "remote" left ventricular myocardium but is not transmural in this "remote" region. Uptake of FDG in the "remote" myocardial tissue PET images could be further improved by MRI guided partial volume correction. Suppression of myocardial glucose uptake was achieved through lipid infusion, heparin injection and fasting.

1.4.2 Future opportunities with hybrid cardiac PET/MRI

Without marked improved in registration between PET and MRI than what is possible today, the use of PET radiopharmaceuticals was dependent on low (but not zero) non-specific binding for anatomical localization of signal. However, with automatic registration of the MRI image to the PET distribution, PET probes without non-specific binding can now be developed and used. For example, this enables the tracking of PET labelled cells. As outlined in the section “Injecting Labeled Inflammatory Cells”, the tracking of ^{89}Zr labeled cells would be possible if hybrid PET/MRI reliably registered the PET and MRI images whereas this may not be reliably done with PET/CT or sequential PET/MR due to the lack of anatomical information from the ^{89}Zr cells and the lack of soft tissue contrast of CT. ^{89}Zr with its 3.3 day half-life is attractive for longitudinal imaging since it can be tracked within the body for as long as 3 weeks[148].

1.4.3 Constant Infusion Protocol

A constant infusion approach to tracer delivery has been hypothesized to lead to an equilibrium concentration of the tracer and has been used for dynamic brain glucose metabolism measurements[149,150]. This has also been applied in the heart to measure cardiac function and glucose metabolism during hypoxia[151]. The constant infusion provides the equilibrium needed to see a change in glucose metabolism when hypoxia is applied. The time at which equilibrium is reached has not been quantified. Furthermore, a constant infusion may allow tracers to enter low-flow areas such as the IOT[43]. In combination with the previously mentioned PET/MRI techniques, a combined constant infusion of MRI contrast agents and PET tracers would allow for penetration of low flow regions such as the microvascular obstruction.

1.4.4 Hybrid PET/MRI protocols

An opportunity and challenge for hybrid PET/MRI is to optimize the combined PET and MRI protocols. One of the issues post-MI is delivery to an area of IOT. A bolus injection of gadolinium chelate does not penetrate IOT and hence allows its discrimination from the INOT. Although this lack of penetration of the MR contrast agent allows the

discrimination of the three post-MI tissue types, the lack of penetration of ^{18}F-FDG blocks information regarding the presence or absence of inflammatory cells in the IOT. A bolus injection of ^{18}F-FDG does not penetrate this zone sufficiently to give inflammatory cells the opportunity to sequester the tracer[119]. A novel and now possible approach would be to maintain a high blood concentration of tracer for a sufficiently long period of time to allow increased delivery of the tracer, even to the regions of severely compromised flow. This could be accomplished by a constant infusion of ^{18}F-FDG and a Gd-chelate. If the Gd-chelate were able to penetrate the IOT during a 40 min infusion, then it is likely that ^{18}F-FDG would also be delivered sufficiently to somewhat penetrate IOT and INOT. A slow infusion would allow accurate 3D T1 maps to be collected as tissue concentrations would not change appreciably during the acquisition and this would match the 3D data collection of ^{18}F-FDG-PET. Normally 3D T1 maps cannot be accurately collected after a bolus injection of Gd-chelate. This would provide unprecedented 3D data matched in time and space between ^{18}F-FDG-PET and Gd-chelate/MRI. As the concentration of Gd-chelate would not change appreciably during the 3D T1 map data collection, subtle changes in the extra-cellular volume could be detected in the remote myocardium[151–153].

One of the major differences between PET and MRI is the flexibility in binning the data after the acquisition. PET data can be collected in list-mode, where the location and time of individual PET events is recorded in a large raw data file. If physiological timing markers are also recorded, it is possible to reconstruct PET images at any point within the respiratory and cardiac phases. Hence, allowing the elimination of data corrupted by motion of either physiological origin and/or associated with patient bulk movement. MRI data is typically collected in a rigid format corresponding to a patterned projection in k-space and MRI images are difficult to accurately reconstruct from an incomplete set of k-space data. Recently this constraint of MRI has been addressed using a novel approach to randomize k-space data collection that would then allow matching in time of MRI with “random” PET list-mode image creation[154–157]. This will harmonize the way PET and MRI data is collected and used; which is important to fully realize the benefits of simultaneous acquisition such as improved PET to MRI registration.

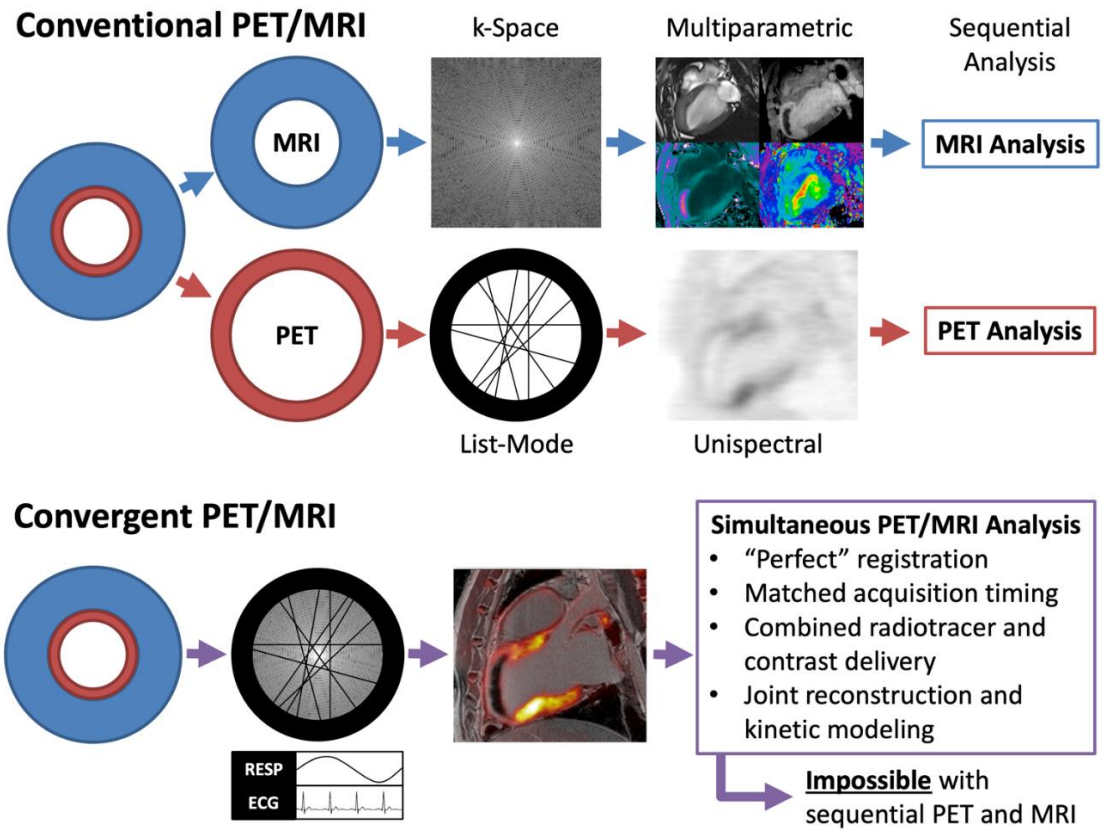

Figure 1-5: Conventional vs convergent approaches to cardiac hybrid PET/MRI protocols.

To date, most clinical applications of hybrid PET/MRI in cardiology have adopted protocols that were developed for sequential PET/MRI, which results in good PET and MRI images that are analyzed separately. However, good registration of PET and MRI is not always achieved. With an approach which treats hybrid PET/MRI as a new imaging modality, achieved through the convergence of the two modalities, cardiac PET/MR images could be achieved which are not possible with sequential acquisitions. An example of this potential is shown in Figure 1-4.

1.4.5 Hybrid PET/MRI as a convergent technology

The convergence of PET and MRI will provide medical imaging with a new imaging modality. To achieve convergence there is a need for near perfect registration between PET and MRI as well as other factors outlined in Fig 1-5. A major limitation of PET is the one common signal (511 keV annihilation radiation) for all PET radioisotopes. This limits PET to a single radiopharmaceutical during any one data collection whereas in MRI there is the capacity to collect a variety of image contrasts based on different pulse sequences and interactions of protons with static and varying magnetic fields. For example, a post-MI study that requires both blood flow (e.g. ^{13}N ammonia) and inflammation (e.g. ^{18}F-FDG) by PET is difficult to achieve in a single imaging session. One possibility is to perform myocardial blood flow measurements using contrast-enhanced MRI[158] or BOLD MRI[159] which could reduce acquisition time and dose during cardiac examinations, as shown in Fig 1-6. This would be especially useful in diseases such as cardiac sarcoidosis where it would be advantageous to study blood flow and inflammation[102,160]. Reducing the acquisition time and dose would allow investigators to try new studies which would presently not be possible due to the length of the scan and the patient's ability to withstand it. One potential with hybrid PET/MRI is the use of the Tofts model[161] to quantify K_{trans}, a transfer constant related to tissue perfusion, during a constant infusion and how this relates to PET tracer dynamics[162]. The replacement of FDG-PET with glucoCEST is intriguing but issues with sensitivity of CEST and the fact that different glucose pools are being detected requires significant development[163]. CEST measurements sensitive to creatine kinase, hyaluronan synthesis, or pH may hold more promise in combination with complementary PET imaging.

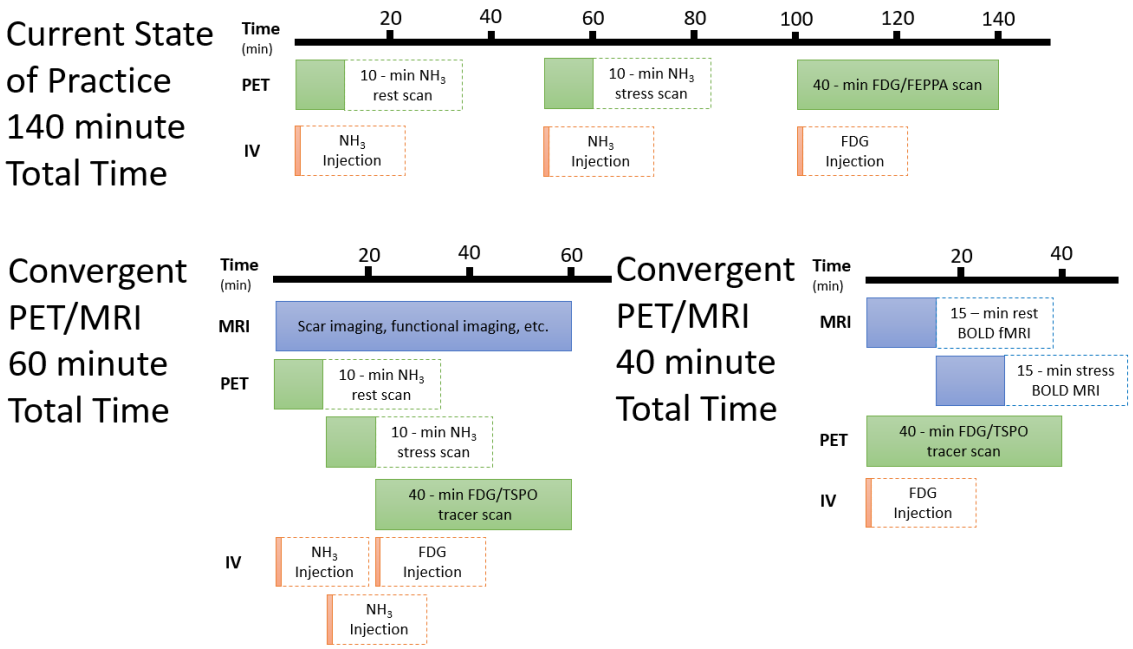

Figure 1-6: Imaging myocardial perfusion reserve and inflammation with a convergent PET/MRI protocol.

Using the current state of practice, imaging myocardial perfusion and inflammation sequentially would take approximately 140 minutes, unacceptably prolonging the exam. Using convergent technology, this could be reduced to 60 minutes with near perfect registration, using a rapid dual-injection for ^{13}N-ammonia for measuring rest and stress blood flow, as suggested by Rust et al.[104] However, when injecting the tracer beforehand or using alternate tracer delivery, and using BOLD MRI instead of PET[164], it could be reduced even further, to 30 minutes or less.

1.4.6 Artificial intelligence with hybrid PET/MRI

In an extensive state-of-the-art review on artificial intelligence in cardiovascular disease, cardiac PET and cardiac MRI are treated separately[165]. The major limitation for the application of AI to hybrid PET/MRI for the detection of disease is the absence of a large cohort of "ground truth" data needed for the training sets. Some of the outcomes of AI as applied separately to PET and MRI suggest some applications to improve the quality of

information. For example, the 2016 Kuggle Data Science Bowl competition provides more than 1,000 cardiac cine MR data sets and the AI developed has shown that left ventricular end-systolic and end-diastolic volumes can be determined[166]. If this approach could be used to identify these volumes and also the epicardial and the endocardial borders at the same respiratory and cardiac phases as in the PET data simultaneously collected, then this could allow identification of the location of these cardiac structures in the PET images, even if in the PET images these structures were not visible. Not only would this automation reduce image analysis it would also allow the identification of the same structures in the PET data. Unfortunately, to the best of our knowledge, the needed PET ground truth data are not available, even for the development of machine learning approaches to assist in the determination of diagnostic values. It would be of considerable value if there were cardiac PET/CT and MRI data of the same patients even if acquired separately. For example, the Alzheimer's Disease Neuroimaging Initiative archived data sets include brain PET and MRI images of the same patient and would allow sufficient training sets to develop AI for joint PET/MRI reconstructions, partial volume correction, MR-derived attenuation correction and dose reduction, to name a few. These findings, in turn, could be tested with true hybrid PET/MRI data sets. Unfortunately, there are no such large data sets for separate cardiac PET and cardiac MRI on the same patients. It seems inevitable that the data would have to be collected on hybrid PET/MRI systems to test joint reconstruction, kinetic modeling and partial volume correction. As we have suggested already, optimizing AI outcomes of combined simultaneously acquired PET and MRI data will require data collection protocols which are very different than what is collected for standalone MRI. Both supervised and unsupervised approaches should be explored with respect to combined connected model analysis. The number of fitted parameters should be small and restricted in supervised approaches whereas in the unsupervised approach many more parameters can be investigated[165]. Another example would be the use of MRI guided PET reconstruction to reduce radiation dose by constraining the PET reconstruction to reduce the effect of noise.

A common AI approach is to try to simulate another, gold-standard modality, e.g. generating a pseudo CT with MRI for MRAC or predicting Gd-enhanced images with non-contrast MRI. Can we use this approach with matched MRI and PET to predict

regions of inflammation? That is, can we get enough information from multiparametric MRI (Gd-enhanced, blood flow, T2-weighted, T2*-weighted, and CEST) to predict where inflammation should be and validated with FDG-PET or TSPO-PET?

1.5 Preclinical benchmarking using animal models

Significant advances in cardiac imaging have often required the use of animal models allowing for the establishment of ground truth directly from tissue. Both small animal and large animal models have been effective. For example, most recently, Thackeray et al[109] used an infarct mouse model to test the use of a TSPO-PET ligand before moving to human studies. In contrast, large animal models, although more expensive, are needed since the physiology of the models better reflects the human condition and/or the imaging cannot be easily scaled up to humans if a small animal model were used. For example, most recently, Yang et al developed cardiac BOLD applications in the canine as a rodent model would not have been of value in developing cardiac BOLD for human application[65]. Translation of therapeutic interventions from rodents to humans has, in general, had a high failure rate[167]. For the development of imaging biomarkers, this problem is exacerbated by the non-linear scaling from rodent to human imaging modalities[92,137–139]. In contrast, large animal models have a reasonable translation record[168,169] and little or no issues with scaling of PET and MRI since studies use human imaging equipment. Regarding coronary artery disease and inflammation, a) infarcted myocardium results in an increase in the distribution volume of Gd-DTPA, characteristic of permanently damaged myocardium, in dogs and humans[42,47,170–172] but the increase in the distribution volume in rats also occurs in reversibly damaged tissue[173]; b) the time course of neutrophil and macrophage activity following AMI is similar in dogs and humans, but different in rodents[15,174–176]; c) inflammatory cell response post AMI has the same cell markers in humans and dogs[6,177]; and d) the course of hemorrhage and iron precipitation following AMI is similar between humans and dogs. There has been some debate regarding the use of porcine rather than canine models for the study of the evolution of acute infarction. The presence of collateral vessels in the canine myocardium is more relevant to AMI in older humans (>50 yrs of age) while the lack of collaterals in pigs provides a better model for sudden death. Since progressive heart disease following

AMI is predominantly seen in older individuals, the canine model is superior for imaging inflammation post-MI[178,179].

1.6 Summary

Standalone myocardial post-MI MRI can provide discrimination of the three tissue types: IOT, INOT and RT. It also can provide functional information, extent of edema and extent of hemorrhage. It can partially track/detect inflammatory cells if they can be labelled with iron particles or ^{19}F. Standalone PET (i.e. PET/CT) can quantify inflammation with ^{18}F-FDG or TSPO-targeted tracers, but not specifically with respect to pro-inflammatory vs. the anti-inflammatory signal and, in the case of ^{18}F-FDG, requires myocardial suppression which is not always successful. A hybrid PET/MR approach including a contrast agent sensitive to anti-inflammatory signal may be able to separate the pro- and anti-inflammatory signals. Hybrid PET/MRI, even with its current state of non-optimal cardiac registration, provides a complementary story that will allow the relationship between scar formation and inflammation to be discovered as is being done in other cardiac conditions such as sarcoidosis[102,180].

To date, the primary use of hybrid PET/MRI is to perform combined PET and MRI procedures in a single procedure primarily as a tool of convenience rather than as a means of greater understanding of pathophysiological mechanisms. To achieve the latter, there are four important areas of development: that are required: a) far better registration than what is available today that does not significantly sacrifice the acquisition of PET data; b) synchronized, simultaneous acquisition of PET and MRI where MRI must have the same flexibility as list-mode PET c) integration of quantitative and novel MRI techniques such as cardiac BOLD; and d) an approach that combines the large number of PET probes and determinants of MRI contrast in novel synergistic ways (see Fig 1-1). This will not only be impactful with currently available PET probes but would make it possible to develop new PET probes or combined PET/MRI strategies that could quantitate and differentiate between the different inflammatory cell phenotypes. Discrimination between the pro- and anti-inflammatory processes in the three tissue types

post-MI will be critical for the development of inflammatory therapies and for implementation in the individual patient.

1.7 Research Objectives

In this thesis, primarily the constant infusion approach to tracer and contrast agent delivery will be examined. Previously, a constant infusion of PET tracers has been used to examine cardiac metabolism during hypoxia[151] in a porcine model and a constant infusion of Gd-DTPA has been used to examine perfusion in a canine model with MRI only[43]. However, they have not been combined in one model or post-MI while imaging with PET/MRI. It has also not been determined whether the constant infusion approach leads to the same results of extracellular volume and glucose metabolism as a clinical bolus injection and whether it is safe to combine FDG and Gd-DTPA in the same syringe. This leads to several research objectives:

1. Since the safety of combining Gd-DTPA and FDG in one syringe has not been shown, the first goal in this thesis was to show that combining these is safe since they will be combined to complete the following objectives.
2. Before applying the constant infusion method in a model of myocardial infarction, it had to be shown at baseline that the glucose metabolism and extracellular volume were not significantly different. Thus, the second objective was to determine whether the results from a bolus injection and a constant infusion are the same.
3. The third objective of this thesis was to measure glucose metabolism and extracellular volume post-myocardial infarction in all regions of the heart including RT, INOT and IOT.
4. The fourth objective was to determine whether a long constant infusion of 150 minutes can penetrate the IOT with both FDG and Gd-DTPA.
5. The fifth and final objective was to determine whether the current technique to suppress myocardial glucose uptake of fasting, heparin injection and lipid infusion is effective.

Overall, this will validate the constant infusion approach with hybrid PET/MRI and it may allow measurements of inflammation in the RT, INOT and IOT.

1.8 Thesis Outline

1.8.1 Simultaneous measurements of myocardial glucose metabolism and extracellular volumes with hybrid PET/MRI using concurrent injections of Gd-DTPA and [^{18}F]FDG

In Chapter two, Simultaneous measurements of myocardial glucose metabolism and extracellular volumes with hybrid PET/MRI using concurrent injections of Gd-DTPA and [18F]FDG, the first two objectives were addressed: the safety of combining gadolinium-based contrast agent and FDG in one syringe and comparing the results from a bolus injection and a constant infusion at baseline. FDG and Gd-DTPA were combined in a single syringe for 90 minutes and analysed for changes in pH and radiochemical purity and identity with radiometric thin layer chromatography. In addition to that, 6 healthy canines were imaged with PET/MRI with 3 different injection protocols of combined Gd-DTPA and FDG: 60-minute constant infusion, bolus injection and bolus injection followed by a 30-minute constant infusion. All of these were done without suppression and then repeated with suppression by heparin injection and lipid infusion. Note that animals were fasted in either case as a requirement for anesthesia[181].

1.8.2 Tracking the progress of inflammation with PET/MRI in a canine model of myocardial infarction

In chapter three, Tracking the progress of inflammation with PET/MRI in a canine model of myocardial infarction, the third objective, measuring glucose metabolism and extracellular volume over time post-MI, was addressed. Eight animals were imaged at baseline and on days 3, 7, 14, 21 and 43 with hybrid PET/MRI during a constant infusion of Gd-DTPA and FDG. Glucose metabolism and extracellular volume were measured in RT, INOT and IOT. The values of both are compared among days so that a timeline of inflammation can be established in all tissues[182].

1.8.3 Investigating the effects of myocardial glucose suppression on the incorporation of FDG into pro-inflammatory cells in a canine model of myocardial infarction

In chapter four, Investigating the effects of myocardial glucose suppression on the incorporation of FDG into pro-inflammatory cells in a canine model of myocardial

infarction, the fourth and fifth objectives were addressed. As such, the degree of penetration of tracer and contrast agent into the IOT was measured and the effect of myocardial glucose suppression on inflammatory cells was investigated. To determine the impact of myocyte glucose suppression, the constant infusion was increased from 60 min to 150 minutes in 6 animals studied at baseline and at day 5 post-MI. This allowed measurements of glucose metabolism without suppression to be measured in the infarcted tissue for the first 40 minutes of the constant infusion. This result was then compared to the glucose uptake in this infarcted tissue during active suppression for the period of 50 to 90 minutes and then again after the suppression for the period from 100 to 150 minutes.

1.9 References

1. Braunwald E. Shattuck lecture--cardiovascular medicine at the turn of the millennium: triumphs, concerns, and opportunities. *N Engl J Med* 1997;337:1360-1369. doi:10.1056/NEJM199711063371906

2. Braunwald E. Research advances in heart failure: A compendium. *Circ Res* 2013;113:633-645. doi:10.1161/CIRCRESAHA.113.302254

3. Eitel I, Kubusch K, Strohm O, Desch S, Mikami Y, De Waha S, et al. Prognostic value and determinants of a hypointense infarct core in T2-weighted cardiac magnetic resonance in acute reperfused ST-elevation- myocardial infarction. *Circ Cardiovasc Imaging* 2011;4:354-362. doi:10.1161/CIRCIMAGING.110.960500

4. Pfeffer MA, Braunwald E. Ventricular remodeling after myocardial infarction: Experimental observations and clinical implications. *Circulation* 1990;81:116-172. doi:10.1161/01.CIR.81.4.1161

5. Ganame J, Messalli G, Dymarkowski S, Rademakers FE, Desmet W, Van De Werf F, et al. Impact of myocardial haemorrhage on left ventricular function and remodelling in patients with reperfused acute myocardial infarction. *Eur Heart J*

2009;30:1440-1449. doi:10.1093/eurheartj/ehp093

6. Kali A, Cokic I, Tang R, Dohnalkova A, Kovarik L, Yang HJ, et al. Persistent Microvascular Obstruction after Myocardial Infarction Culminates in the Confluence of Ferric Iron Oxide Crystals, Proinflammatory Burden, and Adverse Remodeling. *Circ Cardiovasc Imaging* 2016;9:e004996. doi:10.1161/CIRCIMAGING.115.004996

7. Kali A, Tang RLQ, Kumar A, Min JK, Dharmakumar R. Detection of Acute Reperfusion Myocardial Hemorrhage with Cardiac MR Imaging: T2 versus T2*. *Radiology* 2013;269:387-395. doi:10.1148/radiol.13122397

8. Kali A, Kumar A, Cokic I, Tang RLQ, Tsaftaris SA, Friedrich MG, et al. Chronic manifestation of postreperfusion intramyocardial hemorrhage as regional iron deposition: A cardiovascular magnetic resonance study with ex vivo validation. *Circ Cardiovasc Imaging* 2013;6:218-228. doi:10.1161/CIRCIMAGING.112.000133

9. Frangogiannis NG. The inflammatory response in myocardial injury, repair, and remodelling. *Nat Rev Cardiol* 2014;11:255-265. doi:10.1038/nrcardio.2014.28

10. Weir RAP, Miller AM, Murphy GEJ, Clements S, Steedman T, Connell JMC, et al. Serum Soluble ST2. A Potential Novel Mediator in Left Ventricular and Infarct Remodeling After Acute Myocardial Infarction. *J Am Coll Cardiol* 2010;55:243-250. doi:10.1016/j.jacc.2009.08.047

11. Fishbein MC, Maclean D, Maroko PR. The histopathologic evolution of myocardial infarction. *Chest* 1978;73:843-849. doi:10.1378/chest.73.6.843

12. Frangogiannis NG, Smith CW, Entman ML. The inflammatory response in myocardial infarction. *Cardiovasc Res* 2002;53:31-47. doi:10.1016/S0008-6363(01)00434-5

13. Hofmann U, Knorr S, Vogel B, Weirather J, Frey A, Ertl G, et al. Interleukin-13 deficiency aggravates healing and remodeling in male mice after experimental

myocardial infarction. *Circ Hear Fail* 2014;7:822-830. doi:10.1161/CIRCHEARTFAILURE.113.001020

14. Chatelain P, Latour JG, Tran D, de Lorgeril M, Dupras G, Bourassa M. Neutrophil accumulation in experimental myocardial infarcts: Relation with extent of injury and effect of reperfusion. *Circulation* 1987;75:1083-1090. doi:10.1161/01.CIR.75.5.1083

15. Dewald O, Ren G, Duerr GD, Zoerlein M, Klemm C, Gersch C, et al. Of mice and dogs: species-specific differences in the inflammatory response following myocardial infarction. *Am J Pathol* 2004;164:665-677. doi:10.1016/S0002-9440(10)63154-9

16. Epelman S, Lavine KJ, Randolph GJ. Origin and Functions of Tissue Macrophages. *Immunity* 2014;41:21-35. doi:10.1016/j.immuni.2014.06.013

17. Lavine KJ, Epelman S, Uchida K, Weber KJ, Nichols CG, Schilling JD, et al. Distinct macrophage lineages contribute to disparate patterns of cardiac recovery and remodeling in the neonatal and adult heart. *Proc Natl Acad Sci* 2014;111:16029-16034. doi:10.1073/pnas.1406508111

18. Serhan CN, Savill J. Resolution of inflammation: The beginning programs the end. *Nat Immunol* 2005;6:1191-1197. doi:10.1038/ni1276

19. Warnatsch A, Ioannou M, Wang Q, Papayannopoulos V. Neutrophil extracellular traps license macrophages for cytokine production in atherosclerosis. *Science (80-)* 2015;349:316-320. doi:10.1126/science.aaa8064

20. Yan Y, Gause KT, Kamphuis MMJ, Ang CS, O'Brien-Simpson NM, Lenzo JC, et al. Differential roles of the protein corona in the cellular uptake of nanoporous polymer particles by monocyte and macrophage cell lines. *ACS Nano* 2013;7:10960-10970. doi:10.1021/nn404481f

21. Bronte V, Pittet MJ. The spleen in local and systemic regulation of immunity. *Immunity* 2013;39:806-818. doi:10.1016/j.immuni.2013.10.010

22. Swirski FK, Nahrendorf M, Etzrodt M, Wildgruber M, Cortez-Retamozo V, Panizzi P, et al. Identification of splenic reservoir monocytes and their deployment to inflammatory sites. *Science (80-)* 2009;325:612-616. doi:10.1126/science.1175202

23. Dutta P, Nahrendorf M. Monocytes in myocardial infarction. *Arterioscler Thromb Vasc Biol* 2015;35:1066-1070. doi:10.1161/ATVBAHA.114.304652

24. Hettinger J, Richards DM, Hansson J, Barra MM, Joschko AC, Krijgsveld J, et al. Origin of monocytes and macrophages in a committed progenitor. *Nat Immunol* 2013;14:821-830. doi:10.1038/ni.2638

25. Koelwyn GJ, Corr EM, Erbay E, Moore KJ. Regulation of macrophage immunometabolism in atherosclerosis. *Nat Immunol* 2018;19:526-537. doi:10.1038/s41590-018-0113-3

26. Tavakoli S, Zamora D, Ullevig S, Asmis R. Bioenergetic profiles diverge during macrophage polarization: Implications for the interpretation of 18F-FDG PET imaging of atherosclerosis. *J Nucl Med* 2013;54:1661-1667. doi:10.2967/jnumed.112.119099

27. Dobaczewski M, Xia Y, Bujak M, Gonzalez-Quesada C, Frangogiannis NG. CCR5 signaling suppresses inflammation and reduces adverse remodeling of the infarcted heart, mediating recruitment of regulatory T cells. *Am J Pathol* 2010;176:2177-2187. doi:10.2353/ajpath.2010.090759

28. Frangogiannis NG. Regulation of the inflammatory response in cardiac repair. *Circ Res* 2012;110:159-173. doi:10.1161/CIRCRESAHA.111.243162

29. Thackeray JT, Bengel FM. Molecular Imaging of Myocardial Inflammation With Positron Emission Tomography Post-Ischemia: A Determinant of Subsequent Remodeling or Recovery. *JACC Cardiovasc Imaging* 2018;11:1340-1355. doi:10.1016/j.jcmg.2018.05.026

30. Seropian IM, Toldo S, Van Tassell BW, Abbate A. Anti-inflammatory strategies

for ventricular remodeling following St-segment elevation acute myocardial infarction. *J Am Coll Cardiol* 2014;63:1593-1603. doi:10.1016/j.jacc.2014.01.014

31. Satomi T, Ogawa M, Mori I, Ishino S, Kubo K, Magata Y, et al. Comparison of Contrast Agents for Atherosclerosis Imaging Using Cultured Macrophages: FDG Versus Ultrasmall Superparamagnetic Iron Oxide. *J Nucl Med* 2013;54:999-1004. doi:10.2967/jnumed.112.110551

32. Zhu L, Zhao Q, Yang T, Ding W, Zhao Y. Cellular metabolism and macrophage functional polarization. *Int Rev Immunol* 2015;34:82-100. doi:10.3109/08830185.2014.969421

33. Recalcati S, Locati M, Marini A, Santambrogio P, Zaninotto F, De Pizzol M, et al. Differential regulation of iron homeostasis during human macrophage polarized activation. *Eur J Immunol* 2010;40:824-835. doi:10.1002/eji.200939889

34. Corna G, Campana L, Pignatti E, Castiglioni A, Tagliafico E, Bosurgi L, et al. Polarization dictates iron handling by inflammatory and alternatively activated macrophages. *Haematologica* 2010;95:1814-1822. doi:10.3324/haematol.2010.023879

35. Goldhawk D, Gelman N, Sengupta A, Prato F. The Interface Between Iron Metabolism and Gene-Based Iron Contrast for MRI. *Magn Reson Insights* 2015;8:9-14. doi:10.4137/mri.s23555

36. Young AA, Kramer CM, Ferrari VA, Axel L, Reichek N. Three-dimensional left ventricular deformation in hypertrophic cardiomyopathy. *Circulation* 1994;90:854-867. doi:10.1161/01.CIR.90.2.854

37. Everaars H, Robbers LFHJ, Götte M, Croisille P, Hirsch A, Teunissen PFA, et al. Strain analysis is superior to wall thickening in discriminating between infarcted myocardium with and without microvascular obstruction. *Eur Radiol* 2018;28:5171-5181. doi:10.1007/s00330-018-5493-0

38. Lotz J, Meier C, Leppert A, Galanski M. Cardiovascular Flow Measurement with

Imaging : Basic Facts and Implementation. *RadioGraphics* 2002;22:651-671.

39. Vasanawala SS, Hanneman K, Alley MT, Hsiao A. Congenital heart disease assessment with 4D flow MRI. *J Magn Reson Imaging* 2015;42:870-886. doi:10.1002/jmri.24856

40. Garcia J, Sheitt H, Bristow MS, Lydell C, Howarth AG, Heydari B, et al. Left atrial vortex size and velocity distributions by 4D flow MRI in patients with paroxysmal atrial fibrillation: Associations with age and CHA2 DS2 -VASc risk score. *J Magn Reson Imaging* 2019.

41. Thornhill RE, Prato FS, Pereira RS, Wisenberg G, Sykes J. Examining a canine model of stunned myocardium with Gd-DTPA-enhanced MRI. *Magn Reson Med* 2001;45:864-871. doi:10.1002/mrm.1115

42. Thornhill RE, Prato FS, Wisenberg G, White J a, Nowell J, Sauer A. Feasibility of the single-bolus strategy for measuring the partition coefficient of Gd-DTPA in patients with myocardial infarction: independence of image delay time and maturity of scar. *Magn Reson Med* 2006;55:780-789. doi:10.1002/mrm.20830

43. Pereira RS, Prato FS, Sykes J, Wisenberg G. Assessment of myocardial viability using MRI during a constant infusion of GD-DTPA: Further studies at early and late periods of reperfusion. *Magn Reson Med* 1999;42:60-68. doi:10.1002/(SICI)1522-2594(199907)42:1<60::AID-MRM10>3.0.CO;2-9

44. Flacke SJ, Fischer SE. Measurement of the Gadopentetate Dimeglumine Partition Coefficient in Human Myocardium in Vivo: Normal Distribution and Elevation in Acute and Chronic …. *Radiology* 2001;218:703-710.

45. Kim RJ, Fieno DS, Parrish TB, Harris K, Chen EL, Simonetti O, et al. Relationship of MRI delayed contrast enhancement to irreversible injury, infarct age, and contractile function. *Circulation* 1999;100:1992-2002. doi:10.1161/01.CIR.100.19.1992

46. Lekx KS, Prato FS, Sykes J, Wisenberg G. The Partition Coefficient of Gd-DTPA

Reflects Maintained Tissue Viability in a Canine Model of Chronic Significant Coronary Stenosis. *J Cardiovasc Magn Reson* 2004;6:33-42. doi:10.1081/JCMR-120027803

47. Pereira RS, Wisenberg G, Prato FS, Yvorchuk K. Clinical assessment of myocardial viability using MRI during a constant infusion of Gd-DTPA. *Magn Reson Mater Physics, Biol Med* 2000;11:104-113. doi:10.1016/S1352-8661(00)00093-4

48. Wu KC, Heldman AW, Brinker JA, Hare JM, Lima JAC. Microvascular obstruction after nonsurgical septal reduction for the treatment of hypertrophic cardiomyopathy. *Circulation* 2001;104:1868. doi:10.1161/hc4001.096355

49. Kim RJ, Wu E, Rafael A, Chen EL, Parker MA, Simonetti O, et al. The Use of Contrast-Enhanced Magnetic Resonance Imaging to Identify Reversible Myocardial Dysfunction. *N Engl J Med* 2000;343:1445-1453. doi:10.1016/s1062-1458(01)00166-0

50. Kali A, Cokic I, Tang RLQ, Yang HJ, Sharif B, Marbán E, et al. Determination of location, size, and transmurality of chronic myocardial infarction without exogenous contrast media by using cardiac magnetic resonance imaging at 3 T. *Circ Cardiovasc Imaging* 2014;7:471-481. doi:10.1161/CIRCIMAGING.113.001541

51. Kali A, Choi EY, Sharif B, Kim YJ, Bi X, Spottiswoode B, et al. Native T1 Mapping by 3-T CMR Imaging for Characterization of Chronic Myocardial Infarctions. *JACC Cardiovasc Imaging* 2015;8:1019-1030. doi:10.1016/j.jcmg.2015.04.018

52. Johns JA, Leavitt MB, Newell JB, Yasuda T, Leinbach RC, Gold HK, et al. Quantitation of acute myocardial infarct size by nuclear magnetic resonance imaging. *J Am Coll Cardiol* 1990;15:143-149. doi:10.1016/0735-1097(90)90190-Z

53. Wang G, Yang H-J, Kali A, Cokic I, Tang R, Xie G, et al. Influence of Myocardial

Hemorrhage on Staging of Reperfused Myocardial Infarctions With T2 Cardiac Magnetic Resonance Imaging. *JACC Cardiovasc Imaging* 2019;12:693-703. doi:10.1016/j.jcmg.2018.01.018

54. Liu L, Alizadeh K, Donnelly SC, Dassanayake P, Hou TT, McGirr R, et al. MagA expression attenuates iron export activity in undifferentiated multipotent P19 cells. *PLoS One* 2019;14:1-19. doi:10.1371/journal.pone.0217842

55. Moon BF, Iyer SK, Hwuang E, Solomon MP, Hall AT, Kumar R, et al. Iron imaging in myocardial infarction reperfusion injury. *Nat Commun* 2020;11:1-14. doi:10.1038/s41467-020-16923-0

56. Jerosch-Herold M, Seethamraju RT, Swingen CM, Wilke NM, Stillman AE. Analysis of myocardial perfusion MRI. *J Magn Reson Imaging* 2004;19:758-770. doi:10.1002/jmri.20065

57. Bellamy DD, Pereira RS, McKenzie CA, Prato FS, Drost DJ, Sykes J, et al. Gd-DTPA bolus tracking in the myocardium using T1 fast acquisition relaxation mapping (T1 FARM). *Magn Reson Med* 2001;46:555-564. doi:10.1002/mrm.1227

58. Ishida M, Schuster A, Morton G, Chiribiri A, Hussain S, Paul M, et al. Development of a universal dual-bolus injection scheme for the quantitative assessment of myocardial perfusion cardiovascular magnetic resonance. *J Cardiovasc Magn Reson* 2011;13:28. doi:10.1186/1532-429X-13-28x

59. Papanastasiou G, Williams MC, Kershaw LE, Dweck MR, Alam S, Mirsadraee S, et al. Measurement of myocardial blood flow by cardiovascular magnetic resonance perfusion: Comparison of distributed parameter and Fermi models with single and dual bolus. *J Cardiovasc Magn Reson* 2015;17. doi:10.1186/s12968-015-0125-1

60. Tong CY, Prato FS, Wisenberg G, Lee TY, Carroll E, Sandler D, et al. Measurement of the extraction efficiency and distribution volume for Gd-DTPA in normal and diseased canine myocardium. *Magn Reson Med* 1993;30:337-346.

doi:10.1002/mrm.1910300310

61. Maddahi J, Packard RRS. Cardiac PET perfusion tracers: Current status and future directions. *Semin Nucl Med* 2014;44:333-343. doi:10.1053/j.semnuclmed.2014.06.011

62. Kunze KP, Rischpler C, Hayes C, Ibrahim T, Laugwitz KL, Haase A, et al. Measurement of extracellular volume and transit time heterogeneity using contrast-enhanced myocardial perfusion MRI in patients after acute myocardial infarction. *Magn Reson Med* 2017;77:2320-2330. doi:10.1002/mrm.26320

63. Schelbert HR, Phelps ME, Huang SC, MacDonald NS, Hansen H, Selin C, et al. N-13 ammonia as an indicator of myocardial blood flow. *Circulation* 1981;63:1259-1272. doi:10.1161/01.CIR.63.6.1259

64. Li D, Dhawale P, Rubin PJ, Haacke EM, Gropler RJ. Myocardial signal response to dipyridamole and dobutamine: Demonstration of the BOLD effect using a double-echo gradient-echo sequence. *Magn Reson Med* 1996;36:16-20. doi:10.1002/mrm.1910360105

65. Yang H-J, Ilkary O, Dey D, Sykes J, Klein M, Butler J, et al. Accurate Needle-Free Assessment of Myocardial Oxygenation for Ischemic Heart Disease. *Sci Transl Med* 2019;11.

66. Zijl PCM Van, Yadav NN. Chemical Exchange Saturation Transfer (CEST): What is in a Name and What Isn't ? *Magn Reson Med* 2011;65:927-948. doi:10.1002/mrm.22761

67. Liu G, Song X, Chan KWY, McMahon MT. Nuts and bolts of chemical exchange saturation transfer MRI. *NMR Biomed* 2013;26:810-828. doi:10.1002/nbm.2899

68. Vinogradov E, Sherry a. D, Lenkinski RE. CEST: From basic principles to applications, challenges and opportunities. *J Magn Reson* 2013;229:155-172. doi:10.1016/j.jmr.2012.11.024

69. Jones CK, Schlosser MJ, Van Zijl PCM, Pomper MG, Golay X, Zhou J. Amide proton transfer imaging of human brain tumors at 3T. *Magn Reson Med* 2006;56:585-592. doi:10.1002/mrm.20989

70. Cai K, Haris M, Singh A, Kogan F, Greenberg JH, Hariharan H, et al. Magnetic resonance imaging of glutamate. *Nat Med* 2012;18:302-306. doi:10.1038/nm.2615

71. Haris M, Nanga RRPR, Singh A, Cai K, Kogan F, Hariharan H, et al. Exchange Rates of Creatine Kinase Metabolites: Feasbility of Imaging Creatine by Chemical Exchange Saturation Transfer MRI. *NMR Biomed* 2013;25:1305-1309. doi:10.1002/nbm.2792.Exchange

72. Lindeman LR, Randtke EA, High RA, Jones KM, Howison CM, Pagel MD. A comparison of exogenous and endogenous CEST MRI methods for evaluating in vivo pH. *Magn Reson Med* 2018;79:2766-2772. doi:10.1002/mrm.26924

73. Jones KM, Randtke EA, Yoshimaru ES, Howison CM, Chalasani P, Klein RR, et al. Clinical Translation of Tumor Acidosis Measurements with AcidoCEST MRI. *Mol Imaging Biol* 2017;19:617-625. doi:10.1007/s11307-016-1029-7

74. Chan KWY, McMahon MT, Kato Y, Liu G, Bulte JWM, Bhujwalla ZM, et al. Natural D-glucose as a biodegradable MRI contrast agent for detecting cancer. *Magn Reson Med* 2012;68:1764-1773. doi:10.1002/mrm.24520

75. Walker-Samuel S, Ramasawmy R, Torrealdea F, Rega M, Rajkumar V, Johnson SP, et al. In vivo imaging of glucose uptake and metabolism in tumors. *Nat Med* 2013;19:1067-1072. doi:10.1038/nm.3252

76. Rivlin M, Horev J, Tsarfaty I, Navon G. Molecular imaging of tumors and metastases using chemical exchange saturation transfer (CEST) MRI. *Sci Rep* 2013;3:3045. doi:10.1038/srep03045

77. Jones KM, Pollard AC, Pagel MD. Clinical applications of chemical exchange saturation transfer (CEST) MRI. *J Magn Reson Imaging* 2018;47:11-27. doi:10.1002/jmri.25838

78. Haris M, Singh A, Cai K, Kogan F, McGarvey J, Debrosse C, et al. A technique for in vivo mapping of myocardial creatine kinase metabolism. *Nat Med* 2014;20:209-214. doi:10.1038/nm.3436

79. Zhou Z, Nguyen C, Chen Y, Shaw JL, Deng Z, Xie Y, et al. Optimized CEST cardiovascular magnetic resonance for assessment of metabolic activity in the heart. *J Cardiovasc Magn Reson* 2017;19:95. doi:10.1186/s12968-017-0411-1

80. Pumphrey A, Yang Z, Ye S, Powell DK, Thalman S, Watt DS, et al. Advanced cardiac chemical exchange saturation transfer (cardioCEST) MRI for *in vivo* cell tracking and metabolic imaging. *NMR Biomed* 2016;29:74-83. doi:10.1002/nbm.3451

81. Petz A, Grandoch M, Gorski DJ, Abrams M, Piroth MA, Schneckmann R, et al. Cardiac Hyaluronan Synthesis Is Critically Involved in the Cardiac Macrophage Response and Promotes Healing After Ischemia Reperfusion Injury. *Circ Res* 2019;124:1433-1447. doi:10.1161/CIRCRESAHA.118.313285

82. Bulte JWM, Daldrup-Link HE. Clinical Tracking of Cell Transfer and Cell Transplantation: Trials and Tribulations. *Radiology* 2018;289. doi:10.1148/radiol.2018180449

83. Suzuki Y, Cunningham CH, Noguchi KI, Chen IY, Weissman IL, Yeung AC, et al. In vivo serial evaluation of superparamagnetic iron-oxide labeled stem cells by off-resonance positive contrast. *Magn Reson Med* 2008;60:1269-1275. doi:10.1002/mrm.21816

84. Makela A V., Foster PJ. Imaging macrophage distribution and density in mammary tumors and lung metastases using fluorine-19 MRI cell tracking. *Magn Reson Med* 2018;80:1138-1147. doi:10.1002/mrm.27081

85. Rothe M, Jahn A, Weiss K, Hwang JH, Szendroedi J, Kelm M, et al. In vivo 19 F MR inflammation imaging after myocardial infarction in a large animal model at 3 T. *Magn Reson Mater Physics, Biol Med* 2019;32:5-13. doi:10.1007/s10334-

018-0714-8

86. Bönner F, Merx MW, Klingel K, Begovatz P, Flögel U, Sager M, et al. Monocyte imaging aftermyocardial infarction with ^{19}FMRI at 3 T: A pilot study in explanted porcine hearts. *Eur Heart J Cardiovasc Imaging* 2015;16:612-620. doi:10.1093/ehjci/jev008

87. Dassanayake PSB, Goldhawk DE. Monocyte MRI Relaxation Rates are Regulated by Extracellular Iron and Hepcidin. *MSc Thesis West Univ* 2019.

88. Alizadeh K, Sun Q, McGuire T, Thompson RT, Prato FS, Koropatnick DJ, et al. Hepcidin-mediated Iron Regulation in P19 Cells is Detectable by Magnetic Resonance Imaging. *Mol Imaging Biol, Submitt* 2019.

89. Lewis AJM, Burrage MK, Ferreira VM. Cardiovascular magnetic resonance imaging for inflammatory heart diseases. *Cardiovasc Diagn Ther* 2020;10:598-609. doi:10.21037/cdt.2019.12.09

90. Lewis AJM, Miller JJ, Lau AZ, Curtis MK, Rider OJ, Choudhury RP, et al. Noninvasive immunometabolic cardiac inflammation imaging using hyperpolarized magnetic resonance. *Circ Res* 2018;122:1084-1093. doi:10.1161/CIRCRESAHA.117.312535

91. Yang HJ, Sharif B, Pang J, Kali A, Bi X, Cokic I, et al. Free-breathing, motion-corrected, highly efficient whole heart T2 mapping at 3T with hybrid radial-cartesian trajectory. *Magn Reson Med* 2016;75:126-136. doi:10.1002/mrm.25576

92. Goldhawk DE, Rohani R, Sengupta A, Gelman N, Prato FS. Using the magnetosome to model effective gene-based contrast for magnetic resonance imaging. *Wiley Interdiscip Rev Nanomedicine Nanobiotechnology* 2012;4:378-388. doi:10.1002/wnan.1165

93. Goldhawk DE, Gelman N, Thompson RT, Prato FS. Forming magnetosome-like nanoparticles in mammalian cells for molecular MRI. In: *Design and Applications of Nanoparticles in Biomedical Imaging*. ; 2017:187-203.

94. Ylä-Herttuala S, Baker AH. Cardiovascular Gene Therapy: Past, Present, and Future. *Mol Ther* 2017;25:1095-1106. doi:10.1016/j.ymthe.2017.03.027

95. Wollenweber T, Bengel FM. Cardiac molecular imaging. *Semin Nucl Med* 2014;44:386-397. doi:10.1053/j.semnuclmed.2014.05.002

96. Zanotti-Fregonora P, Pascual B, Rostomily R, Rizzo G, Veronese M, Masdeu J, et al. Anatomy of 18F-GE180, a failed radioligand for the TSPO protein. *Eur J Nucl Med Mol Imaging* 2020;47:2233-2236. doi:10.1007/s00259-020-04885-w

97. Wilson AA, Garcia A, Parkes J, McCormick P, Stephenson KA, Houle S, et al. Radiosynthesis and initial evaluation of [18F]-FEPPA for PET imaging of peripheral benzodiazepine receptors. *Nucl Med Biol* 2008;35:305-314. doi:10.1016/j.nucmedbio.2007.12.009

98. Zammit M, Tao Y, Olsen ME, Metzger J, Vermilyea SC, Bjornson K, et al. [18F]FEPPA PET imaging for monitoring CD68-positive microglia/macrophage neuroinflammation in nonhuman primates. *EJNMMI Res* 2020;10. doi:10.1186/s13550-020-00683-5

99. Haschemi A, Kosma P, Gille L, Evans CR, Burant CF, Starkl P, et al. The sedoheptulose kinase CARKL directs macrophage polarization through control of glucose metabolism. *Cell Metab* 2012;15:813-826. doi:10.1016/j.cmet.2012.04.023

100. Larson SR, Pieper JA, Hulten EA, Ficaro EP, Corbett JR, Murthy VL, et al. Characterization of a highly effective preparation for suppression of myocardial glucose utilization. *J Nucl Cardiol* 2019. doi:10.1007/s12350-019-01786-w

101. Thackeray J, Ross TL, Bankstahl J, Wester H, Bengel F. Targeting cardiovascular inflammation for imaging: Comparison of the uptake of multiple tracers in leukocyte subpopulations. *J Nucl Med* 2017.

102. Wisenberg G, Thiessen JD, Pavlovsky W, Butler J, Wilk B, Prato FS. Same day comparison of PET/CT and PET/MR in patients with cardiac sarcoidosis. *J Nucl*

Cardiol 2019. doi:10.1007/s12350-018-01578-8

103. Murthy VL, Bateman TM, Beanlands RS, Berman DS, Borges-Neto S, Chareonthaitawee P, et al. Clinical Quantification of Myocardial Blood Flow Using PET: Joint Position Paper of the SNMMI Cardiovascular Council and the ASNC. *J Nucl Med* 2018;59:273-293. doi:10.2967/jnumed.117.201368

104. Rust TC, DiBella EVR, McGann CJ, Christian PE, Hoffman JM, Kadrmas DJ. Rapid dual-injection single-scan 13N-ammonia PET for quantification of rest and stress myocardial blood flows. *Phys Med Biol* 2006;51:5347-5362. doi:10.1088/0031-9155/51/20/018

105. Kadrmas DJ, Rust TC, Lazewatsky J, Slomka PJ, Bierman D, Di Carli MF, et al. Single-scan rest-stress cardiac PET imaging with Flurpiridaz F18. *J Nucl Med* 2012;53:140.

106. Ory D, Celen S, Verbruggen A, Bormans G. PET Radioligands for In Vivo Visualization of Neuroinflammation. *Curr Pharm Des* 2014;20:5897-5913. doi:10.2174/1381612820666140613120212

107. Pannell M, Economopoulos V, Wilson TC, Kersemans V, Isenegger PG, Larkin JR, et al. Imaging of translocator protein upregulation is selective for pro-inflammatory polarized astrocytes and microglia. *Glia* 2020;68:280-297. doi:10.1002/glia.23716

108. Vivash L, OBrien TJ. Imaging Microglial Activation with TSPO PET: Lighting Up Neurologic Diseases? *J Nucl Med* 2015;57:165-168. doi:10.2967/jnumed.114.141713

109. Thackeray JT, Hupe HC, Wang Y, Bankstahl JP, Berding G, Ross TL, et al. Myocardial Inflammation Predicts Remodeling and Neuroinflammation After Myocardial Infarction. *J Am Coll Cardiol* 2018;71:263-275. doi:10.1016/j.jacc.2017.11.024

110. Thackeray JT, Derlin T, Haghikia A, Napp LC, Wang Y, Ross TL, et al. Molecular

Imaging of the Chemokine Receptor CXCR4 after Acute Myocardial Infarction. *JACC Cardiovasc Imaging* 2015;8:1417-1426. doi:10.1016/j.jcmg.2015.09.008

111. Derlin T, Sedding DG, Dutzmann J, Haghikia A, König T, Napp LC, et al. Imaging of chemokine receptor CXCR4 expression in culprit and nonculprit coronary atherosclerotic plaque using motion-corrected [68Ga]pentixafor PET/CT. *Eur J Nucl Med Mol Imaging* 2018;45:1934-1944. doi:10.1007/s00259-018-4076-2

112. Pedersen SF, Sandholt BV, Keller SH, Hansen AE, Clemmensen AE, Sillesen H, et al. 64Cu-DOTATATE PET/MRI for detection of activated macrophages in carotid atherosclerotic plaques: Studies in patients undergoing endarterectomy. *Arterioscler Thromb Vasc Biol* 2015;35:1696-1703. doi:10.1161/ATVBAHA.114.305067

113. Tarkin JM, Joshi FR, Evans NR, Chowdhury MM, Figg NL, Shah A V., et al. Detection of Atherosclerotic Inflammation by 68Ga-DOTATATE PET Compared to [18F]FDG PET Imaging. *J Am Coll Cardiol* 2017;69:1774-1791. doi:10.1016/j.jacc.2017.01.060

114. Höglund J, Shirvan A, Antoni G, Gustavsson SÅ, Långström B, Ringheim A, et al. 18F-ML-10, a PET tracer for apoptosis: First human study. *J Nucl Med* 2011;52:720-725. doi:10.2967/jnumed.110.081786

115. Toczek J, Ye Y, Gona K, Kim HY, Han J, Razavian M, et al. Preclinical evaluation of RYM1, a matrix metalloproteinase-targeted tracer for imaging aneurysm. *J Nucl Med* 2017;58:1318-1323. doi:10.2967/jnumed.116.188656

116. Tahara N, Mukherjee J, De Haas HJ, Petrov AD, Tawakol A, Haider N, et al. 2-deoxy-2-[18F]fluoro-d-mannose positron emission tomography imaging in atherosclerosis. *Nat Med* 2014;20:215-219. doi:10.1038/nm.3437

117. Van De Wiele C, Sathekge M, Maes A. Targeting monocytes and macrophages by means of SPECT and PET. *Q J Nucl Med Mol Imaging* 2014;58:269-275.

118. Bansal A, Pandey MK, Demirhan YE, Nesbitt JJ, Crespo-Diaz RJ, Terzic A, et al. Novel 89Zr cell labeling approach for PET-based cell trafficking studies. *EJNMMI Res* 2015;5. doi:10.1186/s13550-015-0098-y

119. Prato FS, Butler J, Sykes J, Keenliside L, Blackwood KJ, Thompson RT, et al. Can the Inflammatory Response Be Evaluated Using 18F-FDG Within Zones of Microvascular Obstruction After Myocardial Infarction? *J Nucl Med* 2015;56:299-304. doi:10.2967/jnumed.114.147835

120. Blackwood KJ, Lewden B, Wells RG, Sykes J, Stodilka RZ, Wisenberg G, et al. In Vivo SPECT Quantification of Transplanted Cell Survival After Engraftment Using 111In-Tropolone in Infarcted Canine Myocardium. *J Nucl Med* 2009;50:927-935. doi:10.2967/jnumed.108.058966

121. Amsalem Y, Mardor Y, Feinberg MS, Landa N, Miller L, Daniels D, et al. Iron-oxide labeling and outcome of transplanted mesenchymal stem cells in the infarcted myocardium. *Circulation* 2007;116:38-45. doi:10.1161/CIRCULATIONAHA.106.680231

122. Yao Y, Li Y, Ma G, Liu N, Ju S, Jin J, et al. In vivo magnetic resonance imaging of injected endothelial progenitor cells after myocardial infarction in rats. *Mol Imaging Biol* 2011;13:303-313. doi:10.1007/s11307-010-0359-0

123. Parashurama N, Ahn BC, Ziv K, Ito K, Paulmurugan R, Willmann JK, et al. Multimodality molecular imaging of cardiac cell transplantation: Part I. Reporter gene design, characterization, and optical in vivo imaging of bone marrow stromal cells after myocardial infarction. *Radiology* 2016;280:815-825. doi:10.1148/radiol.2016140049

124. Miyagawa M, Anton M, Haubner R, Simoes M V, Städele C, Erhardt W, et al. PET of cardiac transgene expression: comparison of 2 approaches based on herpesviral thymidine kinase reporter gene. *J Nucl Med* 2004;45:1917-1923.

125. Rausch I, Quick HH, Cal-Gonzalez J, Sattler B, Boellaard R, Beyer T. Technical

and instrumentational foundations of PET/MRI. *Eur J Radiol* 2017;94:A3-A13. doi:10.1016/j.ejrad.2017.04.004

126. Lassen ML, Rasul S, Beitzke D, Stelzmüller ME, Cal-Gonzalez J, Hacker M, et al. Assessment of attenuation correction for myocardial PET imaging using combined PET/MRI. *J Nucl Cardiol* 2019;26:1107-1118. doi:10.1007/s12350-017-1118-2

127. Robson PM, Vergani V, Benkert T, Trivieri MG, Karakatsanis NA, Abgral R, et al. Assessing the qualitative and quantitative impacts of simple two-class vs multiple tissue-class MR-based attenuation correction for cardiac PET/MR. *J Nucl Cardiol* 2020. doi:10.1007/s12350-019-02002-5

128. Fürst S, Souvatzoglou M, Rischpler C, Ziegler S, Schwaiger M, Nekolla S. Effects of MR contrast agents on attenuation map generation and cardiac PET quantification in PET/MR. *J Nucl Med* 2012;53:139.

129. Farag A, Thompson RT, Thiessen JD, Butler J, Prato FS, Théberge J. Assessment of a Novel 32-Channel Phased Array for Cardiovascular Hybrid PET/MRI Imaging: MRI performance. *Eur J Hybrid Imaging* 2019;3.

130. Vontobel J, Liga R, Possner M, Clerc OF, Mikulicic F, Veit-Haibach P, et al. MR-based attenuation correction for cardiac FDG PET on a hybrid PET/MRI scanner: comparison with standard CT attenuation correction. *Eur J Nucl Med Mol Imaging* 2015;42:1574-1580. doi:10.1007/s00259-015-3089-3

131. Lau JMC, Laforest R, Sotoudeh H, Nie X, Sharma S, McConathy J, et al. Evaluation of attenuation correction in cardiac PET using PET/MR. *J Nucl Cardiol* 2017;24:839-846. doi:10.1007/s12350-015-0197-1

132. Goldhawk DE, Gelman N, Thompson RT, Prato FS. Forming magnetosome-like nanoparticles in mammalian cells for molecular MRI. In: *Design and Applications of Nanoparticles in Biomedical Imaging*. ; 2016.

133. Cherry SR, Sorenson JA, Phelps ME. *Physics in Nuclear Medecine*.; 2003.

134. Chen BC, Legant WR, Wang K, Shao L, Milkie DE, Davidson MW, et al. Lattice light-sheet microscopy: Imaging molecules to embryos at high spatiotemporal resolution. *Science (80-)* 2014;346. doi:10.1126/science.1257998

135. Ephrat P, Albert GC, Roumeliotis MB, Belton M, Prato FS, Carson JJL. Localization of spherical lesions in tumor-mimicking phantoms by 3D sparse array photoacoustic imaging. *Med Phys* 2010;37:1619-1628. doi:10.1118/1.3352785

136. James ML, Gambhir SS. A Molecular Imaging Primer: Modalities, Imaging Agents, and Applications. *Physiol Rev* 2012;92:897-965. doi:10.1152/physrev.00049.2010

137. Gore JC, Yankeelov TE, Peterson TE, Avison MJ. Molecular Imaging Without Radiopharmaceuticals? *J Nucl Med* 2009;50:999-1007. doi:10.2967/jnumed.108.059576

138. Moses WW. Fundamental limits of spatial resolution in PET. *Nucl Instruments Methods Phys Res Sect A Accel Spectrometers, Detect Assoc Equip* 2011;648:S236-40. doi:10.1016/j.nima.2010.11.092

139. Meikle SR, Kench P, Kassiou M, Banati RB. Small animal SPECT and its place in the matrix of molecular imaging technologies. *Phys Med Biol* 2005;50:R45-61. doi:10.1088/0031-9155/50/22/R01

140. Lewis CE, Prato FS, Drost DJ, Nicholson RL. Comparison of respiratory triggering and gating techniques for the removal of respiratory artifacts in MR imaging. *Radiology* 1986;160:803-810. doi:10.1148/radiology.160.3.3737921

141. Pang J, Bhat H, Sharif B, Fan Z, Thomson LEJ, Labounty T, et al. Whole-heart coronary MRA with 100% respiratory gating efficiency: Self-navigated three-dimensional retrospective image-based motion correction (TRIM). *Magn Reson Med* 2014;71:67-74. doi:10.1002/mrm.24628

142. Kolbitsch C, Ahlman MA, Davies-Venn C, Evers R, Hansen M, Peressutti D, et al. Cardiac and Respiratory Motion Correction for Simultaneous Cardiac PET/MR. *J*

Nucl Med 2017;58:846-852. doi:10.2967/jnumed.115.171728

143. Munoz C, Neji R, Kunze KP, Nekolla SG, Botnar RM, Prieto C. Respiratory- and cardiac motion-corrected simultaneous whole-heart PET and dual phase coronary MR angiography. *Magn Reson Med* 2019;81:1671-1684. doi:10.1002/mrm.27517

144. Feng T, Wang J, Tsui BMW. Dual respiratory and cardiac motion estimation in PET imaging: Methods design and quantitative evaluation. *Med Phys* 2018;45:1481-1490. doi:10.1002/mp.12793

145. Robson PM, Trivieri MG, Karakatsanis NA, Padilla M, Abgral R, Dweck MR, et al. Correction of respiratory and cardiac motion in cardiac PET/MR using MR-based motion modeling. *Phys Med Biol* 2018;63:225011. doi:10.1088/1361-6560/aaea97

146. Petibon Y, Sun T, Han PK, Ma C, El Fakhri G, Ouyang J. MR-based cardiac and respiratory motion correction of PET: application to static and dynamic cardiac 18F-FDG imaging. *Phys Med Biol* 2019;64:195009. doi:10.1088/1361-6560/ab39c2

147. Klyuzhin IS, Sossi V. PET Image Reconstruction and Deformable Motion Correction Using Unorganized Point Clouds. *IEEE Trans Med Imaging* 2017;36:1263-1275. doi:10.1109/TMI.2017.2675989

148. Thiessen JD, Sykes J, Keenliside L, Biernaski H, Butler J, Cockburn N, et al. Feasibility of multi-week PET studies with a single injection of 89Zr-phosphate on a clinical PET/MRI. *30th Annu Meet Eur Assoc Nucl Med* 2017.

149. Hahn A, Gryglewski G, Nics L, Hienert M, Rischka L, Vraka C, et al. Quantification of task-specific glucose metabolism with constant infusion of 18F-FDG. *J Nucl Med* 2016;57:1933-1940. doi:10.2967/jnumed.116.176156

150. Villien M, Wey HY, Mandeville JB, Catana C, Polimeni JR, Sander CY, et al. Dynamic functional imaging of brain glucose utilization using fPET-FDG. *Neuroimage* 2014;100:192-199. doi:10.1016/j.neuroimage.2014.06.025

151. Barton GP, Vildberg L, Goss K, Aggarwal N, Eldridge M, McMillan AB. Simultaneous determination of dynamic cardiac metabolism and function using PET/MRI. *J Nucl Cardiol* 2018. doi:10.1007/s12350-018-1287-7

152. Wilk B, Wisenberg G, Sykes J, Butler J, Kovacs MS, Thompson RT, et al. Quantifying inflammation in infarcted myocardial tissue with severely reduced flow: a hybrid PET/MRI approach using a prolonged constant infusion of 18F-FDG and Gd-DTPA. *Soc Nucl Med Mol Imaging 2018 Annu Meet* 2018.

153. Kunze KP, Nekolla SG, Rischpler C, Zhang SHL, Hayes C, Langwieser N, et al. Myocardial perfusion quantification using simultaneously acquired 13NH3-ammonia PET and dynamic contrast-enhanced MRI in patients at rest and stress. *Magn Reson Med* 2018. doi:10.1002/mrm.27213

154. Feng L, Grimm R, Block KT obia., Chandarana H, Kim S, Xu J, et al. Golden-angle radial sparse parallel MRI: combination of compressed sensing, parallel imaging, and golden-angle radial sampling for fast and flexible dynamic volumetric MRI. *Magn Reson Med* 2014;72:707-717. doi:10.1002/mrm.24980

155. Piekarski E, Chitiboi T, Ramb R, Feng L, Axel L. Use of self-gated radial cardiovascular magnetic resonance to detect and classify arrhythmias (atrial fibrillation and premature ventricular contraction). *J Cardiovasc Magn Reson* 2016;18:83. doi:10.1186/s12968-016-0306-6

156. Piekarski E, Chitiboi T, Ramb R, Latson LA, Bhatla P, Feng L, et al. Two-dimensional XD-GRASP provides better image quality than conventional 2D cardiac cine MRI for patients who cannot suspend respiration. *Magn Reson Mater Physics, Biol Med* 2018;31:49-59. doi:10.1007/s10334-017-0655-7

157. Piccini D, Feng L, Bonanno G, Coppo S, Yerly J, Lim RP, et al. Four-dimensional respiratory motion-resolved whole heart coronary MR angiography. *Magn Reson Med* 2017;77:1473-1484. doi:10.1002/mrm.26221

158. Heydari B, Kwong RY, Jerosch-Herold M. Technical Advances and Clinical

Applications of Quantitative Myocardial Blood Flow Imaging With Cardiac MRI. *Prog Cardiovasc Dis* 2015;57:615-622. doi:10.1016/j.pcad.2015.02.003

159. Yang H-J, Christodoulou AG, Sykes J, Bi X, Cokic I, Prato FS, et al. Beat-by-beat dynamic assessment of myocardial oxygenation with highly time-resolved free-breathing, ungated cardiac T2 BOLD MRI using a low-rank tensor formulation. *Int Soc Magn Reson Med 2018 Annu Meet* 2018.

160. Davidson CQ, Phenix CP, Tai T, Khaper N, Lees SJ. Searching for novel PET radiotracers: imaging cardiac perfusion, metabolism and inflammation. *Am J Nucl Med Mol Imaging* 2018;8:200-227. www.ajnmmi.us.

161. Tofts PS. Modeling tracer kinetics in dynamic Gd-DTPA MR imaging. *J Magn Reson Imaging* 1997;7:91-101. doi:10.1002/jmri.1880070113

162. Richard MA, Fouquet JP, Lebel R, Lepage M. MRI-Guided Derivation of the Input Function for PET Kinetic Modeling. *PET Clin* 2016;11:193-202. doi:10.1016/j.cpet.2015.09.003

163. Qi Q, Fox MS, Bartha R, Hoffman L, Lee TY, Thiessen JD. Comparison of Glucose-CEST with Perfusion and Glycolysis Measurements in a C6 Rat Model of Glioma. *World Mol Imaging Congr 2018* 2018.

164. Yang H-J, Ilkary O, Dey D, Sykes J, Klein M, Butler J, et al. Accurate Needle-Free Assessment of Myocardial Oxygenation for Ischemic Heart Disease. *Sci Transl Med (Provisionally Accept* 2019.

165. Dey D, Slomka PJ, Leeson P, Comaniciu D, Shrestha S, Sengupta PP, et al. Artificial Intelligence in Cardiovascular Imaging. *J Am Coll Cardiol* 2019;73:1317-1335. doi:10.1016/j.jacc.2018.12.054

166. Tan LK, McLaughlin RA, Lim E, Abdul Aziz YF, Liew YM. Fully automated segmentation of the left ventricle in cine cardiac MRI using neural network regression. *J Magn Reson Imaging* 2018;48:140-152. doi:10.1002/jmri.25932

167. Couzin-Frankel J. When mice mislead. *Science* 2013;342:922-923. doi:10.1126/science.342.6161.922

168. Grimm D. From bark to bedside. *Science (80-)* 2016;353:638-640. doi:10.1126/science.353.6300.638

169. Thompson K, Wisenberg G, Sykes J, Terry Thompson R. MRI/MRS evaluation of cariporide in a canine long-term model of reperfused ischemic insults. *J Magn Reson Imaging* 2003;17:136-141. doi:10.1002/jmri.10222

170. Diesbourg LD, Prato FS, Wisenberg G, Drost DJ, Marshall TP, Carroll SE, et al. Quantification of myocardial blood flow and extracellular volumes using a bolus injection of Gd-DTPA: Kinetic modeling in canine ischemic disease. *Magn Reson Med* 1992;23:239-253. doi:10.1002/mrm.1910230205

171. Thornhill RE, Prato FS, Wisenberg G. The assessment of myocardial viability: A review of current diagnostic imaging approaches. *J Cardiovasc Magn Reson* 2002;4:381-410. doi:10.1081/jcmr-120013301

172. Weinsaft JW, Klem I, Judd RM. MRI for the Assessment of Myocardial Viability. *Magn Reson Imaging Clin N Am* 2007;25:35-36. doi:10.1016/j.mric.2007.08.007

173. Saeed M, Lund G, Wendland MF, Bremerich J, Weinmann HJ, Higgins CB. Magnetic resonance characterization of the peri-infarction zone of reperfused myocardial infarction with necrosis-specific and extracellular nonspecific contrast media. *Circulation* 2001;103:871-876. doi:10.1161/01.CIR.103.6.871

174. Frangogiannis NG, Mendoza LH, Ren G, Akrivakis S, Jackson PL, Michael LH, et al. MCSF expression is induced in healing myocardial infarcts and may regulate monocyte and endothelial cell phenotype. *Am J Physiol Circ Physiol* 2003;285:H483-92. doi:10.1152/ajpheart.01016.2002

175. Frantz S, Nahrendorf M. Cardiac macrophages and their role in ischaemic heart disease. *Cardiovasc Res* 2014;102:240-248. doi:10.1093/cvr/cvu025

176. Lee WW, Marinelli B, Van Der Laan AM, Sena BF, Gorbatov R, Leuschner F, et al. PET/MRI of inflammation in myocardial infarction. *J Am Coll Cardiol* 2012;59:153-163. doi:10.1016/j.jacc.2011.08.066

177. Hamirani YS, Wong A, Kramer CM, Salerno M. Effect of microvascular obstruction and intramyocardial hemorrhage by CMR on LV remodeling and outcomes after myocardial infarction: A systematic review and meta-analysis. *JACC Cardiovasc Imaging* 2014;7:940-952. doi:10.1016/j.jcmg.2014.06.012

178. Maxwell MP, Hearse DJ, Yellon DM. Species variation in the coronary collateral circulation during regional myocardial ischaemia: A critical determinant of the rate of evolution and extent of myocardial infarction. *Cardiovasc Res* 1987;21:737-746. doi:10.1093/cvr/21.10.737

179. Phelps ME, Huang SC, Hoffman EJ, Selin C, Sokoloff L, Kuhl DE. Tomographic measurement of local cerebral glucose metabolic rate in humans with (F-18)2-fluoro-2-deoxy-D-glucose: Validation of method. *Ann Neurol* 1979;6:371-388. doi:10.1002/ana.410060502

180. Dweck MR, Abgral R, Trivieri MG, Robson PM, Karakatsanis N, Mani V, et al. Hybrid Magnetic Resonance Imaging and Positron Emission Tomography With Fluorodeoxyglucose to Diagnose Active Cardiac Sarcoidosis. *JACC Cardiovasc Imaging* 2018;11:94-107. doi:10.1016/j.jcmg.2017.02.021

181. Smailovic H, Wilk B, Wisenberg G, Sykes J, Butler J, Hicks JW, et al. Simultaneous measurements of myocardial glucose metabolism and extracellular volumes with hybrid PET/MRI using concurrent injections of Gd-DTPA and [18F]FDG. *Submitt to J Nucl Cardiol* 2020.

182. Wilk B, Smailovic H, Wisenberg G, Sykes J, Butler J, Kovacs M, et al. Tracking the progress of inflammation with PET/MRI in a canine model of myocardial infarction. *J Nucl Cardiol* 2021. doi:10.1007/s12350-020-02487-5

Chapter 2

2 Simultaneous measurements of myocardial glucose metabolism and extracellular volumes with hybrid PET/MRI using concurrent injections of Gd-DTPA and [18F]FDG

2.1 Introduction

Pathological alterations in myocardial tissue composition can be assessed using cardiovascular magnetic resonance imaging[1]. Absolute T1 relaxation times throughout the myocardium can be quantified using T1 mapping before and after administration of a gadolinium-based contrast agent (GBCA)[2]. Pre- and post-contrast T1 maps can be combined to give a direct measure of the extracellular volume (ECV)[2,3]. Myocardial fibrosis, a crucial component of the pathologic remodeling leading to heart failure, is characterized by myocardial extracellular matrix expansion and accumulation of interstitial collagen[4]. GBCA track extracellular collagen, which is the principal constituent of the expanded extracellular matrix and ECV mapping has shown promising results with respect to characterizing the extent of infiltrative and fibrotic cardiac diseases, such as sarcoidosis[3–5].

In order to quantify ECV accurately in the heart, single-slice breath hold T1 maps must be acquired spanning the entire heart[3,6,7]. For full heart coverage and artifact elimination, this requires acquisition during which the concentration of GBCA in the blood and tissue should not be changing significantly[3,6,7]. A bolus injection followed by a constant infusion of GBCA, given the correct timing and dose distribution between the bolus and constant infusion, achieves relatively rapid, constant blood concentrations which can be sustained for up to one hour[3,6–8]. Clinically, however, ECV is normally measured after a bolus injection of a GBCA (without an infusion)[9], but the results may be affected by the constantly changing blood and perhaps resultant tissue contrast levels. However, there are

no studies that have investigated the effects on tracer concentrations and image data using only a prolonged constant infusion without a preceding bolus. An accurate and reproducible measurement of the distribution volume (V_D) of GBCA, could lead to a more in-depth understanding of the pathology of both healthy and injured myocardial tissue.

PET can provide additional complementary information to MRI particularly when PET and MRI are combined as a hybrid platform[10,11]. [^{18}F]FDG PET/MRI is increasingly used for the detection of cellularly-mediated cardiac inflammation, particularly in sarcoidosis and, more recently, in myocardial infarction[11,12]. Using hybrid PET/MR with concurrent [^{18}F]FDG and GBCA injections would reduce overall imaging time and can facilitate optimal registration of the PET and MRI images[10,11]. However, assessment of myocardial inflammation also requires suppression of myocyte uptake of [^{18}F]FDG to be able to differentiate between physiological and pathological uptake of FDG by inflammatory macrophages[11]. Clinically, suppression of glucose is accomplished using intravenous heparin and a high fat diet[11]. Heparin is a glycosaminoglycan and therefore exerts a strong osmotic pressure on cells[13]. Joerges et al. has shown that extracellular heparin significantly increased the cell volume of fibroblasts *in vitro*[13], potentially altering the intra/extracellular volume relationship. However, the effects of heparin on ECV *in vivo* remain unclear.

This study was performed to determine if the issues identified above associated with differing infusion protocols and concurrent injections of GBCA and [^{18}F]FDG while performing myocardial glucose suppression affect the determination of myocardial ECVs and glucose uptake. These were investigated in the setting of three different injection protocols: bolus, constant infusion only and a bolus followed by constant infusion. Further, to determine the chemical stability of the compounds when combining Gd-DTPA and FDG, we used radiochromatography on a mixture of FDG and GBCA, once with a linear gadolinium chelator (Gd-DTPA, Magnevist, Bayer) and once with a cyclic chelator (gadobutrol, Gadovist, Bayer).

2.2 Materials and Methods

2.2.1 Animal Preparation

The care and treatment of the animals was in accordance with the University of Western Ontario Council on Animal Care (Animal Use Subcommittee) guidelines. Five healthy female canine subjects were imaged to compare the three different protocols for injecting Gd-DTPA: the standard bolus injection approach, delivery by a constant infusion over 60 minutes without a bolus, or use of a bolus followed by a 30 minute constant infusion. The adult, female, bred-for-research hounds weighed 18-23 kg. Anesthesia for all procedures was induced using propofol and maintained with 1.5% - 2% isoflurane (Forane, Baxter). When required by the imaging protocol, the suppression of myocardial glucose uptake was induced using a continuous infusion of 20% lipid (Intralipid; Baxter Healthcare Corporation) at a rate of 0.25mL/min/kg over a 50-minute period as well as 2000 units of intravenous heparin injected 20 minutes prior to FDG/Gd-DTPA injection[11]. This we have shown is the most effective approach in canines.[12] The requirement of the intralipid infusion may be related to the difference between the diet of dogs compared to humans. Note also that the effective use of heparin in humans is listed by weight[14] whereas in dogs we simply used a fixed dose as the weight of all animals was similar i.e. 18-23 kg.

2.2.2 PET/MRI Protocol

All canine subjects were imaged with a Siemens Biograph mMR 3T clinical scanner. The animals were placed in a right lateral recumbent position and 3 electrodes were positioned on the chest. Gd-DTPA and [^{18}F]FDG were injected through an intravenous line. The same five canine subjects were scanned on two different occasions for each of the three different injection protocols shown below (also on different days), once with the extensive protocol for suppression of glucose uptake by the myocardium and then again without this suppression protocol i.e. six different scanning sessions per canine (See figure 2-1 for sample images from 1 animal). Due to two unsuccessful experiments in the

bolus only work (figure 2-4b), two animals had only one bolus scan done, one of the suppressed, the other unsuppressed.

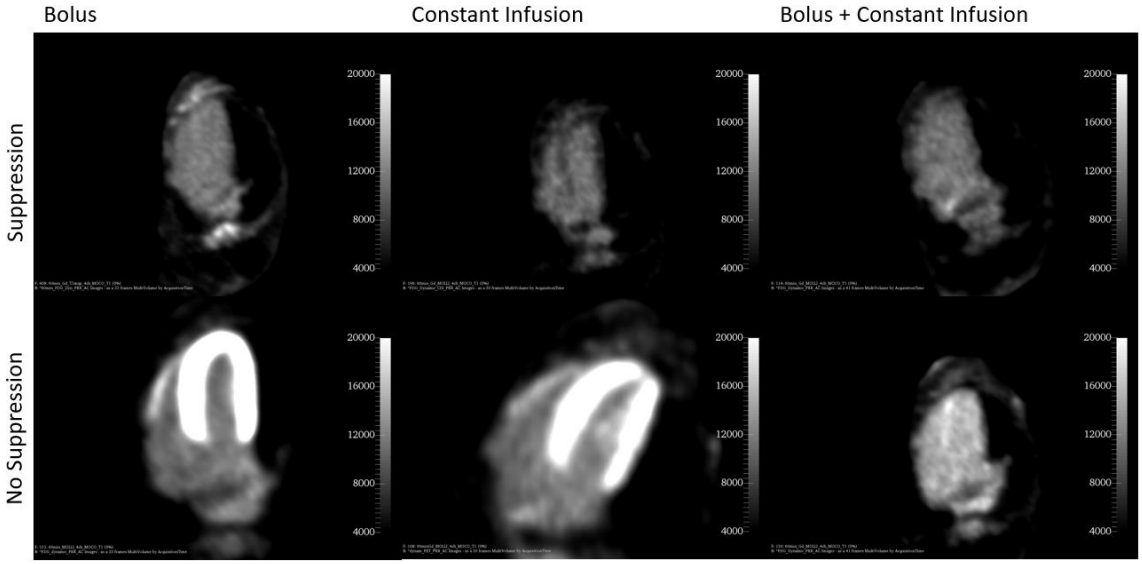

Figure 2-1: Suppression differences based on injection type with FDG imaging.

This figure shows the suppressed vs unsuppressed FDG images in a single animal (D1) with the same image intensity leveling. In this animal, clearly suppression was effective in bolus and constant infusion. As all animals are fasted prior to the scan, as necessitated by the anesthesia, it is likely that this alone may be enough to suppress myocardial glucose uptake in some cases as shown in this animal for the bolus + constant infusion case.

As shown in figure 2-2, each canine was injected a total of 0.24mmol/kg of Gd-DTPA (Magnevist, Bayer Inc.) and 10.2 MBq/kg of FDG (produced in-house at the SJHC Cyclotron facility) for each of the three injection protocols. For the constant infusion only protocol, a 60-minute constant infusion (0.004mmol/kg/min of Gd-DTPA and 0.17 MBq/min/kg FDG) was administered followed by 30 minutes of washout. During the bolus followed by a constant infusion, a bolus of 0.12mmol/kg Gd-DTPA and 5.1 MBq/kg FDG followed by a 30-minute constant infusion (0.004 mmol/kg/min Gd-DTPA and 0.17 MBq/kg) was administered followed by an additional 30 minutes of washout.

Cardiac T1 maps (4-chamber view of the heart) were acquired with a modified Look-Locker inversion recovery (MOLLI) sequence (ECG-gated, 35° flip angle, 256 x 218 matrix size, 300 mm x 255.5 mm field-of-view, 6 mm slice thickness, 400ms repetition time, 1.12ms echo time) during breath hold at pre-contrast and then every 3 min after the concurrent injections: for a total of 60 min after the bolus and bolus plus constant infusion protocols and for 90 minutes following 60 min constant infusion protocol. Note that this included 30 min of washout after the end of the constant infusions.

The PET data was reconstructed in 3-minute frames using a 3D Ordered Subset Expectation Maximization (OSEM) reconstruction (3 iterations, 21 subsets, 172 x 172 x 127 matrix size, zoom of 2 and 4 mm Gaussian filter). Attenuation correction was achieved using a two-point Dixon MRI sequence and segmented into water, fat, lung and air with constant attenuation coefficients for each tissue. The PET voxel size was 2.09 x 2.09 x 2.03 mm. All PET data was acquired in list-mode for 60 minutes in the bolus-only protocol and bolus followed by CI and 90 minutes for the constant infusion only protocol.

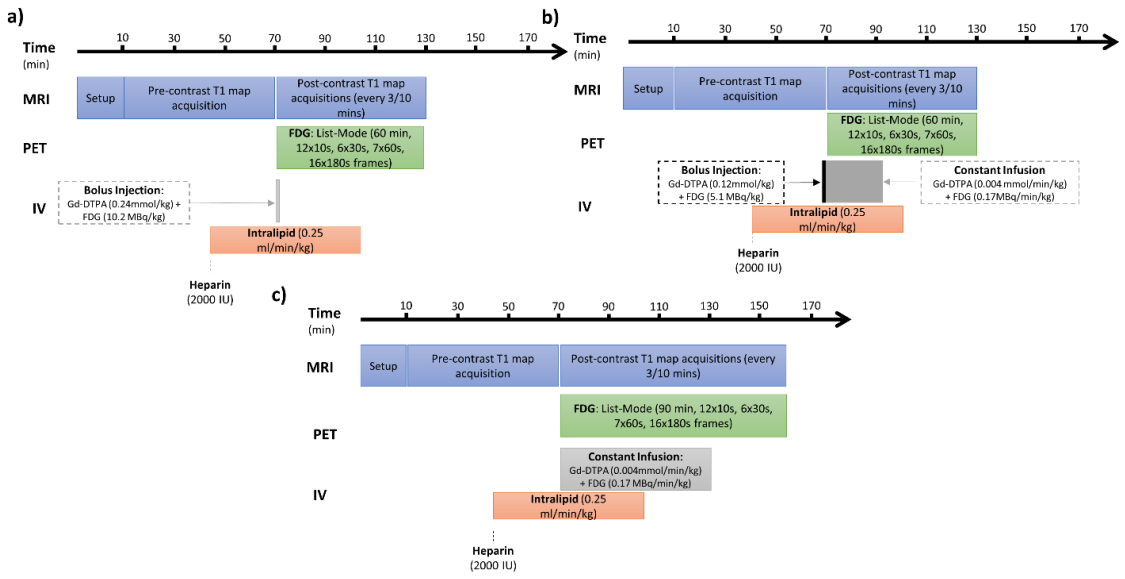

Figure 2-2: Injection protocol with three different injection strategies.

Three different injection strategies of [^{18}F]FDG/Gd-DTPA were used: a) a bolus injection only, b) a bolus followed by a 30-minute constant infusion (Bl + Cl), and c) a

60-minute constant infusion. In the imaging procedure in which glucose metabolism was suppressed a continuous infusion of intralipid and an intravenous heparin injection were administered 20 minutes prior to [^{18}F]FDG/Gd-DTPA injection and MOLLI acquisition.

2.2.3 Image Analysis

Image analysis was performed using 3D Slicer (Open Source, BSD License) and MATLAB (Mathworks, R2019a). As shown in figure 2-3, manually drawn regions of interest (ROIs) in the 4-chamber view were used to identify the healthy myocardium and the left ventricular blood pool. Myocardial and blood T1 values pre- and post- Gd-DTPA administration were measured. Once the ROIs were defined, they were used as a template and copied to the rest of the images in the series. Manual adjustment of some images in the series was applied to offset changes in heart position. Edges were also avoided when drawing ROIs to minimize partial volume averaging from voxels at the myocardial-blood pool border. ECV was calculated using the following formula where hematocrit was assumed to be 0.45[15]. For the comparison of ECV using different injection types with and without glucose suppression, steady-state equilibrium was assumed to be reached when the difference in the calculated ECV between acquisitions was less than 5%, as done by White et al[16] with the following equation:

$$ECV = (1 - hematocrit) \times \frac{\frac{1}{post\ contrast\ T1\ myo} - \frac{1}{native\ T1\ myo}}{\frac{1}{post\ contrast\ T1\ blood} - \frac{1}{native\ T1\ blood}}. \quad \text{Eq 1}$$

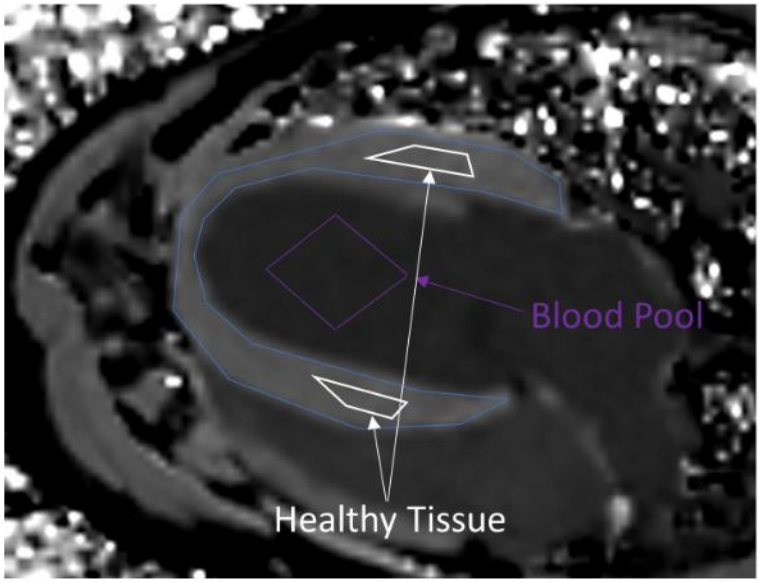

Figure 2-3: Region of interest selection at baseline.

Extracellular volume (ECV) measurements were calculated for three separate regions: two in the healthy myocardium (white ROI's) and one ROI in the blood pool (purple ROI). The ECV was then averaged from the ROI's from the healthy myocardium, using cardiac T1 maps acquired during breath hold at pre-contrast and then every 3 minutes following initial injection(s) of GBCA.

2.2.4 Glucose Metabolism

Using an in-house MATLAB script, the FDG concentration curves of all ROIs were fit to the Patlak model of graphical analysis[17] using the following equation:

$$[FDG(t)]_i = K_i \int_0^t [FDG(\tau)]_p \, d\tau + \left(v_e^P + v_p^P\right)[FDG(t)]_p, \qquad \text{Eq 2}$$

where $[FDG(t)]_i$ is the concentration of [^{18}F]FDG in tissue *i*, K_i, the influx constant which is proportional to the rate of glucose metabolism in tissue *i*. $[FDG(t)]_p$ is the arterial plasma concentration input function which was the blood pool ROI, taken from

within the left ventricular cavity. v_e^p is the equilibrium space of the extravascular exchangeable region and v_p^P the plasma space.

The influx constant, K_i is determined from the slope of $\frac{[FDG(t)]_i}{[FDG(t)]_p}$ vs $\frac{\int_0^t [FDG(\tau)]_p d\tau}{[FDG(t)]_p}$. This slope will be K_i once it is constant, at t = t*, which was operationally defined to be 12 minutes after the start of the constant infusion at which point equilibrium was achieved. $[FDG(t)]_p$ was determined from the blood concentration $[FDG(t)]_b$ corrected by the glucose plasma:whole blood ratio (P) of 1.375[18] and the haematocrit (Hct) i.e. $[FDG(t)]_p = [FDG(t)]_b (P/(1-Hct))$. The tissue concentration was corrected for the partial volume effect in PET using a recovery coefficient (RC) of 0.7 determined for a 10 mm diameter cylinder on our PET/MRI imaging system (approximately equivalent to the thickness of the left ventricular wall)[19,20] i.e.

$$[FDG(t)]_i = \frac{[FDG(t)]_t}{RC} - \frac{1 - RC}{RC}[FDG(t)]_b. \qquad \text{Eq 3}$$

Using this method, K_i was extracted for all ROIs in all studies.

2.2.5 FDG stability under concurrent injection with GBCAs

To a 10 mL vial of Magnevist (Gd-DTPA) or Gadovist (gadobutrol) was added 300 – 500 MBq of [^{18}F]FDG. The vial was stored upright at ambient temperature (20 – 22 ^{o}C). Samples were extracted at 15, 30, 60, and 90 min following initial mixing. These samples were analyzed for changes to pH (colorimetric paper test) and radiochemical purity and identity (radiometric thin layer chromatography or radioTLC) compared to [^{18}F]FDG prior to mixing with GBCA. Both pH and radioTLC test methods were identical to standard testing methods for release of clinical [^{18}F]FDG. The linear range for the radioTLC was 82 – 2290 kBq with a limit of detection of 1.6 kBq at the time of testing. An impurity with 3.3 MBq/mL concentration could reliably be detected. FDG was visualized on the TLC by coating with 10% H_2SO_4 in methanol and heating to give a brown spot.

2.2.6 Statistical Analysis

Statistical analysis was performed using GraphPad Prism (GraphPad Software, La Jolla, CA). All data is presented as mean ± standard error of the mean (SEM) except for Figure 2-7 where mean +/- SD is used. The effect of different protocols on ECV over time were compared using a two-way repeated-measures analysis of variance (ANOVA) followed by Bonferroni multiple comparisons tests. Paired two-tailed t-tests were performed to compare ECV prior to and following washout for the constant infusion protocol. Comparison of differences in ECV and Ki associated with glucose suppression and injection protocol including during washout of Gd-DTPA was assessed with paired and unpaired two-tailed t tests. A p-value of <0.05 was considered to be statistically significant. Bonferroni's method was done to correct for multiple comparisons when comparing multiple treatments' means.

2.3 Results

2.3.1 FDG stability under concurrent injection with GBCAs

At all timepoints, no changes were observed in pH or radiochemical purity. As shown in Table 1, radiochemical identity is confirmed by comparing the retention factors (distance analyte travels versus solvent front) between authentic FDG standard and [^{18}F]FDG. The percent difference between the two retention factors was within 6.4 ± 1.7% and 6.5 ± 3.1% when mixed with Magnevist (Gd-DTPA) and Gadovist (gadobutrol), respectively. This is well within the release specification of 10% and typical of day-to-day variance during clinical productions.

Table 1: Chemical Stability when combining Gd-DTPA or gadobutrol and FDG

Time after mixing (minutes)	Retention Factor Mixed with Gd-DTPA			Retention Factor Mixed with Gadobutrol		
	FDG	[^{18}F]FDG	% Difference	FDG	[^{18}F]FDG	% Difference
Original	0.41	0.43	3.0	0.41	0.43	3.0

15	0.33	0.32	4.4	0.44	0.40	9.1
30	0.38	0.35	7.9	0.42	0.42	1.1
60	0.36	0.38	4.9	0.43	0.39	8.2
90	0.36	0.33	8.2	0.41	0.38	7.5
Average	0.37	0.36	6.4	0.42	0.40	6.5
StDev	0.03	0.04	1.7	0.01	0.02	3.1

2.3.2 Evaluation of ECV in Healthy Myocardium with and without glucose suppression

As shown in Figure 2-4, there was no significant effect of glucose suppression vs. no glucose suppression on the measured ECV at equilibrium irrespective of which infusion protocol was used (bolus-only: p=0.22; constant infusion-only: p=0.10; bolus followed by constant infusion: p=0.09). However, when comparing ECV with glucose suppression across all animals, irrespective of injection method, ECV is significantly higher with suppression (0.21 ± 0.02 vs 0.18 ± 0.01, corresponding to a 13% increase; p = 0.002).

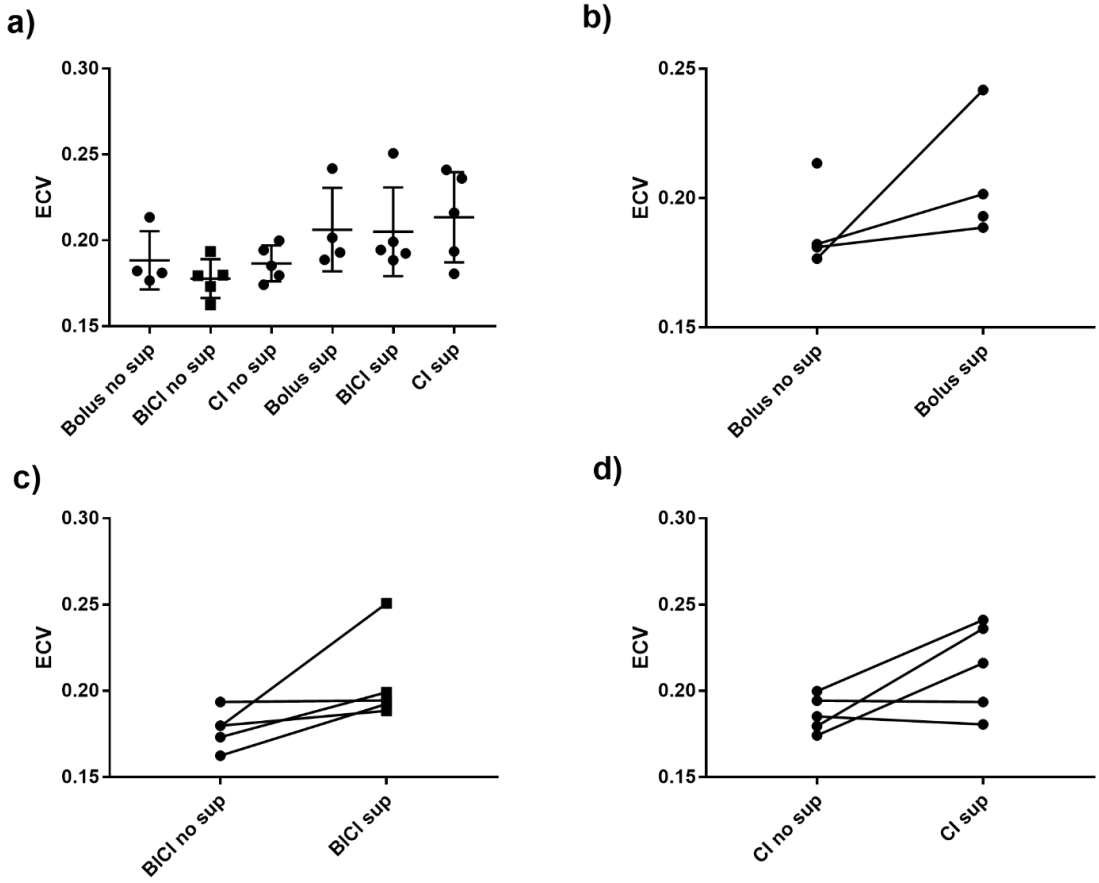

Figure 2-4: The effect of glucose suppression on healthy non-infarcted myocardial ECV.

Suppression was achieved with a continuous infusion of 20% lipid as well as intravenous heparin (2000 units). a) The mean ± SEM ECV for all injection types after equilibrium was reached. No significant differences were found using paired t-tests. The ECV with and without suppression following a b) bolus injection (note that there are only 4 data points given for suppression and no suppression as, due to experimental error, one animal did not have an initial unsuppressed successful experiment and one did not have a successful suppression study), c) Bl + CI injection and d) CI only for each individual canine. The ECV values used corresponded to when equilibrium was reached within the healthy myocardium.

2.3.3 Comparison of ECV in Healthy Myocardium – Measurements using Different Injection Types

When comparing the injection protocols, i.e. a bolus, bolus followed by constant infusion, or a constant infusion, as shown in Figure 2-5, there was no significant difference ($p = 0.21$) between protocols from minute 9 to minute 60. Minute 9 was chosen to exclude times when the tracer is still washing in and therefore may not be representative of the actual ECV. However, over time, the ECV calculated following the bolus injection slowly increased reaching a plateau at minute 18 (0.21 ± 0.02) with a significant difference ($p = 0.02$) between minute 3 vs. minute 18. There was no significant difference found for ECV using the constant infusion protocol at minute 60 when compared to any of the time points beyond that point, i.e. during the 30-minute post infusion washout period.

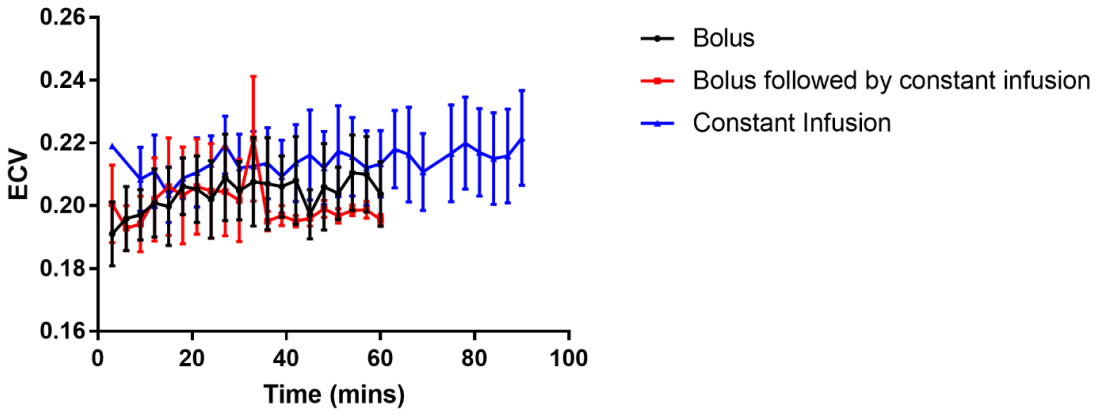

Figure 2-5: The time course of changes in the measured ECV of Gd-DTPA in healthy myocardium in five canine subjects, with glucose suppression, measured every 3 minutes for up to 90 minutes after start of injection.

Data are presented as mean ± SEM, N=5 for each injection method. All injection protocols ended at 60 minutes, except for the constant infusion of Gd-DTPA, which included an additional 30-minute washout period. No significant difference was found when comparing the different injection methods.

2.3.4 Glucose metabolism using Patlak parameter estimates

Figure 2-6 shows the influx constant, Ki, a marker of glucose metabolism for healthy non-infarcted cardiac myocardium with and without glucose suppression using heparin and a continuous infusion of 20% lipid. There was no significant effect of glucose suppression on the measured Ki irrespective of which infusion protocol was used (bolus-only: p=0.19; constant infusion-only: p=0.36; bolus followed by constant infusion: p=0.93).

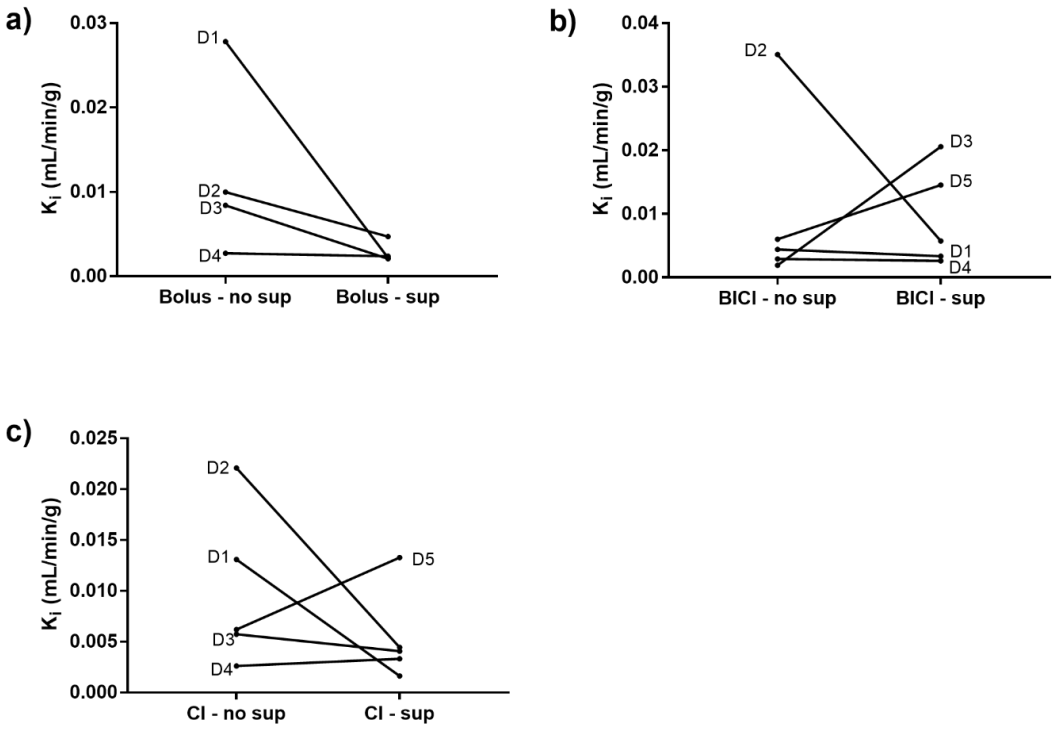

Figure 2-6: The effect of glucose suppression on healthy non-infarcted cardiac myocardium Ki, a marker of glucose metabolism.

This figure shows the Ki of each individual canine with and without suppression following a a) bolus injection, b) BI + CI injection and c) CI only for each individual canine. No significant differences were found using paired t-tests. The individual dogs are identified as D1 to D5 and suggests that the pattern of differences with and without suppression is not related to individual animals.

2.3.5 Change in T1 during each contrast delivery method

As shown in figure 2-7, while values in the bolus experiment are increasing over time, in the bolus followed by CI, values are relatively constant between 10 and 30 minutes and in a constant infusion only, they are best between 40 and 60 minutes. These durations may also be increased by increasing the duration of the infusion as they only change when the infusion is terminated. It is important to point out that these timelines are for healthy tissue with blood flow of approximately 1 ml/min/g and they may vary in ischemic tissue, e.g. infarcted tissue, with reduced blood flow.

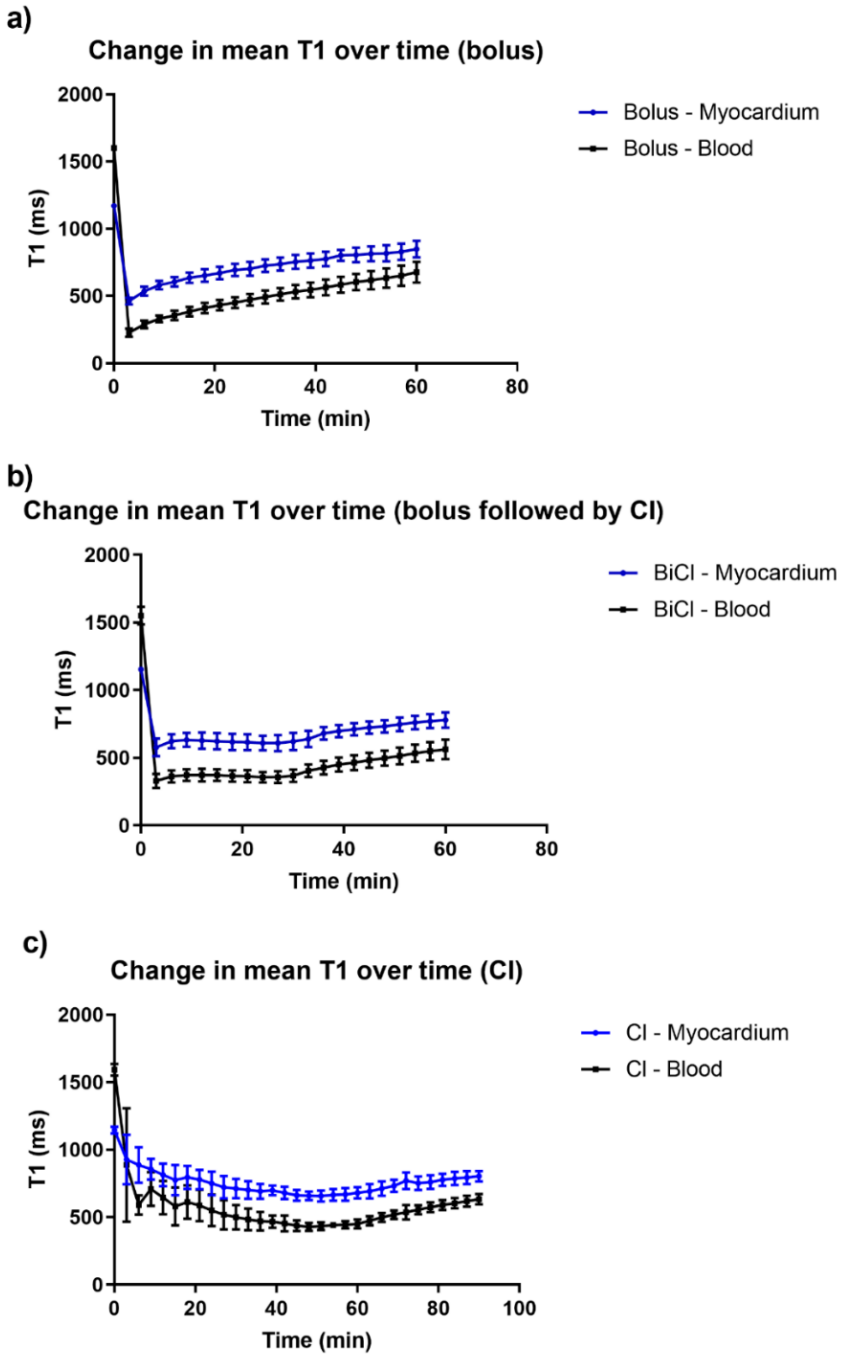

Figure 2-7: Changes in T1 values over time in both the myocardium and the blood.

These are mean values +/- SD for all 5 canines in the suppressed glucose myocardium group.

2.4 Discussion

The main findings were: (a) The suppression of myocardial uptake of [^{18}F]FDG with heparin and lipid infusion may alter the determination of myocardial ECV using GBCA, (b) the infusion protocol used had no effect on the calculated ECV; but with the caveat of (c) ECV measured using a bolus of Gd-DTPA was underestimated if measured prior to the first 15 minutes following injection and (d) combining Gd-DTPA and FDG for concurrent injection for hybrid imaging showed no changes in pH or radiochemical purity of [^{18}F]FDG.

This work demonstrates the equivalence of the determination of ECV under the different injection scenarios for the collection of a T1 map over a single slice when the concentration of GBCA did not vary significantly during the breath hold needed for acquisition. However, a T1-map of ECV over the entire left ventricular myocardium is needed if inflammatory disease is non-uniformly distributed as is most often the case e.g. post myocardial infraction, cardiac sarcoidosis, etc[21,22]. As a 3D T1 map would require 10 or more 2D slices to be acquired each over a breath hold in a sick patient, this could easily take 10 or more minutes[21,22]. During that time, GBCA concentration would be dropping after a bolus injection, rendering the T1 maps inconsistent between slices. However, contrast agent concentrations vary more slowly and to a lesser degree during a constant infusion either following a bolus injection between 10 and 30 minutes, or after the first 40 min of a constant infusion only protocol (see figure 2-7). Although we did not assess the effect of prolonged acquisition times (with accompanying ongoing changes in contrast agent concentrations) on the resulting T1 map, avoiding the variations in blood concentration associated with the use of only bolus injections of GBCA would minimize fluctuations in blood tracer concentrations and give us more accurate and precise measurements of ECV. This would also be expected in remote myocardium following myocardial infarction, provided myocardial blood flow remains close to 1 ml/min/g as has been previously shown in this animal model[6,8,23]. It will be important to validate this concentration dynamic as a function of injection protocol in myocardium with compromised blood flow in regions with microvascular obstruction where blood flow is severely reduced[24].

For the clinical assessment of inflammation by [^{18}F]FDG using simultaneous PET/MRI, suppression of physiological myocardial glucose uptake is generally achieved by a method similar to the one we have used in our study, with the intralipid infusion replaced by a high fat diet[25]. No significant difference was found between measured ECV with glucose suppression and non-suppressed myocardium when comparing individual groups. When comparing suppressed vs non-suppressed irrespective of injection protocol, there was a significant difference (0.21 ± 0.02 vs 0.18 ± 0.01, corresponding to a 13% increase; $p = 0.002$). Further experiments are necessary to investigate whether this effect is from the lipid infusion, which could decrease the hematocrit. This may be an important consideration for experiments utilizing a lipid infusion while measuring ECV, although further experiments are necessary to examine whether the lipid infusion affects the hematocrit or another part of ECV.We also saw that ECV appears to increase over the initial 18 minutes following the bolus injection protocol. This suggests that to assess ECV accurately, one should wait at least 20 minutes and then perform the T1 map acquisitions[26,27]. Schelbert et al. also reported a small but statistically significant change of V_e (extravascular extracellular volume fraction) after bolus injection of GBCA, which is consistent with our results[27]. Clinically, an increase in the measured ECV over 18 minutes may be relevant if the MOLLI sequence is not acquired at identical post-contrast delay times[27]. This might require careful attention to imaging delay time when using a bolus or post-scan correction to compensate for the small increase[27].

While the safety of FDG and GBCA have both been determined independently, to the best of our knowledge the compatibility of the two contrast agent mixture has not been shown. For instance, the linear and cyclic aminopolycarboxylic acid chelators could potentially conjugate to FDG via glycosylation. De-fluorination was another minor concern. In this paper, we show an initial assessment at ambient temperature that neither attachment of chelate to the FDG nor loss of fluoride were observed. Although this data is consistent with the safety of a combined injection, further investigations on the effect of physiological temperature during mixing and blood sampling after concurrent injection would further increase confidence.

In our study we did not see the expected decrease in Ki, a measure of glucose uptake, with glucose suppression. When we compare the non-suppressed group to the suppressed group independent of injection strategy, suppression did not have a significant effect on glucose metabolism ($p=0.27$, non-suppressed 0.010 ± 0.008, suppressed 0.0063 ± 0.009). In all cases the non-suppressed values were below 0.035 ml/min/g. In the suppressed group, all were below 0.02, with 11 of the 14 below 0.005 ml/min/g. It is clear that suppression worked well for the non-suppressed values above 0.02 but had minimal and even contrary results for values already as low as can be achieved with suppression. As all animals were fasted but the suppressed group was also given heparin and intralipid, perhaps the requirement to fast canines for 12-16 hours prior to anesthetic was sufficient to suppress glucose uptake, or the use of only 5 animals may not have provided enough statistical power to establish the presence of a statistically meaningful effect (figure 2-6a and c do suggest a downward trend). Our results are promising as hybrid PET/MR imaging is being used more and it gives the ability to image aspects of inflammation through both modalities simultaneously. To this we have shown in a canine model that concurrent FDG and GBCA injections can be safely used, and do not affect the glucose metabolism and ECV measurements which reduces overall imaging time and ensures optimal registration of the PET and MRI images.

However, our work has limitations: a) While the sample size of this experiment is relatively small, this research provides a starting point for future clinical or pre-clinical experiments. Power analysis has shown that significant differences in ECV for suppressed vs unsuppressed tissue could be reached in each injection protocol with as few as 7 animals in CI and bolus followed by CI group whereas a total of 13 animals would be needed in the bolus only group if the mean and standard deviation were the same as in the current groups. b) Only partition coefficient, and not ECV, was evaluated due to lack of hematocrit data, but results can be directly translated to ECV for clinical relevance as the only difference between partition coefficient and ECV is hematocrit correction and thus a hematocrit of 0.45 was assumed for this study. c) The use of a linear gadolinium chelator, Gd-DTPA (Magnevist) in our experiment has been discontinued (after the start of this experiment) in favour of macrocyclic GBCA's due to association with an increased risk of brain retention. However, ECV represents a physiological

parameter and is derived from the ratio of T1 signal values and is likely not affected by type of extracellular GBCA used and therefore our results can still be translated for clinical relevance. d) Hybrid PET/MRI is currently not in widespread clinical use. While this may change as the modality becomes more accessible and more methods are developed, not many research centres and hospitals will currently be able to take advantage of these results.

2.5 Conclusion

Suppression of myocardial uptake of [^{18}F]FDG, through a continuous lipid infusion and an intravenous heparin injection, has no effect on ECV using GBCA compared to unsuppressed tissue. Additionally, the infusion protocol used (bolus alone, CI alone, bolus followed by CI) had no effect on the calculated ECV at equilibrium, however, ECV measured using a bolus of Gd-DTPA was underestimated if measured prior to the first 15 minutes following injection. Lastly, we have shown that combining Gd-DTPA and FDG for concurrent injection for hybrid imaging showed no changes in pH or radiochemical purity of [^{18}F]FDG. Therefore, simultaneous PET/MRI is promising as it gives the ability to accurately measure complementary aspects of inflammation through both modalities, specifically cardiac inflammation alongside diffuse fibrosis and this has potential application in remote myocardium.

2.6 References

1. Kidambi A, Motwani M, Uddin A, Ripley DP, McDiarmid AK, Swoboda PP, et al. Myocardial Extracellular Volume Estimation by CMR Predicts Functional Recovery Following Acute MI. *JACC Cardiovasc Imaging* 2017. doi:10.1016/j.jcmg.2016.06.015

2. Taylor AJ, Salerno M, Dharmakumar R, Jerosch-Herold M. T1 Mapping Basic Techniques and Clinical Applications. *JACC Cardiovasc Imaging* 2016. doi:10.1016/j.jcmg.2015.11.005

3. Radenkovic D, Weingärtner S, Ricketts L, Moon JC, Captur G. T1 mapping in cardiac MRI. *Heart Fail Rev* 2017. doi:10.1007/s10741-017-9627-2

4. Aime S, Caravan P. Biodistribution of gadolinium-based contrast agents, including gadolinium deposition. In: *Journal of Magnetic Resonance Imaging*. ; 2009. doi:10.1002/jmri.21969

5. Kim RJ, Wu E, Rafael A, Chen EL, Parker MA, Simonetti O, et al. The use of contrast-enhanced magnetic resonance imaging to identify reversible myocardial dysfunction. *N Engl J Med* 2000. doi:10.1056/NEJM200011163432003

6. Thornhill RE, Prato FS, Wisenberg G, Moran GR, Sykes J. Determining the extent to which delayed-enhancement images reflect the partition-coefficient of Gd-DTPA in canine studies of reperfused and unreperfused myocardial infarction. *Magn Reson Med* 2004;52:1069-1079. doi:10.1002/mrm.20236

7. Salerno M, Janardhanan R, Jiji RS, Brooks J, Adenaw N, Mehta B, et al. Comparison of methods for determining the partition coefficient of gadolinium in the myocardium using T1 mapping. *J Magn Reson Imaging* 2013. doi:10.1002/jmri.23875

8. Diesbourg LD, Prato FS, Wisenberg G, Drost DJ, Marshall TP, Carroll SE, et al. Quantification of myocardial blood flow and extracellular volumes using a bolus injection of Gd-DTPA: Kinetic modeling in canine ischemic disease. *Magn Reson*

Med 1992. doi:10.1002/mrm.1910230205

9. Arai AE. The cardiac magnetic resonance (CMR) approach to assessing myocardial viability. *J Nucl Cardiol* 2011. doi:10.1007/s12350-011-9441-5

10. Wilk B, Wisenberg G, Dharmakumar R, Thiessen JD, Goldhawk DE, Prato FS. Hybrid PET/MR Imaging in Myocardial Inflammation Post-Myocardial Infarction. *J Nucl Cardiol* 2019;Epub ahead.

11. Scholtens AM, Verberne HJ, Budde RPJ, Lam MGEH. Additional heparin preadministration improves cardiac glucose metabolism suppression over low-carbohydrate diet alone in 18F-FDG PET imaging. *J Nucl Med* 2016. doi:10.2967/jnumed.115.166884

12. Prato FS, Butler J, Sykes J, Keenliside L, Blackwood KJ, Thompson RT, et al. Can the Inflammatory Response Be Evaluated Using 18F-FDG Within Zones of Microvascular Obstruction After Myocardial Infarction? *J Nucl Med* 2015;56:299-304. doi:10.2967/jnumed.114.147835

13. Joerges J, Schulz T, Wegner J, Schumacher U, Prehm P. Regulation of cell volume by glycosaminoglycans. *J Cell Biochem* 2012. doi:10.1002/jcb.23360

14. Scholtens AM, van den Berk AM, van der Sluis NL, Esser JP, Lammers GK, de Klerk JMH, et al. Suppression of myocardial glucose metabolism in FDG PET/CT: impact of dose variation in heparin bolus pre-administration. *Eur J Nucl Med Mol Imaging* 2020. doi:10.1007/s00259-020-04713-1

15. Lawrence J, Chang YMR, Szladovits B, Davison LJ, Garden OA. Breed-specific hematological phenotypes in the dog: A natural resource for the genetic dissection of hematological parameters in a mammalian species. *PLoS One* 2013. doi:10.1371/journal.pone.0081288

16. White SK, Sado DM, Fontana M, Banypersad SM, Maestrini V, Flett AS, et al. T1 Mapping for Myocardial Extracellular Volume Measurement by CMR. *JACC Cardiovasc Imaging* 2013. doi:10.1016/j.jcmg.2013.01.011

17. Patlak CS, Blasberg RG, Fenstermacher JD. Graphical evaluation of blood-to-brain transfer constants from multiple-time uptake data. *J Cereb Blood Flow Metab* 1983;3:1-7. doi:10.1038/jcbfm.1985.87

18. Higgins PJ, Garlick RL, Bunn HF. Glycosylated hemoglobin in human and animal red cells. Role of glucose permeability. *Diabetes* 1982. doi:10.2337/diab.31.9.743

19. Anazodo U, Kewin M, Finger E, Thiessen J, Hadway J, Butler J, et al. Preliminary evaluation of MRI-derived input function for quantitative measurement of glucose metabolism in an integrated PET-MRI. *EJNMMI Phys* 2015;2:1-2. doi:10.1186/2197-7364-2-s1-a80

20. Lortie M, Beanlands RSB, Yoshinaga K, Klein R, DaSilva JN, DeKemp RA. Quantification of myocardial blood flow with 82Rb dynamic PET imaging. *Eur J Nucl Med Mol Imaging* 2007;34:1765-1774. doi:10.1007/s00259-007-0478-2

21. Lurz JA, Luecke C, Lang D, Besler C, Rommel KP, Klingel K, et al. CMR–Derived Extracellular Volume Fraction as a Marker for Myocardial Fibrosis: The Importance of Coexisting Myocardial Inflammation. *JACC Cardiovasc Imaging* 2018. doi:10.1016/j.jcmg.2017.01.025

22. Haaf P, Garg P, Messroghli DR, Broadbent DA, Greenwood JP, Plein S. Cardiac T1 Mapping and Extracellular Volume (ECV) in clinical practice: A comprehensive review. *J Cardiovasc Magn Reson* 2016. doi:10.1186/s12968-016-0308-4

23. Thornhill RE, Prato FS, Wisenberg G, White JA, Nowell J, Sauer A. Feasibility of the single-bolus strategy for measuring the partition coefficient of Gd-DTPA in patients with myocardial infarction: Independence of image delay time and maturity of scar. *Magn Reson Med* 2006. doi:10.1002/mrm.20830

24. Bekkers SCAM, Yazdani SK, Virmani R, Waltenberger J. Microvascular Obstruction. Underlying Pathophysiology and Clinical Diagnosis. *J Am Coll Cardiol* 2010. doi:10.1016/j.jacc.2009.12.037

25. Nensa F, Tezgah E, Schweins K, Goebel J, Heusch P, Nassenstein K, et al. Evaluation of a low-carbohydrate diet-based preparation protocol without fasting for cardiac PET/MR imaging. *J Nucl Cardiol* 2017. doi:10.1007/s12350-016-0443-1

26. Al-Wakeel-Marquard N, Rastin S, Muench F, O h-Ici D, Yilmaz S, Berger F, et al. Cardiac T1 mapping in congenital heart disease: bolus vs. infusion protocols for measurements of myocardial extracellular volume fraction. *Int J Cardiovasc Imaging* 2017. doi:10.1007/s10554-017-1191-2

27. Schelbert EB, Testa SM, Meier CG, Ceyrolles WJ, Levenson JE, Blair AJ, et al. Myocardial extravascular extracellular volume fraction measurement by gadolinium cardiovascular magnetic resonance in humans: Slow infusion versus bolus. *J Cardiovasc Magn Reson* 2011. doi:10.1186/1532-429X-13-16

Chapter 3

3 Tracking the progress of inflammation with PET/MRI in a canine model of myocardial infarction

3.1 Introduction

After a myocardial infarction (MI), patients remain at risk of adverse events, including heart failure[1]. Risk factors for these adverse events include infarct size[2,3] and extent of microvascular obstruction[4]. Both are independent predictors of left ventricular remodeling. Inflammation also plays a key role in the response to infarction and its evolution will play a key role in determining how the left ventricle remodels. Both MRI and FDG-PET may provide insights into the evolution of myocardial injury and inflammation.

Using MRI, T1 maps can be obtained and used to measure the extra-cellular volume, an indicator of tissue edema, a common accompaniment of inflammation. ECV is elevated within infarcted tissue post-MI, starting in the first few hours[5]. However, little is known about the ECV in remote non-infarcted, non-ischemic myocardium as the left ventricle remodels [6]. In such tissue, fibrosis, cellular inflammation and edema may evolve gradually which would result in a slow increase in ECV, which might only be measurable over extended periods of time (months)[7,8].

In addition to defining the extent of irreversible injury, the delayed enhancement protocol also provides a volume measure of microvascular obstruction within the infarct which we designate hereafter as Infarcted Obstructed Tissue or IOT. IOT has very compromised blood flow with reduced tracer delivery. Little is known about the ECV in the IOT and how it changes in time post-MI.

In order to quantitate ECV in remote tissue (RT), infarcted tissue excluding any region with significant microvascular obstruction, Infarcted Non-Obstructed Tissue or INOT, and IOT, single-slice breath hold T1 maps need to be acquired spanning the entire heart[9–

[11]. However, this requires acquisition during which the concentration of GBCA in the blood and tissue should not be changing significantly, as it normally would following a bolus injection[9–11]. However, it has been known for some time that a bolus injection followed by a constant infusion of GBCA, given the correct timing and dose distribution between the bolus and constant infusion, achieves relatively rapid constant blood concentrations[9–12]. Despite this, few studies have investigated just using a prolonged constant infusion to measure ECV in the RT, INOT and IOT[13].

Post-MI, cellularly mediated inflammatory processes clear out myocardial cellular debris and stabilize the region of infarction with scar tissue. When using FDG to image macrophage mediated cardiac inflammation, an important consideration is effective suppression of the glucose uptake by cardiomyocytes to get an accurate picture of inflammation, without the confounding effect of myocardial glucose uptake. This is generally achieved with one or more of: fasting, a high-fat diet, heparin injection, and in animals, a lipid infusion[14]. In addition to the concern regarding suppression of myocardial glucose uptake, an additional concern with FDG PET imaging in acute MI is the potential effect of IOT on the apparent inflammation profile: lower FDG activity in the center of the infarct (i.e. the IOT) may be primarily the result of reduced delivery of this tracer as a result of the severely compromised flow. Since myocardial infarction patients with IOT have poorer outcomes it is imperative to be able to accurately quantitate the inflammatory processes within this region (without the confounding effects of compromised tracer delivery), in order to plan future interventions to improve prognosis. Previously, a constant infusion has been used in the brain to penetrate the ischemic region post-stroke[15]. We propose that a constant infusion of Gd-DTPA and FDG would allow penetration of the IOT to allow better characterization of the inflammatory response, both macrophage mediated, and that associated with tissue fibrosis and edema, without the constraints of compromised tracer delivery.

Here we have investigated the potential application of a simple combined constant infusion of Gd-DTPA and FDG to quantitate inflammation, ECV and function in RT, INOT and IOT in a canine model of permanent coronary artery occlusion from 3 to 42 days post-MI.

3.2 Methods

3.2.1 Animals and Surgical Preparation

This study was approved by the Animal Care Committee of Western University. Eight adult, female, bred-for-research hounds were used. Anesthesia for surgery and imaging was induced using Propofol and maintained with 1.5% – 2% isoflurane. Animals underwent imaging at baseline (n = 5), 3-4 (n = 6), 7-8 (n = 7), 14-15 (n = 6), 21-22 (n = 8) and 38-44 (n = 8) days post-MI (Figure 3-2). Due to technical difficulties, not all animals were imaged at all time points. MI was induced by permanently placing a snare ligature around the left anterior descending coronary artery during left thoracotomy.

3.2.2 PET Imaging

Animals were fasted between 16 and 21 hours before the start of imaging. To further suppress myocardial glucose uptake, twenty minutes before the constant infusion of FDG, 2000 units of heparin were administered intravenously and an infusion of 20% lipid (Intralipid; Baxter Healthcare Corporation) at a rate of 0.25 mL/min/kg was administered intravenously over a 50-minute period starting immediately after the administration of heparin (see figure 3-1 for a sample image). Note that whereas in humans diet and heparin are sufficient for 95% suppression[14], in canines intralipid infusion is also needed as we have previously reported[16].

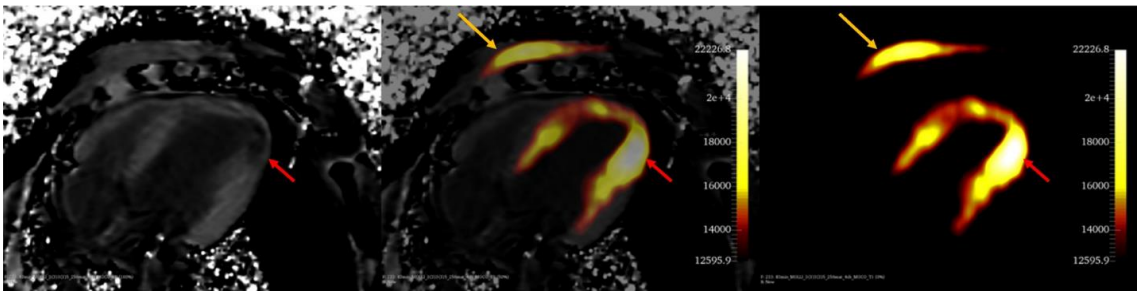

Figure 3-1:FDG uptake at day 7 post-MI, 10 minutes after the end of the constant infusion.

This figure shows the uptake of FDG in the myocardium highlighting the infarcted area, 7 days post-MI, 70 minutes after the start of the infusion. From left to right, there are a

T1 map, a T1 map overlaid with FDG PET and PET only. It should be noted that there is some uptake within the entire myocardium and not just the infarct (red arrow). A longer washout time would likely eliminate a large portion of this. The method of suppression has also been previously used and found to be adequate in this animal model with a bolus injection[99]. This image also highlights the incision site (orange arrow) which shows that macrophage FDG uptake is not affected by suppression of myocardial glucose uptake.

A 60-minute constant infusion of both FDG (0.17 MBq/min/kg; Fludeoxyglucose (^{18}F) Injection, produced in-house at the Lawson Cyclotron Facility) and Gd-DTPA (0.004 mmol/min/kg for a total dose of 0.24 mmol/kg, Magnevist; Bayer Inc.) was started simultaneously with the beginning of the list mode PET acquisition. In addition to the 60-minute infusion, the PET acquisition was extended to a further 10-minute washout in 3 dogs and a 30-minute washout in 5 dogs. The PET data was reconstructed in 3-minute frames using a 3D Ordered Subset Expectation Maximization reconstruction (3 iterations, 21 subsets, 172 x 172 x 127 matrix size, zoom of 2 and 4 mm Gaussian filter). MR-based attenuation correction was achieved using a two-point Dixon MRI sequence and segmented into water, fat, lung and air with constant attenuation coefficients for each tissue[17]. The PET voxel size was 2.09 x 2.09 x 2.03 mm.

3.2.3 Cardiac MR imaging

MR imaging was started 60 minutes prior to the beginning of the constant infusion. Sequences included short axis cine stacks of the left ventricle synchronized to the ECG signal (true fast imaging with steady-state free precession (TrueFISP), slice thickness 6 mm, 256 x 216 voxels, voxel size 1.09 x 1.09 mm, ~12s acquisition time, based on heart rate) where each slice was acquired during a breath hold; a 3D T1 weighted image (ECG triggered Inversion Recovery sequence with navigator echo for respiratory gating, 256 x 200 x 112 voxels, voxel size 0.625 x 0.625 x 0.9 mm, ~4 minute acquisition time, based on heart and respiratory rate); T1 maps (ECG-triggered modified Look-Locker inversion recovery sequence, slice thickness 6 mm, 256 x 144 voxels, voxel size 1.09 x 1.09 mm, ~12s acquisition time, based on heart rate) in a single breath hold to acquire 2-chamber and 4-chamber views of the heart (Siemens Work In Progress). In 7 animals, T1 maps and 3D T1 weighted images were acquired in 10 minute intervals. In the other animal, 4-

chamber view T1 maps were acquired every 3 minutes and a 3D T1 weighted image was acquired 70 minutes into the PET scan (i.e. 10 minutes after the infusion was stopped). See figure 3-2 for details on the timing of both the MRI and PET data acquisitions.

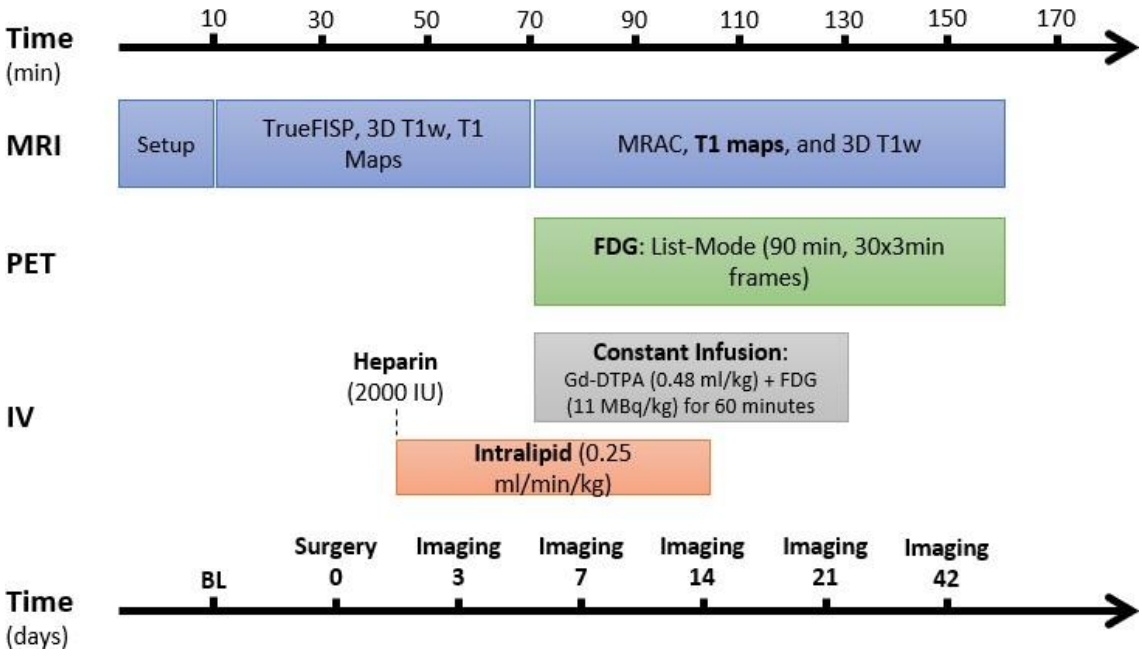

Figure 3-2: Experimental Protocol.

After the subject was setup in the MR scanner, MRAC, localizers, pre-contrast images and cine images were acquired. During this time, heparin was injected and lipids where infused. Then, a constant infusion of Gd-DTPA and FDG was started and T1 maps and 3D T1-weighted images were acquired in conjunction with FDG list-mode data.

3.2.4 Data Analysis

3.2.4.1 Regions of Interest

Regions of interest (ROIs) were manually drawn onto the final Gd-enhanced T1 map which was then automatically transferred to all other T1 maps. The ROIs outlined were the IOT, the INOT, two samples of RT, and the blood pool. Note that the IOT only included tissue with microvascular obstruction and the INOT was all other infarcted

tissue, excluding the IOT. The 2D ROIs were then also transferred to the corresponding slice of PET data. Figure 3-3 shows the selection of the three regions of interest (RT, INOT and IOT) and the selection of the blood pool region within the left ventricular cavity all taken 10 minutes after the 60-minute constant infusion. Manual adjustment of some images in the series was applied to offset changes in heart position. Edges were also avoided when drawing ROIs to minimize partial volume averaging from voxels at the myocardial-blood pool border.

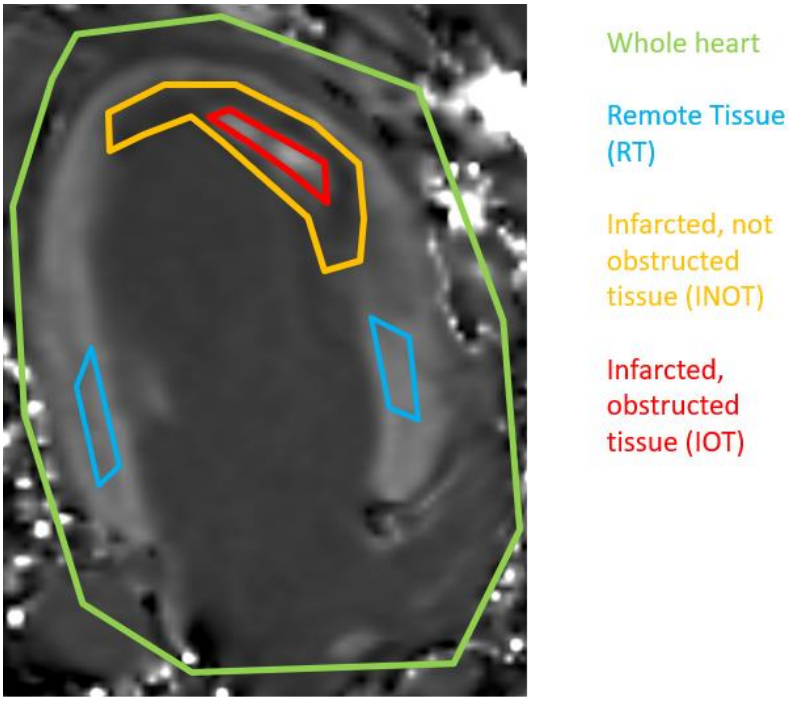

Figure 3-3: Region of interest selection post-MI on a 2-chamber T1 map.

Glucose metabolism and extracellular volume (ECV) measurements were calculated at four separate regions (two in remote tissue (RT), one in infarcted not obstructed (INOT), excluding tissue with microvascular obstruction, and one in infarcted obstructed tissue (IOT)).

3.2.4.2 Glucose Metabolism

FDG concentration curves of all ROIs were fit to the Patlak model[18] as discussed in section 2.2.4.

3.2.4.3 Extracellular Volume Fraction

ECV maps calculated at the 60-minute time point in the constant infusion were used to compare changes over time. For the estimation of ECV equilibrium was assumed to be reached when the difference in ECV between acquisitions was less than 5%, as done by White et al[23]. 76 out of 868 T1 maps could not be analyzed due to excess noise and were excluded. ECV was calculated as discussed in section 2.2.3.

3.2.4.4 Volumes of IOT and INOT

To determine the volume of the IOT and INOT, gadolinium-enhanced 3D T1 weighted images were segmented by a single observer using the 3D Slicer Segment Editor (http://www.slicer.org/)[24]. Thresholds were determined for IOT, INOT and RT and drawn using the Threshold Paint function. The threshold was set for each experiment to exclude the IOT and occasionally had to be adjusted between slices.

3.2.4.5 MRI Measurement of Heart Function

Using Slicer to analyze the ECG triggered short axis TrueFISP image series, the blood pool can be segmented. A single operator defined the blood pool throughout the series and determined the phases of the cardiac cycle with the highest and the lowest blood volume. These were defined as the end diastolic volume (EDV) and end systolic volume (ESV). The ejection fraction (EF) was calculated using the equation,

$$EF = \frac{EDV - ESV}{EDV} \cdot 100\%.$$

These results were compared to the automatic segmentation generated with commercial cardiovascular image analysis software, circle cvi42 (Circle Cardiovascular Imaging Inc, Calgary), and were found to be within 5% when the same number of short axis slices were used. As circle cvi42 failed in a number of sets of data we report values from Slicer. Slices were excluded due to poor image quality, if the aorta was visible or if they were past the apex.

3.2.4.6 Statistics

Statistical analysis was performed using GraphPad Prism (GraphPad Software, La Jolla, CA). All data is presented as mean ± standard error of the mean. Repeated-measures analysis of variance (ANOVA) was performed on the days post-MI, prior to washout and following washout. Comparison of differences in RT, INOT and IOT, as well as during washout of Gd-DTPA, was assessed with paired and unpaired two-tailed t tests. A p-value of <0.05 was considered to be statistically significant. Corrections for multiple comparisons were performed using a Bonferroni multiple comparison test.

3.3 RESULTS

3.3.1 Volume of IOT and INOT

Figure 3-4 shows the T1 maps determined every 10 minutes for one dog. Penetration over time into the IOT can be seen. ROIs were drawn on the 73-minute map to allow for some washout from the blood pool. Measuring the volume of the INOT showed a decrease over time in all animals with a mean starting value of 15174 mm^3 at day 3 and a final value of 4939 mm^3 at day 43, as shown in figure 3-5. Statistical differences were observed starting at day 14 ($p = 0.014$) and then also on day 21 ($p = 0.0031$) and day 43 ($p = 0.0003$).

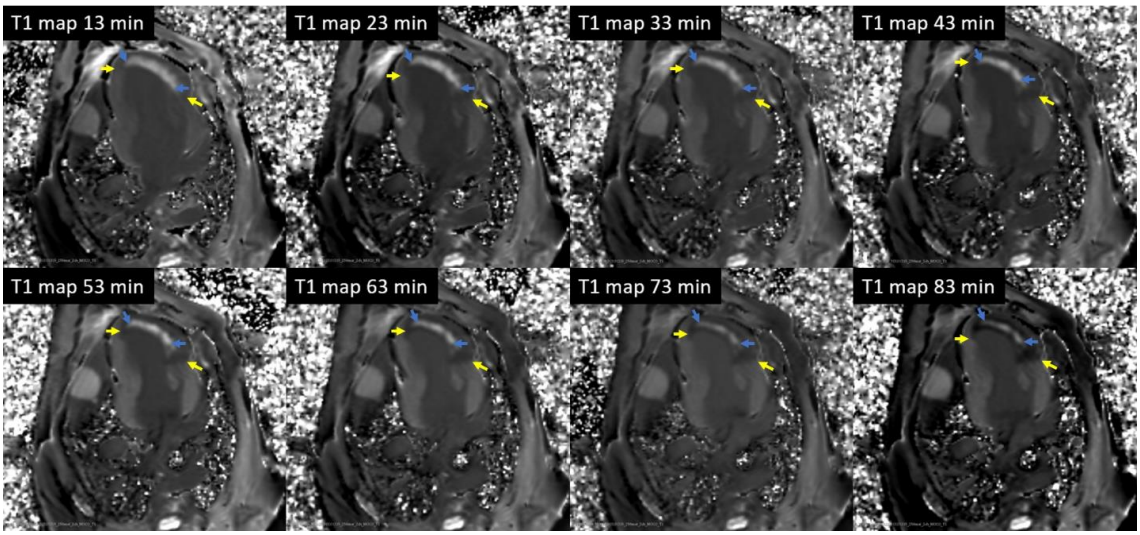

Figure 3-4: 2-Chamber T1 maps throughout the constant infusion at day 7.

This image shows the influx of tracer into the IOT (blue arrows) and INOT (yellow arrows).

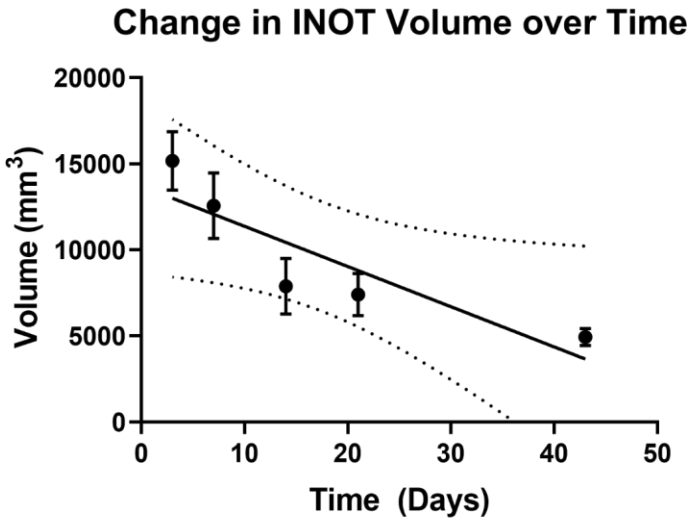

Figure 3-5: Change in INOT Volume over Time.

The INOT volume starts at its highest at day 3 and decreases over 42 days in all 8 animals. Day 3: n = 7, Day 7: n = 7, Day 14: n =5, Day 21: n = 8, Day 42: n = 6.

3.3.2 Extracellular Volume

There was a significant increase in RT at minute 60 on day 14 (p=0.0336) and day 21 (p=0.0205) post-MI compared to the baseline healthy myocardial ECV as shown in figure 3-6. There was no significant difference in RT ECV on day 3 (p=0.50), day 7 (p=0.086) and at day 40 post-MI (p=0.0597) relative to the baseline myocardial ECV.

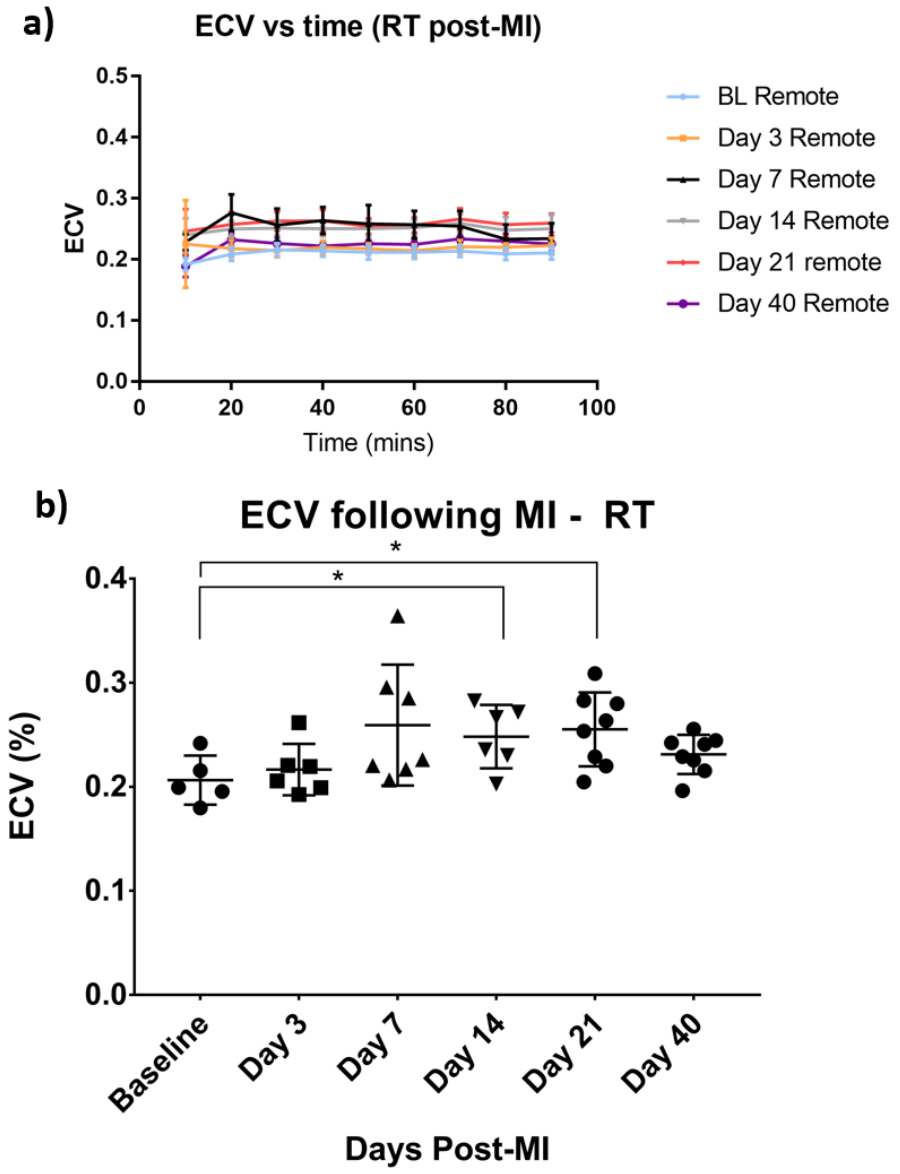

Figure 3-6: ECV in remote tissue post-MI.

*a) ECV (mean ± SEM) varies in the days following MI in the RT over the duration of the scan using the constant infusion protocol. b) ECV values for each canine at each respective day post-MI in RT 60 minutes into the scan, at equilibrium, prior to washout of Gd-DTPA. * represents a significant difference of ($p<0.05$)*

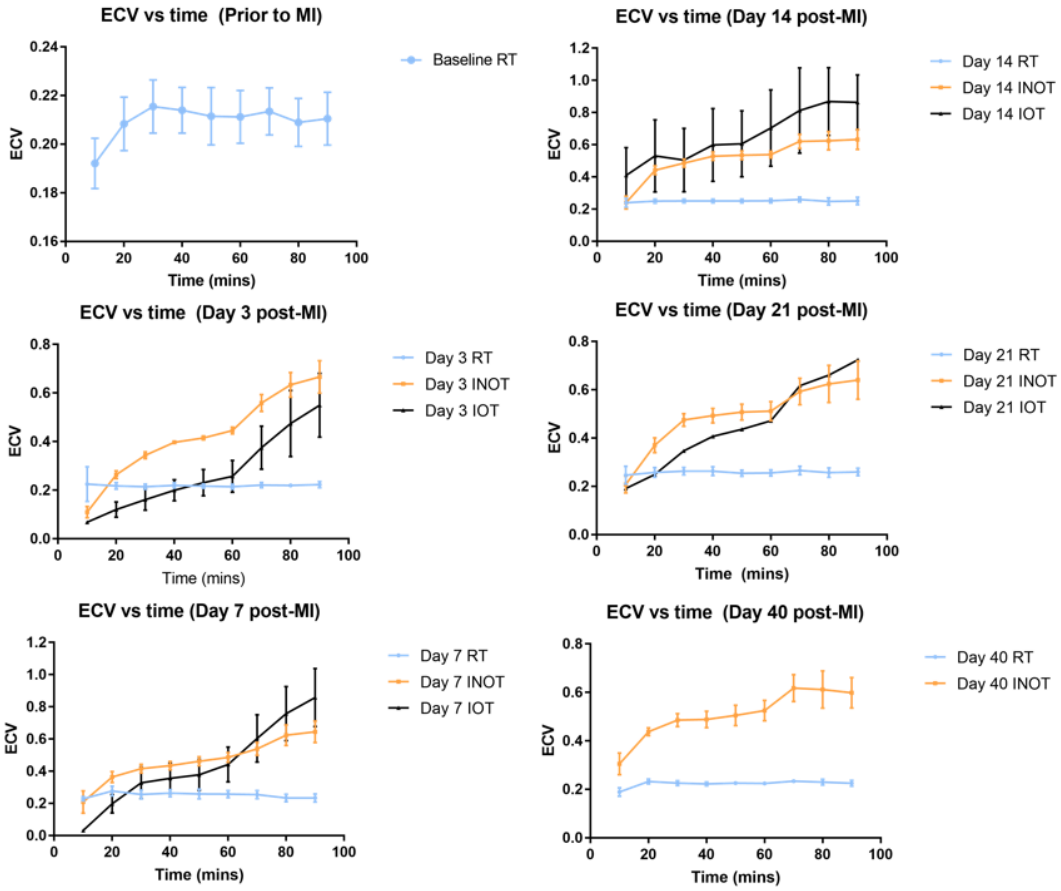

Figure 3-7: ECV measurements pre- and post-MI in all tissue types.

ECV measurements were calculated in eight canine subjects measured every 10 minutes for up to 90 minutes after starting the constant infusion of Gd-DTPA. ECV was calculated in RT, INOT and IOT at days 3, 7, 14, 21 and 40 post-MI and prior to MI. Data represented are mean ± SEM. Constant infusion of Gd-DTPA was terminated at 60 minutes followed by 30 minutes of washout. Only one canine showed an IOT at day 21 and no IOT was seen for any canines 40 days post-MI. Figure 3-7 shows how the measured ECV varies with time for RT, IOT and INOT. Clearly RT reaches equilibrium

as quickly as seen in the normal myocardium measured at baseline with no change during washout. The measurement in the INOT reaches equilibrium well within the 60 min constant infusion at all days except at day 3. The measurement in the IOT does not reach equilibrium except perhaps at day 7, though there was still a significant difference between the 50 minute and 60 minute timepoints. It is clear that the measurement of ECV is not accurate during washout for either INOT or IOT, independent of time, post-MI.

As shown in Figure 3-7, ECV was significantly elevated in the INOT myocardium at minute 60 compared to RT myocardium at all time points post-MI (days 3, 7, 14, 21 and 40) ($p<0.001$).

In the INOT at day 3, there was a significant increase at minute 60 compared to minute 50 ($p=0.024$). At all other days post-MI there was no significant difference between minute 60 and minute 50 (day 7: $p=0.062$; day 14: $p=0.39$; day 21: $p=0.47$; day 40: $p=0.11$).

In the IOT, there was no significant difference in ECV at day 3 at minute 50 and minute 60 ($p = 0.17$). There was a significant difference between minute 50 and 60 at day 7 ($p<0.01$), however, at all other time points there was an insufficient number of canines with an IOT to do proper analysis (N=3 for day 14, N=1 for day 21, N=0 for 40 days).

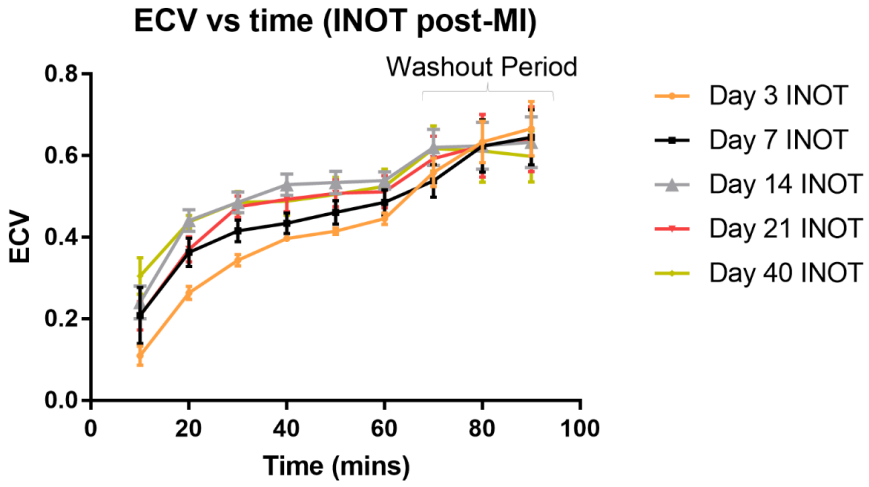

Figure 3-8: ECV measurements in the INOT post-MI.

This figure shows ECV values for the INOT tissues for all canines post infarction as a function of 60 minute constant infusion followed by 30 minutes of washout. Measured ECV is increased during the washout period of Gd-DTPA.

Figure 3-8 shows ECV values for the INOT tissues for all canines post-MI as a function of 60-minute constant infusion followed by 30 minutes of washout. The measured ECV is significantly increased during the washout period of Gd-DTPA (see figure 3-9). This was also seen for the IOT tissue at day 3 at 70, 80 and 90 min of washout and at day 7 at 90 min while at days 14, 21 and 40 there was insufficient data for analysis as the IOT tended to resolve into INOT.

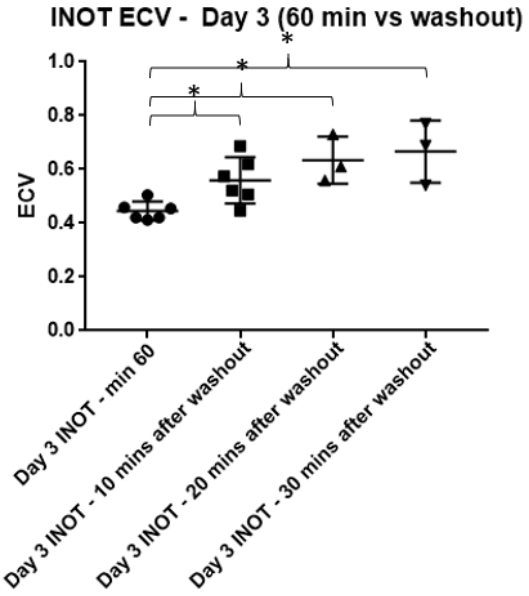

Figure 3-9: ECV in the INOT 3 days post-MI.

*Measured ECV in the INOT three days following myocardial infarction at minute 60, compared to times following washout (10, 20, 30 minutes into washout, $p = 0.0035$, $p = 0.0181$, $p = 0.0468$, respectively). * represents a significant difference of $p<0.05$.*

3.3.3 Patlak Parameter Estimates

Figure 3-10 shows the Ki for all 8 animals in remote myocardium as a function of time post MI. Although it appears that there was an increase in some animals early post-MI, no significant changes were seen (day3: p=0.38; day 7 p = 0.32; day 14: p = 0.11; day p = 21: 0.19; day 43: p = 0.63).

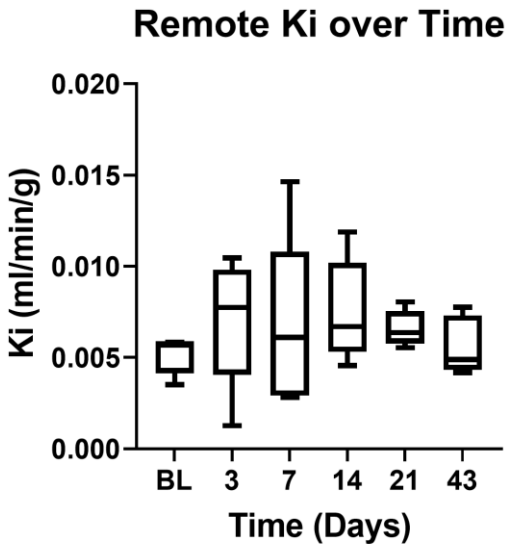

Figure 3-10: Remote tissue Ki pre- and post-MI.

Remote Ki shows no significant difference over time though it appears as though there may be a rise over the first week. This plot shows the mean and interquartile ranges (box) and the maximum and minimum values (whiskers).

Figure 3-11 shows the glucose metabolism for the INOT, Ki, as a marker of glucose metabolism, significantly exceeds baseline (0.00514+/- 0.00045) at all points other than day 43, when glucose metabolism returns to the baseline value. While day 3 is not significantly different from day 7, it is higher than all other values, showing that the inflammatory response appears largest within the first week of infarct. This decrease over time appears to be linear with an r value of 0.918 (p = 0.0278).

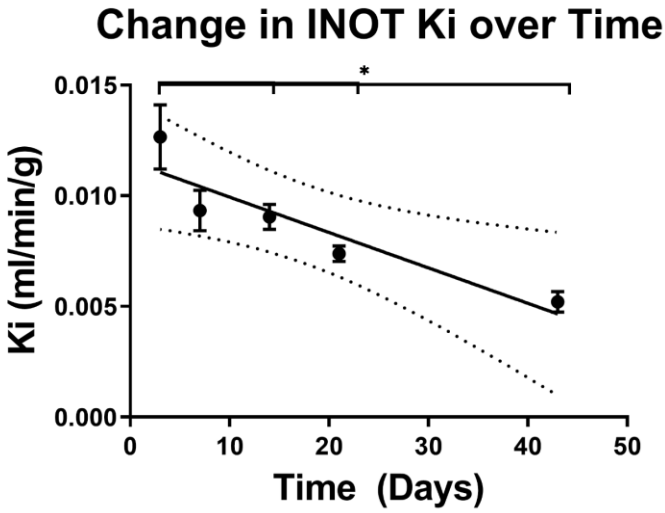

Figure 3-11: Ki in INOT post-MI.

INOT Ki decreases linearly (dashed lines indicate confidence interval) over time, returning to pre-infarct values (0.00514+/- 0.00045) at day 43. Ki in the INOT is significantly different from day 3 at day 14 (p=0.0143), day 21 (p=0.0031) and day 42 (p=0.0003).

The distribution volume in the INOT, calculated with the Patlak model, also undergoes significant changes post-MI, where days 7 ($p = 0.0199$), 14 ($p = 0.0015$), 21 ($p = 0.0001$) and 42 ($p < 0.0001$) are significantly higher than day 3 as shown in figure 3-12.

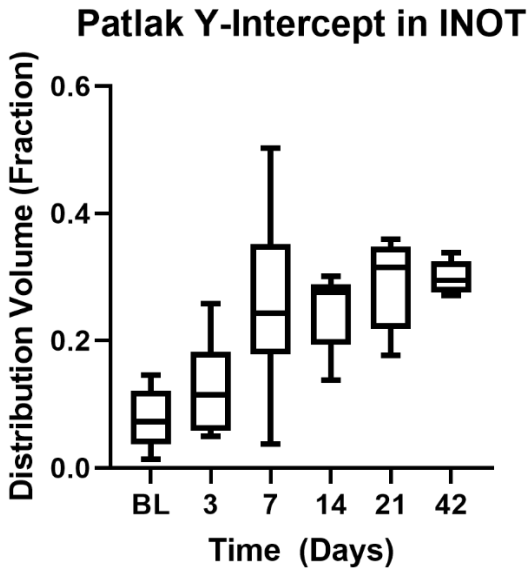

Figure 3-12: Distribution volume (y-intercept) calculated using the Patlak model in the INOT.

Days 7 (p=0.0199), 14 (p = 0.0015), 21 (p = 0.0001) and 42 (p < 0.0001) are significantly higher than baseline though a lot of variation was seen on day 7.

Glucose metabolism in the IOT is increased at days 3 (p = 0.0332) and 7 (p = 0.0042) relative to baseline. There were not enough values for subsequent days to test significance, although in the remaining animals, it does appear to stay elevated.

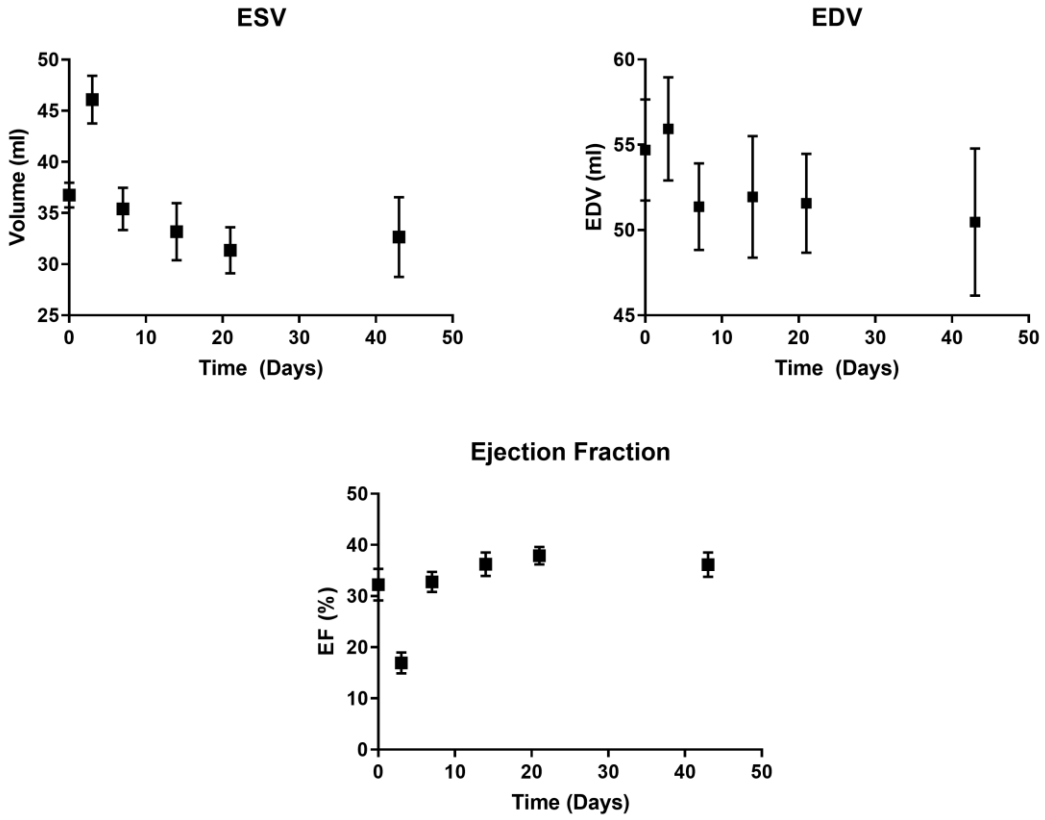

Figure 3-13: End-systolic volume, end-diastolic volume and ejection fraction over time post-MI.

As in human patients, there is an initial drop in ejection fraction (p=0.0013) which then recovers in the following week and remains near baseline. This initial decline can be explained by an increased ESV (p = 0.0127) with steady EDV.

3.3.4 Measurements of Cardiac Function

Figure 3-13 shows the ejection fraction (EF), end-diastolic volume (EDV) and end-systolic volume (ESV) for all animals. A sharp decrease in ejection fraction is visible at day 3 (p = 0.0013) before it returns to a baseline value at day 7. The end diastolic volume on the other hand does not show a difference while the ESV increases on day 3 (p = 0.0127).

3.4 Discussion

In this study, we have applied PET/MR using a combined infusion of a gadolinium-based contrast agent and FDG to assess cell-based inflammation, myocardial fibrosis, and edema, in multiple regions of potential myocardial injury following an acute myocardial infarction. Accurate assessment of these processes can be compromised by issues of reduced tracer delivery, particularly within the central core of an infarction, where microvascular obstruction can markedly reduce blood flow. A single bolus injection of either tracer may not allow adequate penetration of these tracers into these areas of markedly compromised flow.

Although our group has previously demonstrated that concurrent constant infusions of Gd-DTPA and FDG can provide valid measures of ECV and ^{18}F-FDG in normal myocardium[13], this is the first time this injection strategy has been used to investigate RT, INOT and IOT post-MI, and sequentially over several weeks. It is evident from figure 3-6a) that identical ECV values in RT can be measured after 20 to 30 minutes after the onset of a constant infusion until 30 minutes after terminating the constant infusion implying that the GBCA must be being cleared similarly from the RT and blood.

The ECV in the INOT reached equilibrium between 50 and 60 minutes of onset for days 7 – 40 and likely did at the 60 minute time point for day 3 (see figure 3-7), demonstrating that even with reduced blood flow in the INOT tissue, a 60-minute wash in was sufficient to obtain accurate values of ECV. However, the 60 min constant infusion in the IOT appears to not have reached equilibrium within the tissue and hence it is unlikely that the estimate of ECV is accurate. The data presented in figure 3-5 and figure 3-7 at 7, 14 and 21 days suggests that ECV of IOT may actually be similar to that of INOT at the end of the 60 min infusion. However, in the early days following infarction, at day 3, the IOT measured ECV was comparable to RT and much lower than the measured value in INOT. Nevertheless, compared to a bolus injection, significant penetration does occur with the 60 min constant infusion[11,16,25].

Unlike RT, measurements of ECV during washout in the INOT and IOT should not be used as they were significantly elevated at all washout time points as shown in figure 3-7,

3-8 and 3-9. This is presumably because the blood flow is lower in the IOT and INOT and thus dramatically reduces Gd-DTPA clearance in the myocardium compared to blood, meaning that measured ECV appears artificially elevated[26]. This is the opposite to the beginning of the scan, where the ECV is underestimated as the tracer entering the INOT lags behind Gd-DTPA concentrations in the blood. Note that these observations regarding achieving equilibrium in RT, INOT and IOT for GD-DTPA imply that FDG, which was concurrently injected with Gd-DTPA, would behave similarly.

We found a significant increase in ECV in the RT at days 14 and 21 post-MI, but not at days 3 and 7. Increases in ECV in RT may reflect more generalized but less intense tissue edema and/or an early fibrotic response, not just limited to the area of acute ischemic injury, a pattern that has been shown in rats[8,28]. Cleutjens *et al.* have shown increased collagen protein deposition in rats in both infarcted and non-infarcted areas through upregulation of type 1 and type 3 collagen mRNA transcription[8]. This could potentially lead to the ECV increases that we observed post-MI[8,28]. At day 40, there was a p value of 0.06 for ECV in remote myocardium. A larger sample size could potentially have shown elevated ECV, 40 days post-MI. ECV calculation provides important, non-invasive insight into the pathophysiological mechanisms of cardiac remodeling post-MI and may serve as an important source of diagnostic, therapeutic and prognostic decision making[10,29–31]. Specifically, the change in ECV in remote non-infarcted tissue provides strong evidence that there is a pathological process evolving in the early weeks post-infarct[8,28,32]. Future work is needed, such as validating this through measuring amount of fibrosis in histological tissue samples taken from RT and comparing it to tissue from sham treated animals.

Figure 3-13 shows that the functional assessments have a similar timeline for evolution of heart function as human patients post-MI with reduced ejection fraction[27]. There is a sharp decrease in ejection fraction at day 3 and recovery over the subsequent time points.

The decrease in the INOT volume using the 3D T1 weighted images (Figure 3-5) has underscored a long-standing debate. This decrease likely does not represent a degree of

tissue repair but rather reflects permanently damaged myocardial tissue, in essence, shriveling over the days and weeks post infarct. Note this data was taken while the blood and tissue concentrations were kept constant in the RT and to a large extent in the INOT tissue due to the constant infusion.

The FDG results that we observed were not as consistent as the ECV results. This is partially attributable to the lower spatial resolution of cardiac -FDG PET in comparison to GBCA MRI, leading to potential partial volume issues in the discrimination of IOT from INOT. However, there should be a minimal partial volume effect from the left ventricular blood pool when assessing RT as myocardial edges were not included. As shown in 3-9 there is a trend of an increase in Ki from baseline at days 3, 7, 14, and 21 though no significant changes were observed day3: p=0.38; day 7 p = 0.32; day 14: p = 0.11; day 21: p = 0.19; day 43: p = 0.63. These values are also similar to what was found by Herrero et al in normal canine myocardium during suppression[33]. Figure 3-6b) shows increases in ECV at days 7, 14 and potentially 43 days. Although not large effects, this suggests that increases in ECV (potentially edema and fibrosis) is accompanied by cell based inflammation in RT. Note how both results (Figures 3-6b and 3-10) suggest that by 43 days both are proportionately reduced. If fibrosis had developed it would seem unlikely that it would have resolved, suggesting that perhaps edema associated with the ^{18}F-FDG detected inflammation may have started to resolve.

Glucose metabolism in INOT decreased with time as shown in figure 3-10, with Ki highest at 3 days (0.0125 ml/min/g) decreasing to approximately normal tissue values by day 43. In contrast, the Patlak analysis for INOT (see figure 3-8) showed a significant increase in the extravascular exchangeable volume. This decrease in glucose metabolism in the INOT suggests that the number of metabolically active macrophages is decreasing or are being converted into M2-like macrophages, which take up less FDG than M1-like macrophages[26]. It appears that the INOT experiences the highest level of inflammation within the first week following which it declines and returns to baseline by day 43. The IOT glucose metabolism was also significantly increased for the first week but could not be evaluated as a separate region distinct from the surrounding INOT after that due to the decreasing number of animals with an IOT at the later time points as there is apparent

recovery from the initial microvascular injury. This strengthens the notion that anti-inflammatory treatment would be most effective within the first two weeks, but it also shows that the IOT may be an important factor influencing the perseverance of inflammation, especially since glucose metabolism in that region is probably underestimated. As we have shown here, even after the 60 min constant infusion, Gd-DTPA concentration was still increasing. This would suggest a corresponding increase in FDG concentrations within the IOT and that the methodology used in the experiments reported here underestimated the true glucose metabolic rate in the IOT.

Limitations of this study include the small number of animals, but even more so, the small number of animals with an IOT that was sustained through the period of observation, although this pattern of resolution of the regions of microvascular obstruction is by itself noteworthy. Another limitation is that not all animals could be imaged at every timepoint. While most animals had an IOT at day 3 and day 7, they disappeared at day 14, for all but two animals. More animals would also let us study the RT in more detail, since there is an increase in ECV on days 14 and 21 which may correspond to an inflammatory response. We have also found that ECV may be affected by myocardial glucose uptake suppression, i.e. is larger by 13% in healthy myocardium[13]. Since all of these animals were suppressed equally, the trends found should not be affected, but actual ECV values may be slightly lower.

3.5 Conclusion

Here we have shown rigorous longitudinal measurements of inflammation and ECV, measured during a combined infusion of FDG and GBCA. ECV in remote myocardium at 14- and 21- days post-MI was significantly greater than at baseline. The change in ECV in remote non-infarcted tissue provides strong evidence that there is a pathological process evolving in the early weeks post-infarct. As the concentration of FDG in the IOT continues to rise by the end of the constant infusion, it stands to reason that a bolus injection of FDG would underestimate the glucose metabolism in the IOT.

3.6 References

1. Braunwald E. Research advances in heart failure: A compendium. *Circ Res* 2013;113:633-645. doi:10.1161/CIRCRESAHA.113.302254

2. Eitel I, Kubusch K, Strohm O, Desch S, Mikami Y, De Waha S, et al. Prognostic value and determinants of a hypointense infarct core in T2-weighted cardiac magnetic resonance in acute reperfused ST-elevation- myocardial infarction. *Circ Cardiovasc Imaging* 2011;4:354-362. doi:10.1161/CIRCIMAGING.110.960500

3. Pfeffer MA, Braunwald E. Ventricular remodeling after myocardial infarction: Experimental observations and clinical implications. *Circulation* 1990;81:116-172. doi:10.1161/01.CIR.81.4.1161

4. Ganame J, Messalli G, Dymarkowski S, Rademakers FE, Desmet W, Van De Werf F, et al. Impact of myocardial haemorrhage on left ventricular function and remodelling in patients with reperfused acute myocardial infarction. *Eur Heart J* 2009;30:1440-1449. doi:10.1093/eurheartj/ehp093

5. Kim RJ, Wu E, Rafael A, Chen EL, Parker MA, Simonetti O, et al. The use of contrast-enhanced magnetic resonance imaging to identify reversible myocardial dysfunction. *N Engl J Med* 2000. doi:10.1056/NEJM200011163432003

6. Biesbroek PS, Amier RP, Teunissen PFA, Hofman MBM, Robbers LFHJ, van de Ven PM, et al. Changes in remote myocardial tissue after acute myocardial infarction and its relation to cardiac remodeling: A CMR T1 mapping study. *PLoS One* 2017. doi:10.1371/journal.pone.0180115

7. Lurz JA, Luecke C, Lang D, Besler C, Rommel KP, Klingel K, et al. CMR–Derived Extracellular Volume Fraction as a Marker for Myocardial Fibrosis: The Importance of Coexisting Myocardial Inflammation. *JACC Cardiovasc Imaging* 2018. doi:10.1016/j.jcmg.2017.01.025

8. Cleutjens JPM, Verluyten MJA, Smits JFM, Daemen MJAP. Collagen remodeling after myocardial infarction in the rat heart. *Am J Pathol* 1995.

9. Radenkovic D, Weingärtner S, Ricketts L, Moon JC, Captur G. T1 mapping in cardiac MRI. *Heart Fail Rev* 2017. doi:10.1007/s10741-017-9627-2

10. Thornhill RE, Prato FS, Wisenberg G, Moran GR, Sykes J. Determining the extent to which delayed-enhancement images reflect the partition-coefficient of Gd-DTPA in canine studies of reperfused and unreperfused myocardial infarction. *Magn Reson Med* 2004. doi:10.1002/mrm.20236

11. Salerno M, Janardhanan R, Jiji RS, Brooks J, Adenaw N, Mehta B, et al. Comparison of methods for determining the partition coefficient of gadolinium in the myocardium using T1 mapping. *J Magn Reson Imaging* 2013. doi:10.1002/jmri.23875

12. Diesbourg LD, Prato FS, Wisenberg G, Drost DJ, Marshall TP, Carroll SE, et al. Quantification of myocardial blood flow and extracellular volumes using a bolus injection of Gd-DTPA: Kinetic modeling in canine ischemic disease. *Magn Reson Med* 1992;23:239-253. doi:10.1002/mrm.1910230205

13. Smailovic H, Wilk B, Wisenberg G, Sykes J, Butler J, Hicks JW, et al. Simultaneous measurements of myocardial glucose metabolism and extracellular volumes with hybrid PET/MRI using concurrent injections of Gd-DTPA and [18F]FDG. *Submitt to J Nucl Cardiol* 2020.

14. Larson SR, Pieper JA, Hulten EA, Ficaro EP, Corbett JR, Murthy VL, et al. Characterization of a highly effective preparation for suppression of myocardial glucose utilization. *J Nucl Cardiol* 2019. doi:10.1007/s12350-019-01786-w

15. Merten CL, Knitelius HO, Assheuer J, Bergmann-Kurz B, Hedde JP, Bewermeyer H. MRI of acute cerebral infarcts: Increased contrast enhancement with continuous infusion of gadolinium. *Neuroradiology* 1999. doi:10.1007/s002340050740

16. Prato FS, Butler J, Sykes J, Keenliside L, Blackwood KJ, Thompson RT, et al. Can the Inflammatory Response Be Evaluated Using 18F-FDG Within Zones of Microvascular Obstruction After Myocardial Infarction? *J Nucl Med* 2015;56:299-

304. doi:10.2967/jnumed.114.147835

17. Lau JMC, Laforest R, Sotoudeh H, Nie X, Sharma S, McConathy J, et al. Evaluation of attenuation correction in cardiac PET using PET/MR. *J Nucl Cardiol* 2017;24:839-846. doi:10.1007/s12350-015-0197-1

18. Patlak CS, Blasberg RG, Fenstermacher JD. Graphical evaluation of blood-to-brain transfer constants from multiple-time uptake data. *J Cereb Blood Flow Metab* 1983;3:1-7. doi:10.1038/jcbfm.1985.87

19. Lawrence J, Chang YMR, Szladovits B, Davison LJ, Garden OA. Breed-specific hematological phenotypes in the dog: A natural resource for the genetic dissection of hematological parameters in a mammalian species. *PLoS One* 2013. doi:10.1371/journal.pone.0081288

20. Higgins PJ, Garlick RL, Bunn HF. Glycosylated hemoglobin in human and animal red cells. Role of glucose permeability. *Diabetes* 1982. doi:10.2337/diab.31.9.743

21. Lortie M, Beanlands RSB, Yoshinaga K, Klein R, DaSilva JN, DeKemp RA. Quantification of myocardial blood flow with 82Rb dynamic PET imaging. *Eur J Nucl Med Mol Imaging* 2007;34:1765-1774. doi:10.1007/s00259-007-0478-2

22. Anazodo U, Kewin M, Finger E, Thiessen J, Hadway J, Butler J, et al. Preliminary evaluation of MRI-derived input function for quantitative measurement of glucose metabolism in an integrated PET-MRI. *EJNMMI Phys* 2015;2:1-2. doi:10.1186/2197-7364-2-s1-a80

23. White SK, Sado DM, Fontana M, Banypersad SM, Maestrini V, Flett AS, et al. T1 Mapping for Myocardial Extracellular Volume Measurement by CMR. *JACC Cardiovasc Imaging* 2013. doi:10.1016/j.jcmg.2013.01.011

24. Fedorov A, Beichel R, Kalpathy-Cramer J, Finet J, Fillion-Robin JC, Pujol S, et al. 3D Slicer as an image computing platform for the Quantitative Imaging Network. *Magn Reson Imaging* 2012. doi:10.1016/j.mri.2012.05.001

25. Bekkers SCAM, Yazdani SK, Virmani R, Waltenberger J. Microvascular Obstruction. Underlying Pathophysiology and Clinical Diagnosis. *J Am Coll Cardiol* 2010. doi:10.1016/j.jacc.2009.12.037

26. Borchert T, Beitar L, Langer LBN, Polyak A, Wester H-J, Ross TL, et al. Dissecting the target leukocyte subpopulations of clinically relevant inflammation radiopharmaceuticals. *J Nucl Cardiol* 2019.

27. Chew DS, Heikki H, Schmidt G, Kavanagh KM, Dommasch M, Bloch Thomsen PE, et al. Change in Left Ventricular Ejection Fraction Following First Myocardial Infarction and Outcome. *JACC Clin Electrophysiol* 2018. doi:10.1016/j.jacep.2017.12.015

28. Sun Y, Cleutjens JPM, Diaz-Arias AA, Weber KT. Cardiac angiotensin converting enzyme and myocardial fibrosis in the rat. *Cardiovasc Res* 1994. doi:10.1093/cvr/28.9.1423

29. Kidambi A, Motwani M, Uddin A, Ripley DP, McDiarmid AK, Swoboda PP, et al. Myocardial Extracellular Volume Estimation by CMR Predicts Functional Recovery Following Acute MI. *JACC Cardiovasc Imaging* 2017. doi:10.1016/j.jcmg.2016.06.015

30. Thornhill RE, Prato FS, Wisenberg G, White JA, Nowell J, Sauer A. Feasibility of the single-bolus strategy for measuring the partition coefficient of Gd-DTPA in patients with myocardial infarction: Independence of image delay time and maturity of scar. *Magn Reson Med* 2006. doi:10.1002/mrm.20830

31. Haaf P, Garg P, Messroghli DR, Broadbent DA, Greenwood JP, Plein S. Cardiac T1 Mapping and Extracellular Volume (ECV) in clinical practice: A comprehensive review. *J Cardiovasc Magn Reson* 2016. doi:10.1186/s12968-016-0308-4

32. Hinderer S, Schenke-Layland K. Cardiac fibrosis – A short review of causes and therapeutic strategies. *Adv Drug Deliv Rev* 2019. doi:10.1016/j.addr.2019.05.011

33. Herrero P. Quantification of myocardial glucose utilization by PET and 1-carbon-11-glucose. *J Nucl Cardiol* 2002;9:5-14. doi:10.1067/mnc.2001.120635

Chapter 4

4 Myocardial glucose suppression interferes with the detection of inflammatory cells with FDG-PET in a canine model of myocardial infarction

4.1 Introduction

Following a myocardial infarction (MI), heart failure may develop due to a number of factors such as extent of initial myocardial injury, but is also influenced to a major extent by dysregulation of inflammation in response to the original insult[1]. MRI measurements have shown promise in detecting characteristics associated with an increased risk of heart failure, including infarct size[2,3], presence of hemorrhage and presence and size of microvascular injury/obstruction[4,5], hereafter referred to as Infarcted Obstructed Tissue (IOT). Extracellular volume (ECV) measurements, generally associated with tissue injury and/or edema, in particular, provides a sensitive measurement of myocardial fibrosis[6]. To acquire ECV measurements with MRI, T1 maps pre- and post-contrast are required[7,8]. Our group has previously shown how a constant infusion of a gadolinium-based contrast agent (GBCA) can be used to measure ECV post-MI using a 60 min constant infusion[9,10].

FDG-PET imaging allows assessment of cell-mediated inflammation but may not be able to distinguish between uptake of the tracer by pro-inflammatory (neutrophils and M1 macrophages) vs. anti-inflammatory (M2 macrophages) cells. Further, post-MI, to make FDG-PET specific for inflammation, uptake of FDG by non-infarcted myocardium has to be suppressed as completely as possible so that the residual uptake of glucose is specific and limited to that by the resident and invading inflammatory cells. In humans, sequestration of the FDG tracer by myocardium can be achieved with fasting and the injection of heparin[11], which enhances free fatty acid utilization and decreases glucose uptake by myocardium. In the canine model, myocyte glucose uptake suppression can be achieved through a combination of fasting, the injection of heparin and a lipid infusion at the time of FDG administration. However, it is not known if these suppressive techniques

may also affect the degree of uptake (i.e. the metabolic activity) by the inflammatory cells (macrophages). Here, we have investigated this question in the canine model of MI.

Another issue to be considered that may affect the accurate determination of the degree of inflammation within the infarct core is the potential partial volume effect of IOT on the Infarcted Non-Obstructed Tissue (INOT). Due to the very compromised blood flow, PET tracers injected as a bolus do not penetrate the IOT. As the size of the IOT is often too small to be resolved from the INOT with PET, the presence of IOT may cause INOT FDG uptake to appear artificially lower.

Here we report on our investigation of these potential limitations. We have evaluated the use of a prolonged 150 min constant infusion of FDG and Gd-DTPA instead of a bolus injection. This prolonged constant infusion allows the investigation of the effect of suppression on uptake of FDG by inflammatory cells through the tracking of the metabolic activity before, during and after the use of myocardial suppression techniques. Further, this will also provide some insight into the pattern and degree of inflammatory activity within the central IOT.

4.2 Materials and Methods:

4.2.1 Animal Preparation

The care and treatment of the animals was in accordance with the University of Western Ontario Council on Animal Care (Animal Use Subcommittee) guidelines. The adult, female, bred-for-research hounds weighed 18-23 kg. Anesthesia for all procedures was induced using propofol and maintained with 1.5% - 2% isoflurane (Forane, Baxter). In experiment one, six animals were studied at baseline (BL) twice, to determine the effect on glucose uptake in normal myocardium of heparin alone (BL1) and of heparin combined with lipid infusion (BL2). Combined with fasting, preliminary data indicates that the combination of heparin and lipid is the most effective approach to suppression in canines[12]. In experiment two, five of the animals from experiment one and two additional animals, which did not undergo the procedures in experiment one, underwent a procedure to induce a myocardial infarction. The left anterior descending coronary artery

was permanently ligated during left thoracotomy. Five days after the surgery, the seven animals were imaged. As only one imaging procedure was possible at five days, the effect of suppression of glucose metabolism in the remote tissue and in the infarcted tissue was investigated using both a heparin injection and the lipid infusion. Heparin was administered as an intravenous bolus of 2000 units and a 20% lipid infusion (Intralipid; Baxter Healthcare Corporation) was given intravenously over a 50 minute period at a rate of 0.25 ml/min/kg. Since all canines were of a similar weight (20-23kg) the same dose of heparin was used. Before each scan, the blood glucose level was measured with a glucometer. After the post-MI imaging at 5 days, animals were given 20mL propofol and then euthanized with an injection of KCl (30mL administered intravenously).

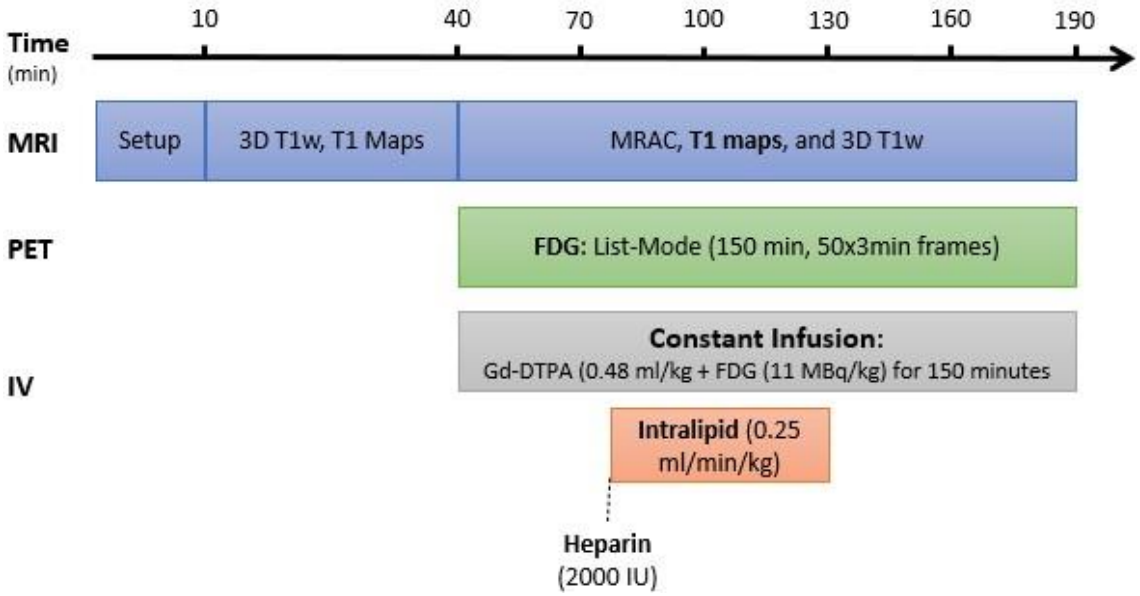

Figure 4-1: 150-minute constant infusion protocol.

Cine images, 3D T1 weighted images and T1 maps were acquired pre-contrast. PET list-mode acquisition was started simultaneously with the constant infusion of Gd-DTPA and FDG. Heparin injection and lipid infusion were done 40 minutes into the constant infusion.

4.2.2 Injection Protocol

In previous work, we have established that a simultaneous constant infusion of both Gd-DTPA and ^{18}FDG is an effective approach to measure the extracellular volume (ECV) by MRI and the glucose metabolism (MRGlu) by PET[9]. Unlike the typical approach using a bolus injection, a prolonged constant infusion can be easily modelled to monitor the effects on ECV and MRGlu of different interventions such as glucose suppression. In this study, a 150 min constant infusion was implemented. Note that as the animals required fasting to allow anesthesia, there is already a level of glucose suppression that varies between animals. In the first baseline scan (BL1), a bolus of heparin was administered 40 minutes after the start of constant infusion while in BL2 and post-MI, in addition to the heparin injection, a constant infusion of intralipid was begun and continued for 50 minutes. In all cases, the ECV and MRGlu were determined for three time intervals during the constant infusion: from 10 to 40 min, 60 to 90 min and from 120 to 150 min. These three time intervals have been hereafter identified as “before”, “during” and “after” glucose suppression. During the entire 150 min constant infusion, Gd-DTPA was administered intravenously at 4 μmol/min/kg and FDG at 0.17 MBq/min/kg.

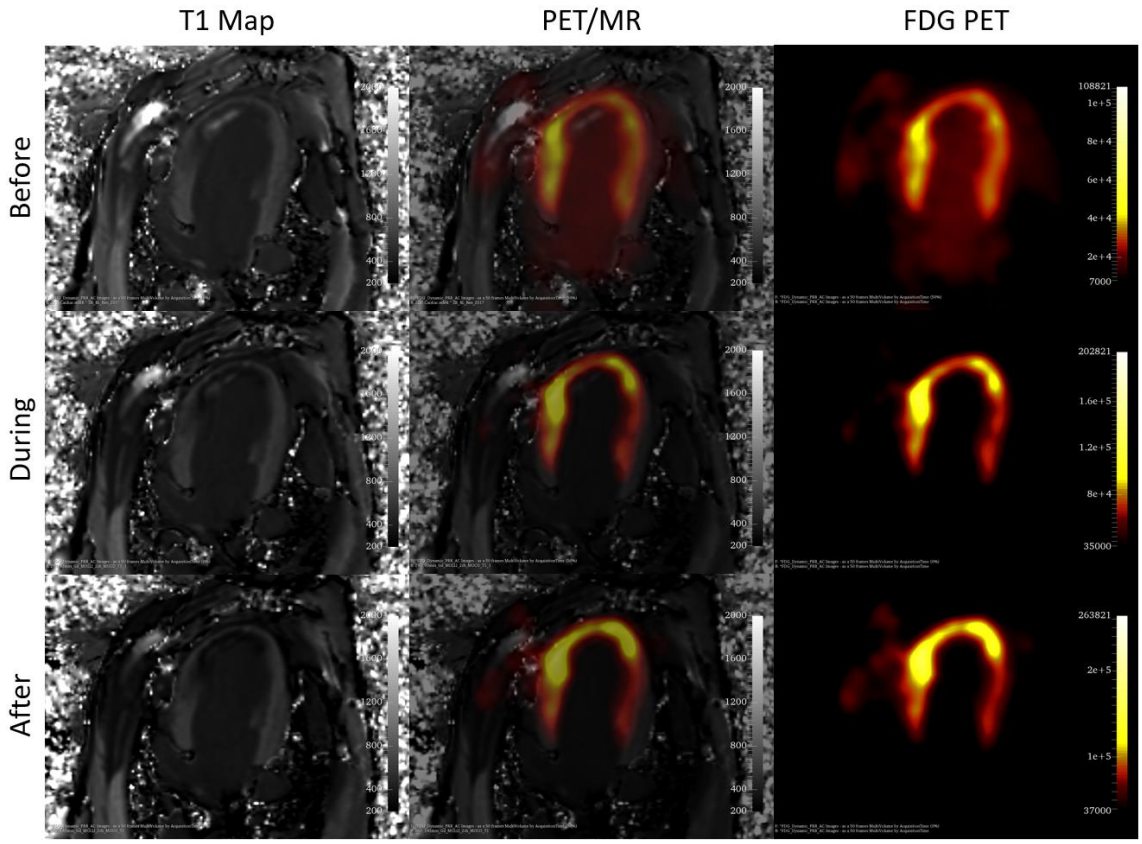

Figure 4-2: FDG uptake and T1 maps 5 days post-MI pre- and post-suppression.

Images were taken at 40 minutes (before suppression), 90 minutes (during suppression) and at 150 minutes (after suppression).

4.2.3 PET/MRI Protocol

All scans were done on a 3T PET/MRI (Siemens Biograph mMR). The animals were placed in the right lateral recumbent position and 3 electrodes were positioned on the chest to obtain an ECG reading. The protocol is shown in figure 4-1 with the 150 min constant infusion started at 40 min after the start of the imaging to allow for set-up and baseline MRI acquisitions needed for the ECV calculation.

Cardiac T1 maps (4-chamber view of the heart) were acquired with a modified Look-Locker inversion recovery (MOLLI) sequence[13] (ECG-gated, 35° flip angle, 256 x 218 matrix size, 300 mm x 255.5 mm field-of-view, 6 mm slice thickness, 400ms repetition

time, 1.12ms echo time) during breath hold at pre-contrast and then every 10 min after the concurrent infusions. PET data was acquired in list-mode throughout the 150 min constant infusion and subsequently reconstructed in 3-minute frames using a 3D Ordered Subset Expectation Maximization (OSEM) reconstruction (3 iterations, 21 subsets, 172 x 172 x 127 matrix size, zoom of 2 and 4 mm Gaussian filter). Attenuation correction was achieved using a two-point Dixon MRI sequence and segmented into water, fat, lung and air with constant attenuation coefficients for each tissue. The PET voxel size was (2.09 x 2.09 x 2.03) mm^3.

4.2.4 Image Analysis

Figure 4-2 shows a typical hybrid PET/MRI image set acquired at 60 and 150 min into the 150 min constant infusion. Note that, due to the intrinsic hardware registration of the PET and MRI subsystems, regions of infarct identified on an MRI image are automatically registered to the PET images. However, as PET images are not corrected for respiratory motion whereas MRI images are the registration is compromised. Image analysis was performed using 3D Slicer (Open Source, BSD License) and MATLAB (Mathworks, R2019a). As shown in figure 4-3, manually drawn regions of interest (ROIs) in the 4-chamber view were used to identify the healthy myocardium and the left ventricular blood pool for the baseline experiments. Post-MI, three regions were identified and manually outlined by an experienced observer: remote tissue (RT), infarcted non-obstructed tissue (INOT) and infarcted obstructed tissue (IOT). Once the ROIs were defined, they were used as a template and copied to the rest of the images in the series. Manual adjustment of some images in the series was applied to offset changes in heart position. Edges were also avoided when drawing ROIs to minimize partial volume averaging from voxels at the myocardial-blood pool border. Dynamic T1 values (pre- and post- Gd-DTPA administration) and FDG activity concentration were measured in each ROI.

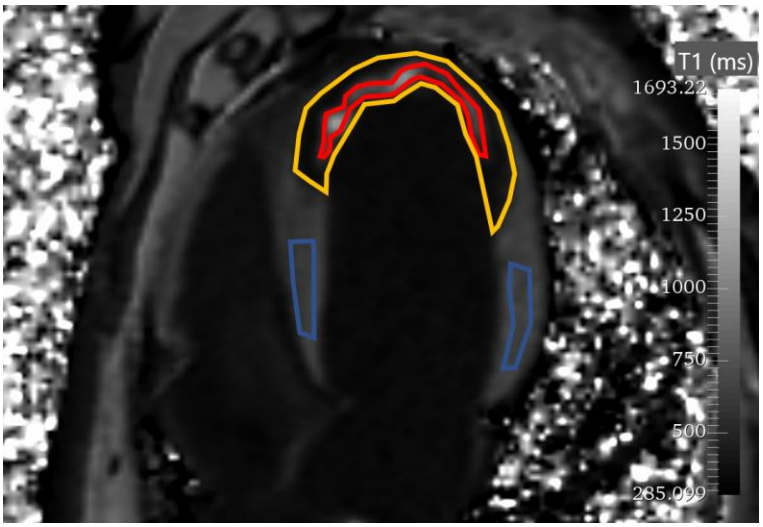

Figure 4-3: Regions of interest at 5 days post-MI used for the 150-minute constant infusion protocol.

Regions of interest as defined on a T1 map 60 minutes after the start of the infusion. Red represents the IOT, yellow the INOT and blue the RT.

4.2.5 Volumes of IOT and INOT

Volumes were manually drawn on 3D T1 weighted images by an experienced observer at 30 and 150 minutes into the constant infusion.

4.2.6 Extracellular Volume Determination

ECV was calculated as discussed in 2.2.3.

4.2.7 Glucose Metabolism

K_i was extracted for all ROIs in all studies as discussed in 2.2.4 and the metabolic rate of glucose (MRGlu) was calculated by multiplying K_i by the blood glucose level, taken before the study.

4.2.8 Histology

After the experiment 2 imaging session, the hearts from 5 of the subjects were extracted and imaged with PET/MRI. Three regions were visually identified on the left ventricle: the centre of infarct, edge of infarct and remote tissue. Samples were fixed, frozen and embedded in optimal cutting temperature compound (OCT), and subsequently sectioned at 5-6 μm thickness, as previously described[19,20]. Immunohistochemistry using primary and fluorophore-conjugated secondary antibodies was conducted as previously described[19,20]. In brief, tissue sections were incubated with blocking buffer in 10% serum for 30 minutes at room temperature followed by incubation with primary polyclonal or monoclonal antibodies for 1h at room temperature in a humidified chamber. These antibodies were used to identify macrophages (CD68 (ab955) 1:200 dilution) and glucose transporter 1 (Glut1 (orb157188) 1:1000 dilution). Samples were rinsed twice in phosphate buffered solution (PBS) and incubated for 2h at room temperature with secondary antibodies (Donkey anti rabbit 488 (A21206) 1:1000 dilution; Donkey anti-mouse 594 (A21203) 1:1000 dilution). Sections were washed twice with PBS, incubated 8 min with DAPI nuclear stain (1:1000), and mounted with ProLong Diamond antifade (Life Technologies) to prevent the tissues from photobleaching.

High resolution images were captured with a Nikon A1R Confocal Microscope at 60x magnification using an oil immersion lens. Five random fields of view were acquired for each of 4 tissue sections per sample with the exposure time, gain and look up tables set the same for all tissue sections. Therefore, each sample (reported as data points in all graphs) reflects an average of 4 technical replicates.

Images of CD68 and GLUT1 were analyzed with FIJI 1.49v, a distribution of ImageJ software (National Institutes of Health, Bethesda). Punctate staining patterns were quantified using the RenyiEntropy algorithm, an entropy-based approach that distinguishes the positive punctate signals within the cells from the background. The integrated density represents the mean intensity of the positive signal above a certain threshold in scaled units divided by the area in pixels. The integrated density threshold was set such that the entropies of distributions above and below the set threshold are

maximized. Therefore, this algorithm only captured the high intensity punctate staining patterns and did not calculate any background staining of these images.

4.2.9 Statistical Analysis

Statistical analysis was performed using GraphPad Prism (GraphPad Software, La Jolla, CA). All data is presented as mean ± standard error of the mean (SEM). Paired two-tailed t-tests were performed to compare values before, during and after suppression. A p-value of <0.05 was considered to be statistically significant. Bonferroni's method was done to correct for multiple comparisons when comparing multiple treatment's means.

4.3 Results

4.3.1 Effect of Suppression on metabolic rate of glucose consumption

As shown in figure 4-2, glucose suppression using heparin and an infusion of intralipid has the desired effect of suppressing remote myocardial tissue and thereby highlighting the inflammatory activity within the infarcted zone. As heparin was injected at 40 minutes and the lipid infusion was started at the same time, suppression was seen on the FDG time-activity graphs at 60 minutes. At 150 minutes, there is a higher concentration of FDG in the infarcted zone compared to the 60 minute time point. This is also highlighted by the graph in figure 4-4, showing the FDG uptake quantitatively over time in one animal.

When we analyse the metabolic rate of glucose in all tissues using Patlak graphical analysis, a significant difference is seen from before glucose suppression to during, with a reduction in the metabolic rate, and after, as shown in figure 4-5. Using both heparin injection and lipid infusion (BL2), a significant difference is seen in healthy tissue from before to during and after suppression. However, using heparin only (BL1) this effect is not as large, with significance only reached between before and during but not before and after suppression. This may mean that heparin alone is not as effective in suppressing

glucose metabolism as the combination of heparin and lipid infusion. Post-MI, MRGlu in both INOT and RT are significantly reduced as shown in figure 4-5. Before suppression there is no significant difference in MRGlu between INOT and RT but during and after suppression, MRGlu is significantly higher in the INOT.

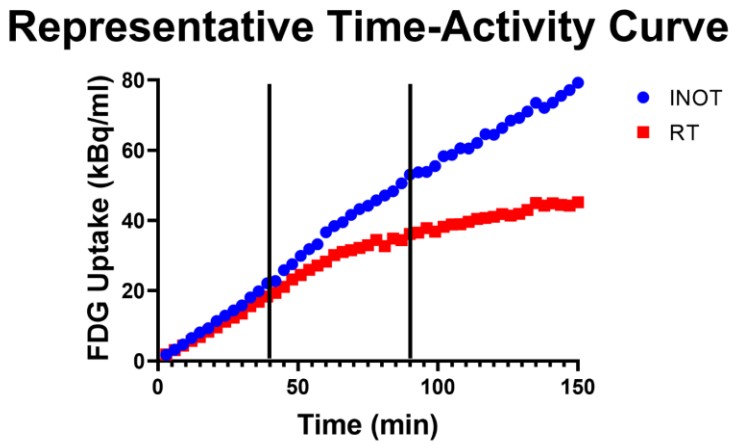

Figure 4-4: FDG activity concentration over the course of a 150-minute constant infusion in one representative animal.

During the first 60 minutes, INOT and remote tissue rise at almost the same rate but when suppression takes effect, the slope of the remote tissue is strongly reduced while in INOT it is only reduced slightly. Vertical bars show the time during which lipid infusion is applied.

4.3.2 Effect of suppression on extracellular volume

As shown in figure 4-6 with either heparin alone (BL1) or heparin with lipid infusion (BL2), there is no significant difference in ECV measurements in healthy tissue between before, during and after, highlighting that neither heparin nor intralipid infusion affect ECV measurements. Post-MI, there is also no significant effect of suppression in the RT and INOT on ECV.

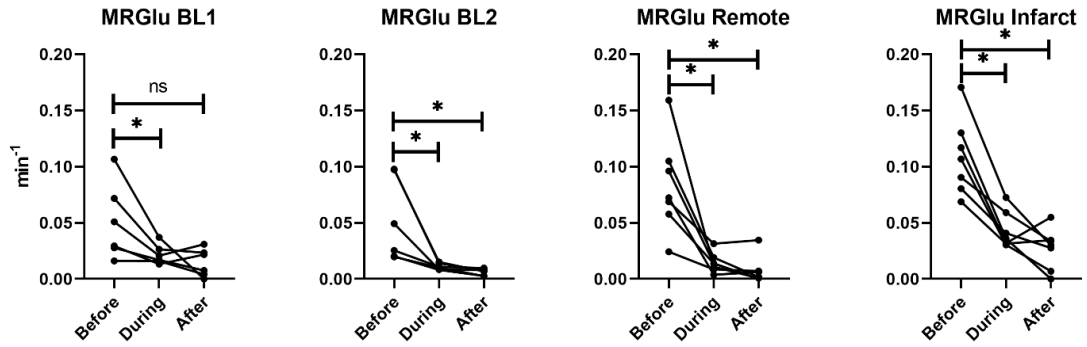

Figure 4-5: Metabolic rate of glucose consumption at baseline and 5 days post-MI.

Metabolic rate of glucose consumption decreases in all cases when suppression is applied. However, when using heparin only (BL1), there is no significant difference from before suppression to after. It should also be noted that post-MI, MRGlu does not decrease as much as in the remote tissue even though their starting points are similar. No significant differences were found between during suppression and after suppression.

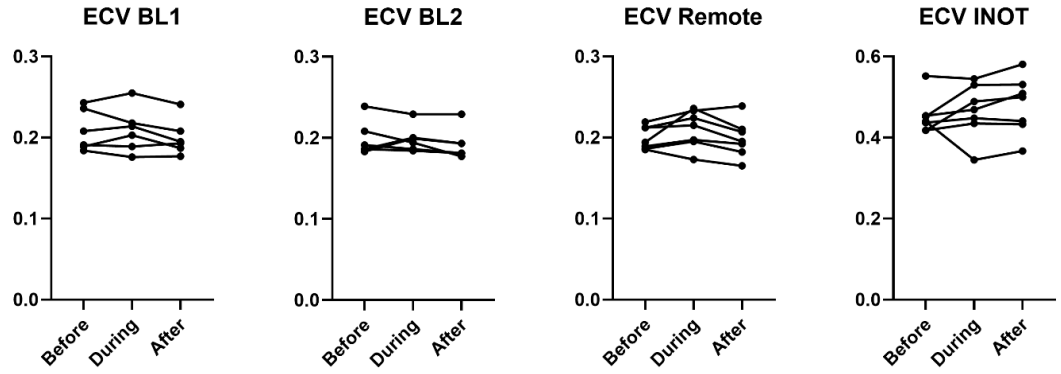

Figure 4-6: Suppression of myocardial glucose uptake does not affect ECV at 5 days.

There is no significant difference between suppression by heparin only and heparin and lipid infusion. Suppression of myocardial glucose uptake did not significantly affect ECV. It should be noted that the ECV in the INOT was approximately twice as large as in remote tissue.

4.3.3 Penetration of infarcted obstructed tissue

As shown in figures 4-2 and 4-7, there is a degree of penetration of Gd-DTPA, and therefore likely FDG, into the IOT. It appears that the FDG activity in the IOT is rising linearly over the course of the infusion. The apparent size of the IOT is also greatly reduced in the three animals with an IOT (69%, 93% and 93% reduction in IOT volume from 30-150 min) when the measurement after 30 min of CI is compared to the end of the constant infusion i.e. at 150 min due to progressive penetration of the tracer into the areas of most compromised flow during the course of the infusion.

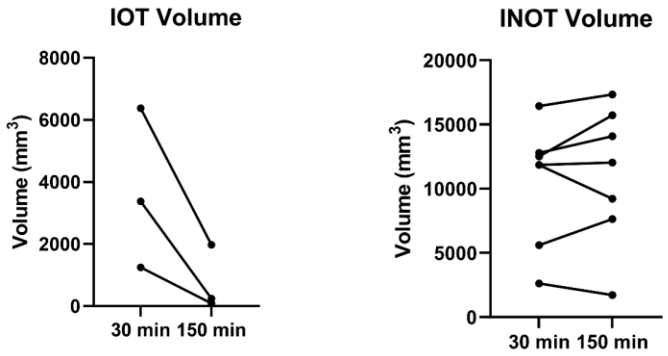

Figure 4-7: IOT and INOT volume 5 days post-MI.

While only three animals had an IOT, in these animals, the IOT volume decreased by 69%, 93% and 93%, showing some penetration over time of the IOT. INOT volume on the other hand remained the same.

4.3.4 Histology

As shown in figure 4-8, there was a significant increase in CD68 expression in the centre of the infarct compared to the edge of the infarct and in the remote tissue which were not significantly different. There was no difference seen in GLUT1 expression for all regions.

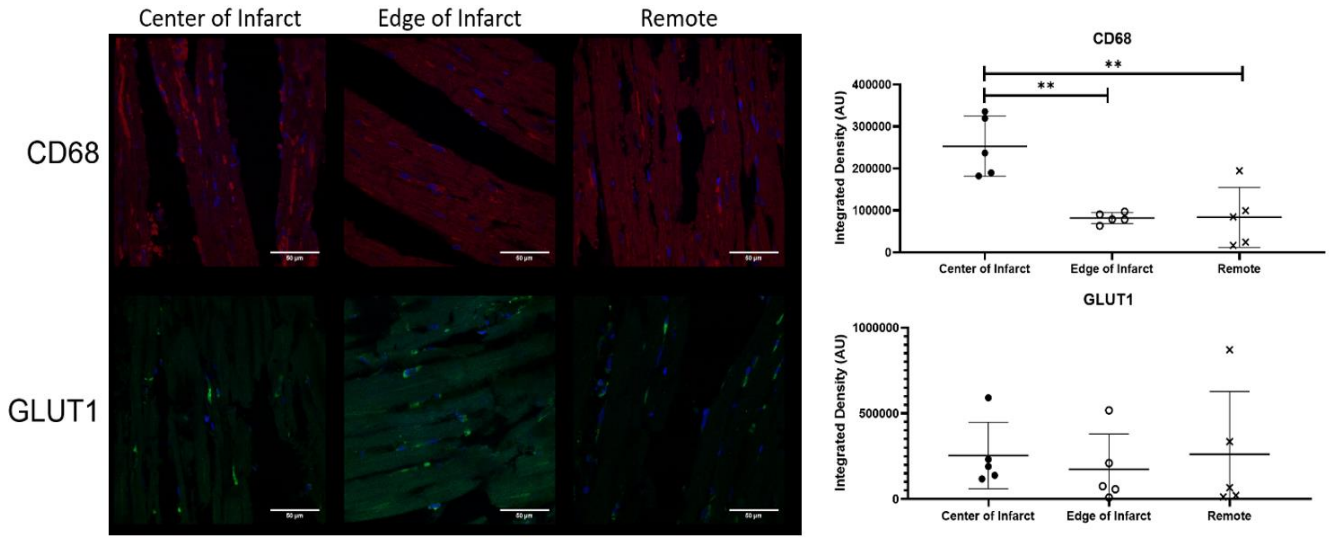

Figure 4-8: GLUT1 and CD68 expression 5 days post-MI.

No significant differences were seen in the GLUT1 expression in the center of infarct, edge of infarct and remote tissue. However, CD68 expression was higher in the center of infarct than at the edge of infarct and in the remote tissue. Representative histological images of each are shown on the left.

4.4 Discussion

Myocardial glucose suppression has previously been assumed to only affect cardiomyocytes but not inflammatory cells such as macrophages[21]. This has been largely an unquestioned assumption in publications dealing with protocols associated with the needed suppression of FDG uptake in normal myocytes in order to visualize inflammation in diseases like cardiac sarcoidosis. Here we show that there is a significant effect of suppression "within" infarcted tissue (figure 4-5), suggesting either an effect of suppression on macrophages or alternatively, the presence of a significant volume of viable myocytes in the infarcted region, that are subject to the same metabolic effects of suppression on the cardiomyocytes within the non-infarcted regions. Considering the large increase in extracellular volume (approximately double) within the infarcted region, it is unlikely that there is a large presence of viable myocytes. This potential effect of

suppression on inflammatory cells may make FDG-based PET imaging less sensitive to inflammatory activity, highlighting the need for tracers that are not only specific for the presence of inflammation but whose uptake is not confounded by the metabolic state present at the time of injection and during the period of imaging.

The difference in MRGlu results at baseline supports our previous work[9] showing that, in the canine model, to achieve adequate suppression of myocardial glucose uptake, combining a heparin injection with lipid infusion performs better than a heparin injection alone. However, the variability of FDG uptake in normal myocardium due to fasting alone, prior to anaesthesia, makes it difficult to compare values before glucose uptake suppression to after suppression.

ECV measurements, on the other hand, do not appear to be affected by heparin or lipid infusion with no significant difference seen within each baseline scan but also not between BL1 and BL2. In a previous study, we found a trend towards higher ECV with the use of heparin and lipid infusion when compared to fasting alone when the ECV was measured at 14 and 21 days post MI [9]. This implies that this increase seen was not related to an artifact associated with changes in haematocrit due to the constant infusion protocol.

While only three animals had a visible IOT, in these animals the apparent IOT volume decreased by 69%, 93% and 93% after a 150 minute constant infusion of Gd-DTPA. Not only does this show that Gd-DTPA is slowly penetrating into the IOT (the concentration will slowly continue to increase until the extravascular volume is “filled”) but it also suggests that measurement of inflammation in this region using PET imaging is possible if corrections are developed for the impact of this slow delivery of FDG. Due to the resolution of PET, the IOT also presents a major partial volume problem for the INOT and penetrating it with the tracer would make quantification of inflammation within the INOT less affected by partial volume artefacts and therefore more accurate.

Histology shows that GLUT1 expression is the same in infarcted tissue as in remote tissue; this similarity lines up well with the MRGlu before suppression in RT and INOT which is also not significantly different. While histology shows GLUT1 expression to be

the same in the infarct as in the remote tissue, the CD68 expression is more than twice as high in the infarct as in the remote tissue. Since ECV has gone up, there must be more GLUT1 receptors expressed per cell in macrophages at 5 days post MI. Previously, GLUT1 has been shown to be overexpressed in macrophages but this has not been compared to myocytes[22]. Alternatively, fasting may have reduced expression in the myocytes. It would be interesting to compare the numbers of Glut1 receptors at later times post MI when the number of M2 macrophages are dominant over the M1's that are predominantly present at 5 days post MI. The high ECV also explains the high CD68 expression as more cellular debris would lead to more macrophages. CD68 has previously been shown to be increased in infarcted and remote tissue post-myocardial infarction[23].

Limitations of this study include that the effect of fasting may be variable as we have shown previously[9] and the small number of animals, specifically the small number of animals with an IOT. With this small number of animals with IOT, it is impossible to determine whether the volume reduction is significant. It also means that glucose metabolism in the IOT could not confidently be determined.

4.5 Conclusion

This research suggests that inflammatory cells are affected by myocardial glucose uptake suppression in a canine model of myocardial infarction. This problem may be solved by using different tracers that do not require glucose suppression.

4.6 References

1. Frangogiannis NG. The inflammatory response in myocardial injury, repair, and remodelling. *Nat Rev Cardiol* 2014;11:255-265. doi:10.1038/nrcardio.2014.28

2. Eitel I, Kubusch K, Strohm O, Desch S, Mikami Y, De Waha S, et al. Prognostic value and determinants of a hypointense infarct core in T2-weighted cardiac magnetic resonance in acute reperfused ST-elevation- myocardial infarction. *Circ Cardiovasc Imaging* 2011;4:354-362. doi:10.1161/CIRCIMAGING.110.960500

3. Pfeffer MA, Braunwald E. Ventricular remodeling after myocardial infarction: Experimental observations and clinical implications. *Circulation* 1990;81:116-172. doi:10.1161/01.CIR.81.4.1161

4. Ganame J, Messalli G, Dymarkowski S, Rademakers FE, Desmet W, Van De Werf F, et al. Impact of myocardial haemorrhage on left ventricular function and remodelling in patients with reperfused acute myocardial infarction. *Eur Heart J* 2009;30:1440-1449. doi:10.1093/eurheartj/ehp093

5. Kali A, Cokic I, Tang R, Dohnalkova A, Kovarik L, Yang HJ, et al. Persistent Microvascular Obstruction after Myocardial Infarction Culminates in the Confluence of Ferric Iron Oxide Crystals, Proinflammatory Burden, and Adverse Remodeling. *Circ Cardiovasc Imaging* 2016;9:e004996. doi:10.1161/CIRCIMAGING.115.004996

6. Schelbert EB, Testa SM, Meier CG, Ceyrolles WJ, Levenson JE, Blair AJ, et al. Myocardial extravascular extracellular volume fraction measurement by gadolinium cardiovascular magnetic resonance in humans: Slow infusion versus bolus. *J Cardiovasc Magn Reson* 2011. doi:10.1186/1532-429X-13-16

7. Radenkovic D, Weingärtner S, Ricketts L, Moon JC, Captur G. T1 mapping in cardiac MRI. *Heart Fail Rev* 2017. doi:10.1007/s10741-017-9627-2

8. Thornhill RE, Prato FS, Wisenberg G, Moran GR, Sykes J. Determining the extent to which delayed-enhancement images reflect the partition-coefficient of Gd-

DTPA in canine studies of reperfused and unreperfused myocardial infarction. *Magn Reson Med* 2004;52:1069-1079. doi:10.1002/mrm.20236

9. Smailovic H, Wilk B, Wisenberg G, Sykes J, Butler J, Hicks JW, et al. Simultaneous measurements of myocardial glucose metabolism and extracellular volumes with hybrid PET/MRI using concurrent injections of Gd-DTPA and [18F]FDG. *Submitt to J Nucl Cardiol* 2020.

10. Wilk B, Smailovic H, Wisenberg G, Sykes J, Butler J, Kovacs M, et al. Tracking the progress of inflammation with PET/MRI in a canine model of myocardial infarction. *J Nucl Cardiol* 2021. doi:10.1007/s12350-020-02487-5

11. Masuda A, Naya M, Manabe O, Magota K, Yoshinaga K, Tsutsui H, et al. Administration of unfractionated heparin with prolonged fasting could reduce physiological 18F-fluorodeoxyglucose uptake in the heart. *Acta radiol* 2016. doi:10.1177/0284185115600916

12. Larson SR, Pieper JA, Hulten EA, Ficaro EP, Corbett JR, Murthy VL, et al. Characterization of a highly effective preparation for suppression of myocardial glucose utilization. *J Nucl Cardiol* 2019. doi:10.1007/s12350-019-01786-w

13. Messroghli DR, Radjenovic A, Kozerke S, Higgins DM, Sivananthan MU, Ridgway JP. Modified look-locker inversion recovery (MOLLI) for high-resolution T 1 mapping of the heart. *Magn Reson Med* 2004. doi:10.1002/mrm.20110

14. Lawrence J, Chang YMR, Szladovits B, Davison LJ, Garden OA. Breed-specific hematological phenotypes in the dog: A natural resource for the genetic dissection of hematological parameters in a mammalian species. *PLoS One* 2013. doi:10.1371/journal.pone.0081288

15. Patlak CS, Blasberg RG, Fenstermacher JD. Graphical evaluation of blood-to-brain transfer constants from multiple-time uptake data. *J Cereb Blood Flow Metab* 1983;3:1-7. doi:10.1038/jcbfm.1985.87

16. Higgins PJ, Garlick RL, Bunn HF. Glycosylated hemoglobin in human and animal red cells. Role of glucose permeability. *Diabetes* 1982. doi:10.2337/diab.31.9.743

17. Anazodo U, Kewin M, Finger E, Thiessen J, Hadway J, Butler J, et al. Preliminary evaluation of MRI-derived input function for quantitative measurement of glucose metabolism in an integrated PET-MRI. *EJNMMI Phys* 2015;2:1-2. doi:10.1186/2197-7364-2-s1-a80

18. Lortie M, Beanlands RSB, Yoshinaga K, Klein R, DaSilva JN, DeKemp RA. Quantification of myocardial blood flow with 82Rb dynamic PET imaging. *Eur J Nucl Med Mol Imaging* 2007;34:1765-1774. doi:10.1007/s00259-007-0478-2

19. McGirr R, McFarland MS, McTavish J, Luyt LG, Dhanvantari S. Design and characterization of a fluorescent ghrelin analog for imaging the growth hormone secretagogue receptor 1a. *Regul Pept* 2011. doi:10.1016/j.regpep.2011.08.011

20. Douglas GAF, McGirr R, Charlton CL, Kagan DB, Hoffman LM, Luyt LG, et al. Characterization of a far-red analog of ghrelin for imaging GHS-R in P19-derived cardiomyocytes. *Peptides* 2014. doi:10.1016/j.peptides.2014.01.011

21. Engel H, Steinert H, Buck A, Berthold T, Huch Böni RA, Von Schulthess GK. Whole-body PET: Physiological and artifactual fluorodeoxyglucose accumulations. *J Nucl Med* 1996.

22. Freemerman AJ, Johnson AR, Sacks GN, Milner JJ, Kirk EL, Troester MA, et al. Metabolic reprogramming of macrophages: Glucose transporter 1 (GLUT1)-mediated glucose metabolism drives a proinflammatory phenotype. *J Biol Chem* 2014;289:7884-7896. doi:10.1074/jbc.M113.522037

23. Lee WW, Marinelli B, van der Laan AM, Sena BF, Gorbatov R, Leuschner F, et al. PET/MRI of Inflammation in Myocardial Infarction. *J Am Coll Cardiol* 2012;59:153-163. doi:10.1016/j.jacc.2011.08.066

Chapter 5

5 Conclusions, Limitations and Future Directions

5.1 Conclusions and Future Direction

In this final chapter, the main objectives of this thesis will be discussed and summarised. Additional limitations will be outlined and future directions will be discussed. The overall impact of this research on the field of PET/MRI in myocardial infarction imaging will also be considered.

5.2 Research Objectives

Post-myocardial infarction, patients are at risk of adverse remodeling leading to heart failure, in part due to an ongoing, dysregulated pro-inflammatory response. An imaging method is needed to determine whether patients are at risk of or currently undergoing a dysregulated pro-inflammatory response in remote, peri-infarct and infarcted tissue. The objectives of this research were to a) determine that it is safe to combine gadolinium-based contrast agents and FDG, b) evaluate whether a constant infusion could be used to achieve the same glucose metabolism results at baseline as a bolus injection, c) longitudinally examine the use of a constant infusion post-MI and d) determine the effects of myocardial glucose suppression on extracellular volume and glucose metabolism in infarcted and remote tissue.

5.3 Summary of Individual Chapters

5.3.1 Chapter 1: Hybrid PET/MR imaging in myocardial inflammation post-myocardial infarction

Chapter 1 describes the background for the following chapters. It highlights hybrid PET/MR imaging as an emerging imaging modality which is more than just a sum of its components, PET and MRI. PET and MRI can separately image many aspects of inflammation such as glucose metabolism (PET) and perfusion (MRI). However, hybrid PET/MRI may be able to further this goal through innovative combinations of these

modalities. One such example is using a dual constant infusion of the gadolinium-based MR contrast agent and the PET tracer, allowing for easier kinetic modeling and simultaneous measurements of glucose metabolism and extracellular volume. Combined reconstruction may also allow for enhanced motion correction of PET imaging, lowering the partial volume problems associated with it[1].

5.3.2 Chapter 2: Simultaneous measurements of myocardial glucose metabolism and extracellular volumes with hybrid PET/MRI using concurrent injections of Gd-DTPA and [18F]FDG

Chapter 2 sets the groundwork for chapters 3 and 4 as well as future work. First of all, it had to be ensured that it is safe to combine Gd-DTPA and FDG or gadopentetic acid and FDG in one syringe. Both gadolinium-based contrast agents were tested to have an example of a linear and a cyclic chelator. There was no difference in pH, appearance or chromatography results between the original sample and the working sample, showing that there is no chemical change in the mixture and it is therefore safe to use. Once that was determined, the next step was to compare glucose metabolism and extracellular volume at baseline with different injection and suppression strategies. The different injection types were constant infusion only, bolus injection only and bolus injection followed by constant infusion. These were done once with suppression by heparin injection and lipid infusion and once with only fasting for glucose suppression. In all cases, the same amount of Gd-DTPA and FDG were administered. No significant differences were seen between the different injection methods, though ECV was significantly higher (13%) in the suppressed group than in the unsuppressed group. Overall, these similarities show that both bolus injection followed by a constant infusion and constant infusion only are good alternatives to the clinically used standard of care bolus injection[2].

5.3.3 Chapter 3: Tracking the progress of inflammation with PET/MRI in a canine model of myocardial infarction

In chapter 3, a potential application of the constant infusion is examined. The IOT has been historically difficult to examine due to the extremely low blood flow. The 60 min

constant infusion protocol was applied here in order to evaluate if it would be superior in penetrating this region. Remote tissue has also been chronically understudied and was therefore examined as well. Eight animals were scanned before induction of a myocardial infarction and then again at days 3, 7, 14, 21 and 42 after the surgery with the goal of measuring the glucose metabolism and extracellular volumes in INOT, IOT and RT. IOT and INOT volume as well as cardiac function were also measured. While penetration into the IOT is shown, only 3 animals presented with an IOT region which limited the ability to assess a 60 min constant infusion. ECV was significantly elevated in the RT on days 14 and 21, showing that there may be inflammation mediated extracellular edema/fibrosis within that tissue. This research also provided the first in-depth look at inflammation using PET/MRI over the first 6 weeks post-MI and provided some evidence of shrinkage of the apparent IOT volume over the course of a 60 minute constant infusion of contrast agent[3].

5.3.4 Chapter 4: Myocardial glucose suppression interferes with the detection of inflammatory cells with FDG-PET in a canine model of myocardial infarction

While a 60 minute constant infusion reduced the apparent volume of IOT (maximum of 50% reduction) seen on MRI, the effect was not large enough to eliminate partial volume effects on PET. In order to further reduce apparent IOT volume, a 150 minute constant infusion was used to penetrate the IOT. To test the effects of suppression of myocardial glucose uptake, 40 minutes into the constant infusion of Gd-DTPA and FDG, heparin was injected and a lipid infusion was started. ECV was unaffected by glucose suppression in RT and INOT at 5 days post-MI, which was consistent with the findings shown in chapter 3 at 7 days post-MI. Metabolic rate of glucose, on the other hand, was decreased in RT and INOT. The high ECV in the INOT (twice the volume fraction of remote tissue) suggests that the tissue is severely and irreversibly injured, with few or no viable myocytes. As such, the decrease in MRGlu in the INOT (figure 4-5) is likely an effect of glucose suppression primarily on macrophages. This finding highlights the need for tracers which do not rely on glucose suppression to image inflammation, e.g. PET tracers that target TSPO overexpressed in activated macrophages such as ^{18}F-FEPPA. The

efficacy of ^{18}F-FEPPA to image inflammation will have to be shown in a canine and human study, both of which are in progress.

5.4 Limitations

The major limitation of this work is the small number of animals, particularly the number of animals with microvascular obstruction. One of the goals of this research was to investigate the inflammatory response in the regions with microvascular obstruction but the small number of animals made this impractical. Using an animal model with larger infarcts and/or reperfusion injury, such as a 3-hour occlusion followed by reperfusion, may be more likely to cause the animal to have regions of microvascular obstruction[4].

In these studies, a linear gadolinium chelate, Gd-DTPA, was used. While these linear chelates have been largely discontinued due to the potential for gadolinium toxicity, their use should not affect results. There has been no evidence in literature that results obtained with linear chelates are inconsistent with cyclic chelates[5].

Histology was only conducted for one of the studies (Chapter 4) on day 5 post-MI. Histology at every timepoint would be ideal since it could be used to confirm the number of macrophages in all tissues to compare to ECV and glucose metabolism results in chapters 2 and 3. More histological data would also allow for additional information such as apoptosis to be obtained. In addition to histology, blood sampling to look for heart failure markers such as TNF-α or BNP would be a great addition to these studies since it would allow for further determination about whether the animals were moving into heart failure rather than only looking at the MRI results for cardiac function.

FDG data was only analysed in two dimensions, to align with the T1 maps. However, 3D data is available due to the nature of PET. Analysing this data in 3D would be a better way to analyse this data, simply because there would be more data. It would not however, line up with the T1 maps and would lead to further difficulties regarding region of interest selection as that is best done on the T1 maps. The constant T1 values during a constant infusion, as shown in chapter 2, could resolve this problem since 3D T1 maps could be acquired during the equilibrium time of gadolinium concentration.

ECV was calculated with the assumed haematocrit of 0.45. It would be ideal to collect blood at every point at which ECV is calculated, i.e. every 10 minutes, or at least before the scan, during the scan but before the lipid infusion, during the lipid infusion, after the lipid infusion and at the end of the scan (in terms of the 150 minutes infusion).

5.5 Future Work

5.5.1 The role of the remote tissue

Chapter 3 shows a significant difference in ECV in the remote tissue at days 14 and 21. While this likely shows damage due to inflammation, the FDG results were inconclusive. A further study with more animals and a focus on this region may be able to determine whether this is inflammation-related, especially if animals were sacrificed and tissue harvested for histology. For example, in a study with 12 animals with acute MI, 6 could be sacrificed at day 7 to obtain tissue samples from the acute inflammatory phase and the other 6 would go on to day 21 with imaging at days 3, 7, 14 and 21. Important stains would be CD68 for macrophages and neutrophils, Oil-Red O for lipid-laden macrophages (to examine fat infiltration)[6], and Haematoxylin-Eosin for apoptosis. Some research also suggests that M1 and M2 macrophages could be distinguished when staining with both CD68 and CD163 but this is still controversial[7].

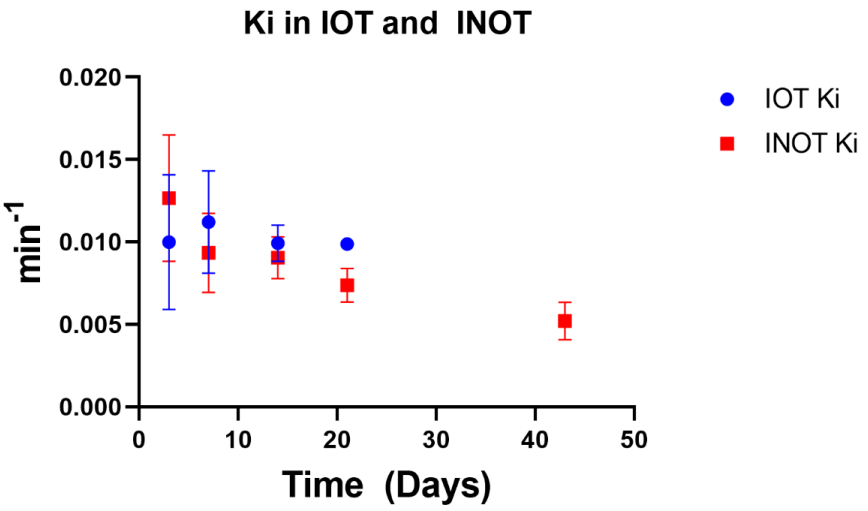

Figure 5-1: Comparison of Ki in IOT and INOT.

While the number of animals with IOT is too small to be certain, there is no significant change over time in Ki in the IOT tissue while the INOT decreases with significant differences from day 3 observed at days 14, 21 and 43.

5.5.2 The role of the microvascular obstruction in left ventricular remodelling

One of the main problems of PET/MR imaging is that it is difficult to penetrate the microvascular obstruction. Due to this, the extent of inflammation within that region is currently unknown. Chapter 3 showed the timeline of inflammation in the INOT but not the IOT. Shown in figure 5-1 are preliminary results where there is no significant change in IOT Ki over time. It would be interesting to see whether an increased number of animals with MO would show a similar trend or clarify the difference between the two curves. However, as discussed before, the number of animals with IOT is too small to be certain. Using a similar workflow to what we have used so far, but with an animal model that has a high chance of MO, perhaps reperfusion injury, would allow differences between the IOT and INOT to be brought to light. If there is indeed a difference in the timeline of inflammation in the IOT and INOT then it raises the question of whether the higher inflammation in the IOT affects inflammation in the INOT or the RT. It may be possible to focus treatment on the IOT or at least to assess the risk of heart failure in these

patients more accurately though better PET resolution, perhaps through hybrid reconstruction[8], may be necessary.

5.5.3 Interventions during a constant infusion

In chapter 4, a 150 minute constant infusion was used with suppression of myocardial glucose uptake started 40 minutes into this infusion. This had a drastic effect on myocardial glucose uptake while ECV was unaffected. This principle could be expanded to other treatments or tracers, similar to a stress/rest scan. For example, during a 10 minute constant infusion of $^{13}NH_3$, adenosine could be injected at 5 minutes and differences in the slope of tracer uptake would show which areas have a perfusion defect during rest and stress. While it would be difficult to use this approach with a short-lived tracer such as NH_3, it may be optimal for others such as ^{18}F-Flurpiridaz[9] where the long half-life prevents stress-rest scans. It could also be expanded to a fatty acid tracer such as ^{11}C-palmitate[10] where glucose or heparin could be injected partway into the scan.

5.5.4 Patient Study

In addition to the results shown in these studies, a patient study is underway. In this study, a total of 30 patients will be examined. The study consists of two imaging time-points, the first at 7-14 days following acute MI and the second at three months following MI. Before the first imaging session, patients are asked to follow a high fat diet plan and a 12-hour fast. Before imaging, a glucometer reading is taken. During the imaging session, patients receive perfusion imaging by $^{13}NH_3$ PET with cine MRI to determine cardiac function. This is followed by a 60 min break. During this break, patients receive two doses of heparin to suppress myocardial glucose uptake in conjunction with the aforementioned high fat diet and fast. Once patients are back in the PET/MRI, pre-contrast T1 and T2 maps are acquired. Then, the patients receive a combined bolus injection over 2 minutes of gadobutrol (Gadovist) and FDG followed by a 30 minute constant infusion of the same for a total dose of 0.2 mmol/kg Gadovist and 5 MBq/kg FDG. T1 maps are acquired in 2-chamber and 4-chamber views every 10 minutes for the first 40 minutes and then again between 50 and 60 minutes. PSIR images are acquired between 40 and 50 minutes. The follow up scan at 3 months post-MI is MRI only and

uses cine MRI to determine heart function and T1 maps before and after gadobutrol to determine extracellular volume.

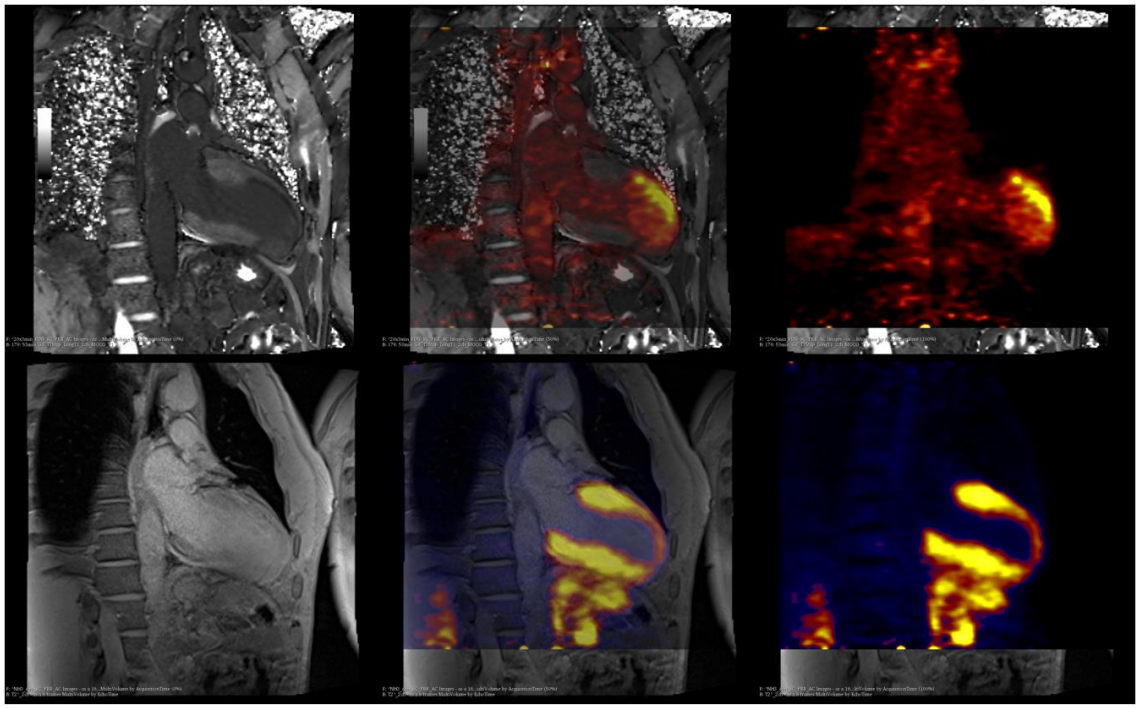

Figure 5-2: T1, T2, FDG and NH_3 images in acute MI in patients.

This figure shows, from left to right, the T1 map, T1 map with overlayed FDG and FDG alone in the top row and the T2 map, T2 overlayed with $^{13}NH_3$ and $^{13}NH_3$ alone in the bottom row. The FDG image is taken from the last time frame, 57-60 minutes. Very high FDG uptake is seen within the infarct, meaning high inflammation.

Analysis will include looking at the change in ejection fraction, end-systolic volume and end-diastolic volume from the first time point to the follow up time-point and determine if it is affected by the extent of inflammation at the acute time point. Additionally, Patlak modeling will be done to determine metabolic rate of glucose in infarcted and remote tissue and extracellular volume will also be measured in both tissues and at both time points. These values will then be compared with the change in cardiac function from the initial time-point to the follow-up. $^{13}NH_3$ imaging provides the additional benefit of perfusion imaging. As such, the size of the perfusion defect can be compared to the size

of the metabolically active region determined with FDG PET and also with the size of the infarct region as determined by T1 mapping. Initial images are shown in figure 5-2.

5.6 Conclusion

This research has advanced the field of hybrid PET/MRI imaging of inflammation post-MI in terms of imaging strategies. It is the first work to show that a constant infusion can be used to penetrate the microvascular obstruction and also the first to show detailed PET/MRI imaging over the first 6 weeks after myocardial infarction. It is also the first to show that myocardial glucose suppression with lipid infusion and heparin injection affects the metabolic rate of glucose in inflammatory cells. This highlights the need for tracers that do not depend on myocardial glucose suppression.

5.7 References

1. Wilk B, Wisenberg G, Dharmakumar R, Thiessen JD, Goldhawk DE, Prato FS. Hybrid PET/MR Imaging in Myocardial Inflammation Post-Myocardial Infarction. *J Nucl Cardiol* 2019;Epub ahead.

2. Smailovic H, Wilk B, Wisenberg G, Sykes J, Butler J, Hicks JW, et al. Simultaneous measurements of myocardial glucose metabolism and extracellular volumes with hybrid PET/MRI using concurrent injections of Gd-DTPA and [18F]FDG. *Submitt to J Nucl Cardiol* 2020.

3. Wilk B, Smailovic H, Wisenberg G, Sykes J, Butler J, Kovacs M, et al. Tracking the progress of inflammation with PET/MRI in a canine model of myocardial infarction. *J Nucl Cardiol* 2021. doi:10.1007/s12350-020-02487-5

4. Yang Y, Graham JJ, Connelly K, Foltz WD, Dick AJ, Wright GA. MRI manifestations of persistent microvascular obstruction and acute left ventricular remodeling in an experimental reperfused myocardial infarction. *Quant Imaging Med Surg* 2012. doi:10.3978/j.issn.2223-4292.2011.12.02

5. Hashemi H. Comparison of Gadovist and Magnevist in brain Magnetic resonance imaging of multiple sclerosis patients with an acute attack. *Iran Red Crescent Med J* 2021;23. doi:10.32592/ircmj.2021.23.2.192

6. Cokic I, Kali A, Yang H-J, Tang R, Francis J, Dharmakumar R. Fat Infiltration Within Myocardial Infarction is Initiated by Macrophage Foam Cell Formation in the Scar Regions Containing Persistent Iron Deposits. *Circulation* 2018;134.

7. Barros MHM, Hauck F, Dreyer JH, Kempkes B, Niedobitek G. Macrophage polarisation: An immunohistochemical approach for identifying M1 and M2 macrophages. *PLoS One* 2013. doi:10.1371/journal.pone.0080908

8. Schramm G, Rigie D, Vahle T, Rezaei A, Van Laere K, Shepherd T, et al.

Approximating anatomically-guided PET reconstruction in image space using a convolutional neural network. *Neuroimage* 2021;224. doi:10.1016/j.neuroimage.2020.117399

9. Packard RRS, Huang SC, Dahlbom M, Czernin J, Maddahi J. Absolute quantitation of myocardial blood flow in human subjects with or without myocardial ischemia using dynamic flurpiridaz F 18 PET. *J Nucl Med* 2014. doi:10.2967/jnumed.114.141093

10. Christensen NL, Schacht AC, Munk OL, Alstrup AKO, Tolbod LP, Harms HJ, et al. Whole-body biodistribution, dosimetry and metabolite correction of [11C]palmitate: A PET tracer for imaging of fatty acid metabolism. *Mol Imaging* 2017.

Appendices

Appendix A: Copyright for Chapter 1: Hybrid PET/MR Imaging in Myocardial Inflammation Post-Myocardial Infarction

4. Authors' Retained Rights

Author(s) retain the following non-exclusive rights for the published version provided that, when reproducing the Article or extracts from it, the Author(s) acknowledge and reference first publication in the Journal:

a. to reuse graphic elements created by the Author(s) and contained in the Article, in presentations and other works created by them;
b. they and any academic institution where they work at the time may reproduce the Article for the purpose of course teaching (but not for inclusion in course pack material for onward sale by libraries and institutions); and
c. to reproduce, or to allow a third party Assignee to reproduce the Article in whole or in part in any printed volume (book or thesis) written by the Author(s).

Article Details

Journal title	Article title
Journal of Nuclear Cardiology	Hybrid PET/MR Imaging in Myocardial Inflammation Post-Myocardial Infarction
DOI	**Corresponding Author**
10.1007/s12350-019-01973-9	Benjamin Wilk

Appendix B: Animal Use approval for chapters 2, 3 and 4.

AUP Number: 2011-067
PI Name: Prato, Frank
AUP Title: Validating Total Myocardial Inflammation in a Canine Model of Sustained Occlusion For Cell Therapy Optimization
Official Notification of AUS Approval: A MODIFICATION to Animal Use Protocol 2011-067 has been approved.
The holder of this Animal Use Protocol is responsible to ensure that all associated safety components (biosafety, radiation safety, general laboratory safety) comply with institutional safety standards and have received all necessary approvals. Please consult directly with your institutional safety officers.
Submitted by: Kinchlea, Will D
on behalf of the Animal Use Subcommittee

Appendix C: Copyright for Chapter 2: Simultaneous measurements of myocardial glucose metabolism and extracellular volumes with hybrid PET/MRI using concurrent injections of Gd-DTPA and [18F]FDG

Journal Name:	Journal of Nuclear Cardiology	(the 'Journal')
Manuscript Number:	JNC-20-345-OA.R2	
Proposed Title of Article:	Simultaneous measurements of myocardial glucose metabolism and extracellular volumes with hybrid PET/MRI using concurrent injections of Gd-DTPA and [18F]FDG	
Author(s) [Please list all named Authors]:	Benjamin Wilk, H. Smailovic, B. Wilk, G. Wisenberg, J. Sykes, J. Butler, J. Hicks, J. D. Thiessen, F. S. Prato	(the 'Author')
Corresponding Author Name:	Benjamin Wilk	

4 Reuse Rights

Author retains the following non-exclusive rights for the published version provided that, when reproducing the Article or extracts from it, the Author acknowledges and references first publication in the Journal according to current citation standards. In any event the acknowledgement should contain as a minimum, "First published in [Journal name, volume, page number, year] by Springer Nature".

a) to reuse graphic elements created by the Author and contained in the Article, in presentations and other works created by them;

b) the Author and any academic institution where they work at the time may reproduce the Article for the purpose of course teaching (but not for inclusion in course pack material for onward sale by libraries and institutions);

c) to reuse the published version of the Article or any part in a thesis written by the same Author , and to make a copy of that thesis available in a repository of the Author(s)' awarding academic institution, or other repository required by the awarding academic institution. An acknowledgement should be included in the citation: "Reproduced with permission from Springer Nature"; and

d) to reproduce, or to allow a third party to reproduce the Article, in whole or in part, in any other type of work (other than thesis) written by the Author for distribution by a publisher after an embargo period of 12 months.

Appendix D: Copyright for Chapter 3: Tracking the progress of inflammation with PET/MRI in a canine model of myocardial infarction

Journal Name:	Journal of Nuclear Cardiology	(the 'Journal')
Manuscript Number:	JNC-20-346-OA.R2	
Proposed Title of Article:	Tracking the progress of inflammation with PET/MRI in a canine model of myocardial infarction	
Author(s) [Please list all named Authors]:	Benjamin Wilk, B. Wilk, H. Smailovic, G. Wisenberg, J. Sykes, J. Butler, M. Kovacs, J. D. Thiessen, F. S. Prato	(the 'Author')
Corresponding Author Name:	Benjamin Wilk	

4 Reuse Rights

Author retains the following non-exclusive rights for the published version provided that, when reproducing the Article or extracts from it, the Author acknowledges and references first publication in the Journal according to current citation standards. In any event the acknowledgement should contain as a minimum, "First published in [Journal name, volume, page number, year] by Springer Nature".

a) to reuse graphic elements created by the Author and contained in the Article, in presentations and other works created by them;

b) the Author and any academic institution where they work at the time may reproduce the Article for the purpose of course teaching (but not for inclusion in course pack material for onward sale by libraries and institutions);

c) to reuse the published version of the Article or any part in a thesis written by the same Author , and to make a copy of that thesis available in a repository of the Author(s)' awarding academic institution, or other repository required by the awarding academic institution. An acknowledgement should be included in the citation: "Reproduced with permission from Springer Nature"; and

d) to reproduce, or to allow a third party to reproduce the Article, in whole or in part, in any other type of work (other than thesis) written by the Author for distribution by a publisher after an embargo period of 12 months.

Appendix E: Ethics approval of cardiac patient study mentioned in Chapter 5

Principal Investigator: Dr. Gerry Wisenberg
Department & Institution: Schulich School of Medicine and Dentistry\Imaging,London Health Sciences Centre

Review Type: Full Board
HSREB File Number: 109025
Study Title: A Pilot Study of the Assessment of Early Post-Myocardial infarction Inflammation Using PET/MR

HSREB Initial Approval Date: April 03, 2017
HSREB Expiry Date: April 03, 2018

Documents Approved and/or Received for Information:

Document Name	Comments	Version Date
Letter of Information & Consent	clean LOI Main Study	2017/03/01
Western University Protocol	clean ethics protocol--Received March 5/17	
Sub-Study Letter of Information & Consent	Biomarker LOI - Clean	2017/03/30

The Western University Health Science Research Ethics Board (HSREB) has reviewed and approved the above named study, as of the HSREB Initial Approval Date noted above.

Curriculum Vitae

BENJAMIN WILK

EDUCATION

Western University
PhD in Medical Biophysics **2015-Present**
Dissertation: “Combined contrast infusion in hybrid PET/MRI to investigate the infarcted myocardium”

University of Ontario Institute of Technology
Bachelor of Education **2014-2015**
Teachables in Physics and Mathematics

University of Ontario Institute of Technology
Bachelor of Science **2010-2014**
Honours Thesis: Simulation of Graphene and Boron Nitride Heterosystems:
Structure, Electron Bands, Stability and Vibrations
Minor: Mathematics

AWARDS

Ontario Graduate Scholarship **September 2019 – August 2020**
Lawson Internal Research Fund **January 2018 – December 2018**

RELATED RESEARCH EXPERIENCE

University of Ontario Institute of Technology
Research Assistant **2014-2015**
Implementing an Object-Oriented, Modern, Optimal Control System for a Robot.

University of Ontario Institute of Technology
Undergraduate Research Assistant **2013-2014**
2D and 3D Graphene and Boron Nitride Heterosystems.

TEACHING EXPERIENCE

Western University
Biology Teaching Assistant **2019-2020**
Presented introductory materials, supervised students in a laboratory setting and graded reports.

Western University Judo Club
Assistant Instructor **2018-2020**
Taught judo techniques to beginners and advanced students. These classes are comprised of approximately 15 people and student safety is a key concern, requiring "classroom" management and attention to detail.

Western University
Mathematics Teaching Assistant **2016-2019**
Marked quizzes, tests and exams for first year calculus and linear algebra and taught tutorials to up to 200 students.

Western University
Physics Teaching Assistant **2015-2016**
Presented introductory materials and supervised up to 48 students in first year physics labs.

Dunbarton High School, Sinclair Secondary School and Gandatsetiagon Public School
Teacher Candidate **2013-2014**

Taught a variety of classes, including physics and math but also music art and language from grades 7-12 under the supervision of an associate teacher.

UOIT
Physics Teaching Assistant **2013-2014**
Marked assignments and midterms for Electricity and Magnetism I + II, Fluid Mechanics, Mathematical Physics, Mechanics II, Modern Physics, Quantum Mechanics I, Statistical Mechanics I and Thermodynamics.

UOIT
Undergraduate Teacher Candidate **2010-2014**
Observed and assisted full time teaching staff at Bolton C. Falby Public School, Pine Ridge Secondary School and the Ontario Science Centre, including the preparation of experiments.

ACADEMIC SERVICE AND VOLUNTEER EXPERIENCE

Western Aikido Club
Executive Member **2017 – 2020**
Taking on numerous roles within the executive team included creating and managing the budget, leading classes and organising social events.

St. John Ambulance
Sergeant Administration **2016 – 2018**
Provided first aid at events across Southwestern Ontario and completed administrative tasks to do with recruitment.

UOIT Bachelor of Education Student Association
Treasurer **2014 – 2015**
Create and follow a budget for the club, managing incoming funds and expenses for all club activities including events and clothing sales.

UOIT Physics Society
Founding President **2012-2014**
Organised physics colloquia with guest speakers as well as other social and academic events. Managed clothing and telescope sales to fund the society.

UOIT Concurrent Education Student Association
Executive Member **2011-2014**
Contributed to the founding and organization of the annual Concurrent Education Student Association Professional Development Conference.

UOIT Astronomy Club
Founding Executive Member **2013-2014**
Organised meetings and social events and maintained contact with the Durham Region Astronomical Association.

PUBLICATIONS

Simultaneous measurements of myocardial glucose metabolism and extracellular volumes with hybrid PET/MRI using concurrent injections of Gd-DTPA and [18F]FDG
H Smailovic, B Wilk, G Wisenberg, J Sykes, J Butler, J W Hicks, J D Thiessen, F S Prato
Journal of Nuclear Cardiology, submitted 2020

Tracking the progress of inflammation with PET/MRI in a canine model of myocardial infarction
B Wilk, H Smailovic, G Wisenberg, J Sykes, J Butler, M Kovacs, J D Thiessen, F S Prato
Journal of Nuclear Cariology, submitted 2020

Hybrid PET/MR imaging in myocardial inflammation post-myocardial infarction

B Wilk, G Wisenberg, R Dharmakumar, J D Thiessen, D E Goldhawk, F S Prato
Journal of Nuclear Cardiology 2019

Same day comparison of PET/CT and PET/MR in patients with cardiac sarcoidosis
G Wisenberg, J D Thiessen, W Pavlovsky, J Butler, B Wilk, F S Prato
Journal of Nuclear Cardiology 2019

[18F]FDG cardiac PET imaging in a canine model of radiation-induced cardiovascular disease associated with breast cancer radiotherapy
O El-Sherif, I Xhaferllari, J Sykes, J Butler, R A deKemp, J Renaud, H Yin, B Wilk, R Sullivan, J G Pickering, J Battista, G Wisenberg, F S Prato, S Gaede
American Journal of Physiology. Heart and Circulatory Physiology 2019

Graphene-Boron Nitride 2D Heterosystems Functionalized with Hydrogen: Structure, Vibrations, Optical Response, Electron Band Engineering and Bonding
A I Shkrebtii, B Wilk, R Minnings, R Zapata-Pena, S M Anderson, B S Mendoza, I M Kupchak
Advances in Science and Technology 2017

PRESENTATIONS

Myocardial glucose suppression interferes with the detection of inflammatory cells with FDG-PET in a canine model of myocardial infarction
Society of Nuclear Medicine and Molecular Imaging Conference,
Virtual Oral Presentation 2021

Quantifying Inflammation in Infarcted Myocardial Tissue with Severely Reduced Flow: A Hybrid PET/MRI Approach Using a Prolonged Constant Infusion of 18F-FDG and Gd-DTPA
Society of Nuclear Medicine and Molecular Imaging Conference,
Pennsylvania Convention Centre, Philadelphia: Poster Presentation 2018

Gadobutrol and 18F-FDG Do Not Interact When Combined in a Single Syringe for Combined Contrast PET/MRI
European Association of Nuclear Medicine and Molecular Imaging Conference,
Austria Centre, Vienna: Poster Presentation 2017

Comparing bolus injection and constant infusion of Gd-DTPA and 18F-FDG in a canine model of myocardial infarction
Society of Nuclear Medicine and Molecular Imaging Conference,
Colorado Convention Centre, Denver: Poster Presentation 2017

Comparison of constant infusion to bolus FDG delivery to evaluate inflammation of the infarcted myocardium
Ottawa Heart Conference,
Westin Ottawa, Ottawa: Oral Presentation 2017

Developing a combined contrast kinetic model in heart failure using hybrid PET/MRI
Society of Nuclear Medicine and Molecular Imaging Conference,
San Diego Conference Centre, San Diego: Oral Presentation 2016

Tracer kinetics in a canine model of cardiac infarction: Bolus injection versus constant infusion of 18F-FDG with simultaneous PET/MRI
Conference on PET/SPECT MR,
Julich Research Centre, Cologne: Oral Presentation 2016

2D Electron Band Engineering: Application of High Performance Computing to Quantum Nano-Systems
Compute Ontario Research Day,
Perimeter Institute, Waterloo: Oral and Poster Presentation 2014

2D Electron Band Engineering: Computer Simulations of Graphene and Boron Nitride Based Heterosystems
Canadian Undergraduate Physics Conference,
McMaster University, Waterloo: Oral and Poster Presentation 2013